SCUOLA DI DOTTORATO

UNIVERSITÀ DEGLI STUDI DI MILANO-BICOCCA

PhD SCHOOL in
CHEMICAL SCIENCE
Department of Materials Science

Exploration of Photocatalyzed PET-RAFT Polymerization: from Polymer Synthesis to Polymer Recycling

Valentina BELLOTTI
Matr. 806779 (XXXVI *Cycle*)

Supervisor: Prof. Roberto Simonutti
Tutor: Prof. Davide Ballabio

ACADEMIC YEAR 2022/2023

Table of Contents

Chapter 1

Scope of the Thesis: Summary article

Polymers and material science are nowadays essential for many aspects of everyday life, indeed polymeric materials cover a large portion of the actual market. Polymer science is subjected to continuous challenges and one of the main task is the development of precise and sustainable techniques for the production of advanced materials for multidisciplinary fields such as biosensors, packaging, biotechnology, medical science, microelectronics, solar cells, formulation chemistry, composite materials, and so on. For this reason, understanding the chemistry and physics of polymers is fundamental for the development of new materials or for the improvement of existing technologies.

Free radical polymerization (FRP) is the most used industrial procedure for polymer synthesis *via* a chain-growth mechanism. In fact, almost 50% of the synthetic polymers are produced using radical methods due to the easy synthetic requirement (just deoxygenation is needed), relatively low temperatures (usually lower than 100 °C) and minimal attention to presence of water or protic impurities. The polymerization can be carried out in solution, bulk, dispersion, emulsion, and so on. Finally, almost all alkene-based monomer families can be easily polymerized through radical mechanisms with high tolerance of different functionalities (hydroxy, amino, acids, etc.). Nevertheless, even if FRP can provide a wide range of polymers, it has some important restrictions, which limit the production of more complex and advanced materials. The major drawback of FRP is the quick termination of the propagating chains once the kinetic chain length is reached. This results in no control over molecular weight, dispersity, morphology or the possibility of post-polymerization modifications.

The discovery and development of Reversible-Deactivation Radical Polymerization (RDRP) has revolutionized and enlarged the scope of polymer chemistry, making possible the preparation of materials one though impossible to produce *via* radical process. RDRP methods introduced several advantages such as: precise control of the molecular weight which culminates in very narrow dispersity of the polymeric chains. Moreover, the final polymer chains are considered "living" or "controlled", meaning that the polymerization can be initiated, stopped, and restarted, and the polymer is capped with a specific functionality. The presence of a chain-end is particularly interesting for the synthesis of polymers with controlled architectures such as block copolymers, star polymers, and nanoparticles. Finally, the presence of the chain-end is also valuable for post-polymerization modification or grafting onto specific surfaces. Those characteristics all together opened the doors to new applications going from drug delivery to coatings, adhesives, nanotechnology, and the synthesis of complex materials. One of the most versatile and popular RDRP techniques for synthesizing complex polymers with tunable properties is the reversible addition-fragmentation chain transfer (RAFT) polymerization. The latter follow a degenerative chain transfer mechanism thanks to the use of thiocarbonylthio-containing molecules, also called chain transfer agents (CTAs) of RAFT agents, which ultimately terminate the polymer chain.

More recently, the merging between photochemistry and polymer science has gained great interest due to the several advantages of light as an external stimulus for initiating polymerization. In particular, in the last decade photoinduced electron/energy transfer (PET)-RAFT polymerization has been introduced to the scientific community as a valuable alternative to traditional RAFT polymerization. The use of light and photocatalyst provide various advantages in terms of oxygen tolerance, room temperature polymerization, spatiotemporal control which brings to process simplification, low cost, sustainability, resulting in new applications in lithography, 3D and 4D printing, biological conjugation and high throughput synthesis.

Last but not least, now more than ever one of the most important challenges in polymer chemistry is enhancing the sustainability of plastic materials. There are different methods to address this topic, such as the development of biorenewable or biodegradable polymers, mechanical recycling or chemical recycling. In particular, the latter is highly appealing due to the fact that not only the monomer can be retrieved but also re-used to produce completely new materials which would permit circular economy of traditional plastics. In 2020 depolymerization of polymers was included in the IUPAC top ten impact technologies in chemistry and nowadays remain one of the most investigated themes for the future.

1.1 Structure of the thesis

The primary goal of this thesis is to provide an in-depth exploration of PET-RAFT polymerization. This examination will encompass various levels, including mechanistic aspects, and applicability in polymer and material science with a particular emphasis on nanotechnology.

Furthermore, we will explore the potential for utilizing this technique in closing the loop of plastic, by chemical recycling through photo-assisted chemical processes. Hopefully, the readers will appreciate the great potential of light-induced control polymerization both in the context of material manufacturing and the sustainable recovery of chemicals, paving the way for its potential scale-up and industrial adoption. To provide a comprehensive overview, the thesis begins with a detailed introduction in **Chapter 2**, which covers the reaction mechanisms, the critical parameters for the polymerization, and the practical applications of controlled PET-RAFT polymerizations and depolymerization.

Mechanistic studies of PET-RAFT polymerization

While the mechanism of RAFT polymerization is indeed well-established, the same cannot be said for PET-RAFT. In fact, this technique introduces additional mechanistic complexities due to the interactions between the photocatalyst in the excited state with the CTA, the effect of light intensity and wavelength, and the charge stabilization effect of the solvents. Furthermore, the use of heterogeneous catalysts instead of the more common homogeneous reaction mixtures introduces further questions regarding the significance of available surface area and the interactions occurring on the surface with the involved chemical species. Understanding these interactions in heterogeneous media is of extreme importance because heterogeneous catalysis plays a pivotal role in the industrialization of chemical processes. This complexity highlights the need for a deeper investigation into the mechanistic aspects of PET-RAFT polymerization.

In this context, this thesis commences with **Chapter 3,** where titanium dioxide (TiO_2)-based nanoparticles were explored for the first time to enable visible-light-regulated PET-RAFT polymerization. In this chapter we combined experimental investigations and Density Functional Theory (DFT) calculations with a twofold aim: firstly, to understand the mechanism of photopolymerization and the critical interactions involved, and secondly, to shift the PC absorption region towards visible light for visible-light polymerization.

The computational calculations have been performed by Chiara Daldossi, PhD student from the Qnano group of Professor Cristiana Di Valentin, University of Milano-Bicocca.

One-pot production of nanomaterials via PET-RAFT, going from nanoparticles to nanocomposites

In the field of PET-RAFT applicability in material science our primary focus has been directed towards the development of simple and efficient methods for producing advanced materials, and in particular nanomaterials.

In **Chapter 4** we introduce a novel and versatile synthetic approach for polymerizing amphiphilic hard-shell soft-core nanoparticles *via* PET-RAFT polymerization in dispersion conditions. Soft-core nanoparticles find applications in various fields, particularly where the molecular mobility of the cargo should be preserved, such as for photon upconversion (UC), molecular rotors, or as nano-reactor for organic reactions. In this regard, poly(dimethyl acrylamide)-b-poly(butyl acrylate) amphiphilic copolymer (PDMA-b-PBA) has been selected as a promising candidate. High importance was given to the photocatalyst selection. Specifically, we selected organic naturally-derived catalysts such as metal-based porphyrin because of their applicability in various fields, (*i.e.* organic synthesis, photodynamic therapy, and sensitizers for up-conversion processes). Additionally, the low solubility in polar solvents can bring spontaneous migration into the solvophobic core during the polymerization process, resulting in their encapsulation. In so doing, the porphyrin acts both as the catalyst for the polymerization and the cargo for the desired application.

In a similar vein, one-pot production of nanocomposites has been investigated in **Chapter 5**. Within this context, we present an efficient method for generating a $CsPbBr_3$-PMMA nanocomposite through a single-step procedure *via* PET-RAFT polymerization. This approach eliminates the generation of toxic waste containing heavy metal ions and operates under mild conditions, such as room temperature and in the presence of oxygen. As in the previous case, the $CsPbBr_3$ nanocrystals fulfill a dual role. Initially, they serve as photocatalysts, facilitating the controlled polymerization of methyl methacrylate. Subsequently, they function as inorganic fillers within the nanocomposite, directly encapsulated within the newly formed polymeric matrix. The selection of RDRP technique for the production of $CsPbBr_3$-PMMA nanocomposite provided for significant advantages (due to the presence of the CTA and a constant radical concentration) allowing for high perovskite loading.

The optical measurements for Chapter 4 have been performed in collaboration with the group of Professor Angelo Monguzzi. The perovskite nanocrystals in Chapter 5 have been provided by Dr. Sara Mecca from the group of Professor Luca Beverina and the optical measurement performed in collaboration with Andrea Erroi, Dr. Francesco Carulli and Dr. Matteo Zaffalon from the group Professor Sergio Brovelli, University of Milano-Bicocca.

Light-mediated Chemical Depolymerization of RAFT polymers

Despite the numerous advantages of the PET-RAFT process over conventional RAFT, in terms of expanding the applicability, mild reaction conditions, easy equipment and process, and so on, achieving a transition from academic research to industrial implementation remains a formidable challenge. The ability to reverse the process and retrieve both the RAFT agent and the monomer is pivotal for RDRP-polymers to become industrially relevant in terms of costs. Chemical recycling aspect represents the final stage in closing the loop of plastic usage, and our focus has been to establish a method for achieving it through photo-assisted technology. Retrieving the starting monomers from polymers synthesized by reversible deactivation radical polymerization has recently emerged as an efficient way to increase the recyclability of such materials. To date, most methods have primarily focused on utilizing high temperatures to trigger an efficient depolymerization reaction. Anyway, photo-catalysis is a powerful tool, which can in principle improve thermal-driven depolymerization procedures. In **Chapter 6** we aimed to leverage the same advantages that PET-RAFT offers in polymer depolymerization to enable efficient and sustainable polymer recycling. In fact, in this chapter we present a comprehensive investigation of the photocatalyzed and temporally regulated depolymerization of RAFT-made polymethacrylates by reversing the PET-RAFT protocol.

This project has been carried out during 6 months as a visiting student at the ETH university in Zurich under the supervision of professor Athina Anastasaki.

Chapter 2

2 Literature Review

The aim of this chapter is to provide a wide overview on control polymerization techniques. In particular, the attention will be focused on Reversible Addition-Fragmentation chain-Transfer (RAFT) polymerization and Photoinduced Electron/Energy transfer (PET)-RAFT polymerization. Finally, the possibility of reverse RAFT-based polymerization by recovering the monomer will be discussed.

2.1 Reversible-Deactivation Radical Polymerization

Free radical polymerization has been extensively used in the past, both in academia and industry, for the fast production of a wide variety of polymers. Nevertheless, this method is limited for more specific applications, which require the capability to achieve target molecular weight, low dispersity of the chains, or possibility of post-polymerization modification. The discovery of reversible-deactivation radical polymerization (RDRP) allow to expand the scope of polymer science to a variety of new applications, once thought impossible through free radical mechanism.[1] RDRP techniques shear high control and "living character" of the polymerization meaning that the molecular weight and dispersity of the polymeric chains can be easily tune by adjusting the synthetic parameters and the final polymer can be reactivated in order to obtain complex architectures (*i.e.*, blocks, stars, branched or hyper-branched networks, nanoparticles, surface-grafting, and so on).[2] RDRP is a collective terms that embraces subclasses of control polymerization techniques such as nitroxide-mediated polymerization (NMP),[3] atom transfer radical polymerization (ATRP),[4] and reversible addition-fragmentation radical polymerization (RAFT).[5,6] In all the RDRP methodologies the control over the polymerization is achieved by the formation of a dormant species (polymer capped by a small molecule, depending on the RDRP class), which is in equilibrium with the (macro)-propagating radical.[7,8] Thanks to this activation/deactivation equilibrium the chains spend most of their polymerization time in the dormant state allowing slow and control addition of the monomer units. A very general mechanism is shown in **Figure 2.1.** A further classification of these techniques can be done: (i) NMP and ATRP follow a reversible deactivation mechanism which relies on the persistent radical effect. NMP exploits alkoxyamine species that cleaves at elevated temperature to release the radical and a nitroxide, similarly ATRP relies on activation of halide species by a transition metal complex. (ii) RAFT has a degenerative transfer mechanism in which there is no change in the overall number of radicals during the polymerization and so an external source of radicals is required, typically a radical initiator.

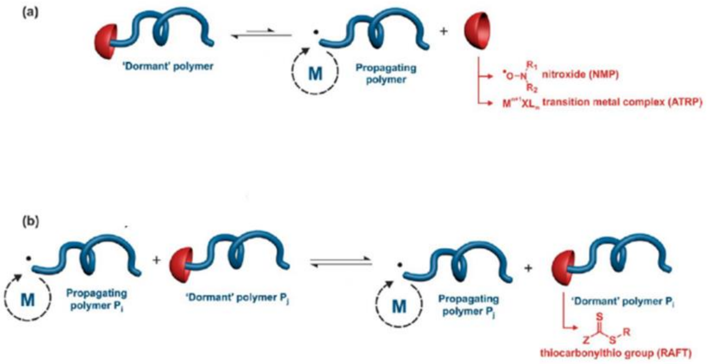

Figure 2.1: Reversible-deactivation radical polymerization (RDRP) based (a) on a reversible termination mechanism or (b) on a degenerative transfer mechanism. reproduced with permission from ref [8]

2.1.1 Living character and Block copolymers

The living behavior of RDRP allowed it to obtain architectures that were impossible to reach with free radical polymerizations. In particular, a living polymer chain is a macromolecule able to be extended, even after the complete consumption of the monomer, by further monomer addition (the same monomer or a completely different monomer). However, it should be considered that termination occurs in RAFT polymerizations as well as in ATRP and NMP polymerizations. As conversion increases, termination reactions become more prevalent relative to propagation in all radical polymerizations.

Block copolymers (BCPs) are a specific class of macromolecules in which chemically distinct monomer units are grouped in discrete homopolymer blocks along the polymer chains. They can have different architectures depending on: (i) the number of chemically distinct blocks and (ii) the relationship between linear sequences and ramifications in the blocks themselves. Respect to polymer blending the behavior of block copolymers is particularly interesting due to the covalent bond that connects the two blocks. The presence of the junction points avoid separation of the two homopolymers, even if they are immiscible. Even if macroscopic separation is not possible to the microscopic level, different morphologies are achieved in bulk or solution, derived from self-assembly of the two, or more, blocks of the same macromolecule. This process is known as microphase separation [10] and self-organization in cylindrical, spherical, lamellar, and other shapes have been revealed both experimentally and theoretically in bulk.[11] The microphase separation is driven by unfavorable mixing enthalpy coupled with small mixing entropy, and can be controlled by three important parameters: (i) the volume fraction of the A and B blocks (f_A and f_B), (ii) the total degree of polymerization ($N = N_A + N_B$) and (iii) the Flory-Huggins interaction parameter (χ_{AB}). The latter is reported in equation 2.1 and indicate the degree of incompatibility between A and B which govern the phase separation:

$$\chi_{AB} = \left(\frac{z}{k_B T}\right)\left[\epsilon_{AB} - \left(\frac{1}{2}\right)(\epsilon_{AA} + \epsilon_{BB})\right] \qquad (2.1)$$

Where z is the number of nearest neighbors per repeat unit, k_B is the Boltzmann constant, $k_B T$ the thermal energy, and ϵ_{AA}, ϵ_{BB} and ϵ_{AB} are the attractive interaction energies between molecules of the same type (A-A and B-B) and of different nature (A-B).

The introduction of solvent increase the level of complexity because in solution additional interactions occur and the χ interaction parameters of each block with the solvent, with each other and themselves must be considered. The diblock copolymer can behave as amphiphilic, double solvophilic or double solvophobic depending on the solubility of both blocks with the selected solvent. Among these, the amphiphilic polymers are the most interesting because self-assembly can occur in the so called selective solvent, meaning the one in which just one of the two blocks is soluble. In this case solvophobic effect and hydration forces govern the self-assembly and they depend on the amphiphilic polymer concentration in the solvent. In particular, the polymer starts to self-assemble over a specific concentration, known as critical aggregation concentration (CAC). Likewise block copolymers in bulk, also in this case the aggregation occurs to minimize the free energy by balancing the solvophobic effect and hydration forces in terms of area per molecule. The morphology of the aggregate is primary determined by the packing parameter $p = v/a_0 l_c$, where v is the volume of solvophobic segment, a_0 is the contact area of the head solvophilic group and l_c is the length of the solvophobic segment.[12] Highly solvophilic portion with very large optimal headgroup area and small solvophobic-chain volume ($p < 1/3$) will assemble into spherical micelles. When the mismatch between the headgroup area and solvophobic-chain volume is reduced ($1/3 \leq p \leq 1/2$) rod-like or cylindrical micelles are formed. Finally, if the solvophobic part is predominant ($1/2 \leq p \leq 1$) self-assemble to form membranes.

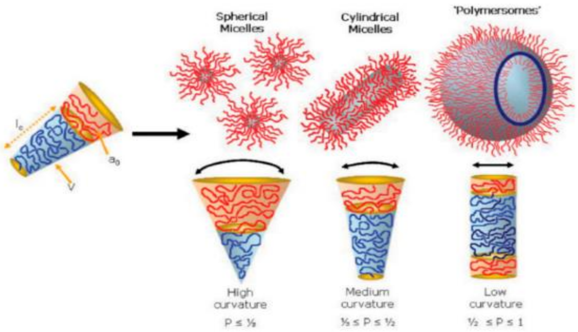

Figure 2.2: Nanostructures of amphiphilic diblock copolymers due to the inherent curvature of the polymer, as estimated by the chain packing parameter, p. Reproduced with permission from ref [12].

2.2 Reversible Addition-Fragmentation chain Transfer (RAFT) polymerization

Among the class of RDRP polymerizations RAFT stands as the most versatile protocol, providing for the facile synthesis of complex architectures for a wide variety of functional monomers and various polymerization conditions (organic and aqueous solution, bulk, emulsion, dispersion).[9,13] RAFT was first developed at the Commonwealth Scientific and Industrial Research Organisation (CSIRO), in Australia, and announced in 1998.[14] The living free-radical character of the polymerization was achieved by the addition of thiocarbonylthio-containing organic molecules (Z–C(=S)S–R), also called CTA (chain transfer agent) or RAFT agents. The CTA is able to reversibly react with the (macro)radical during propagation by a chain transfer mechanism, the so formed macro-CTA act as a dormant species ready to react again with another radical (details of the mechanism in *section 2.2.1*). The overall process is an insertion of the monomers between the S–R bond of the CTA. The characteristic high control of RAFT polymerization is a consequence of the continuous switching between propagating and dormant states. In this way termination reactions can be considered negligible, and control over the molecular weight, together with narrow dispersity (Đ) and defined molecular architectures are easily achieved.

2.2.1 RAFT Mechanism

The introduction of the chain transfer agent produces a new equilibrium that cannot be observed in the uncontrolled free radical process. This addition-fragmentation equilibrium shown in the **Figure 2.3** is the most important step in RAFT mechanism.[15]

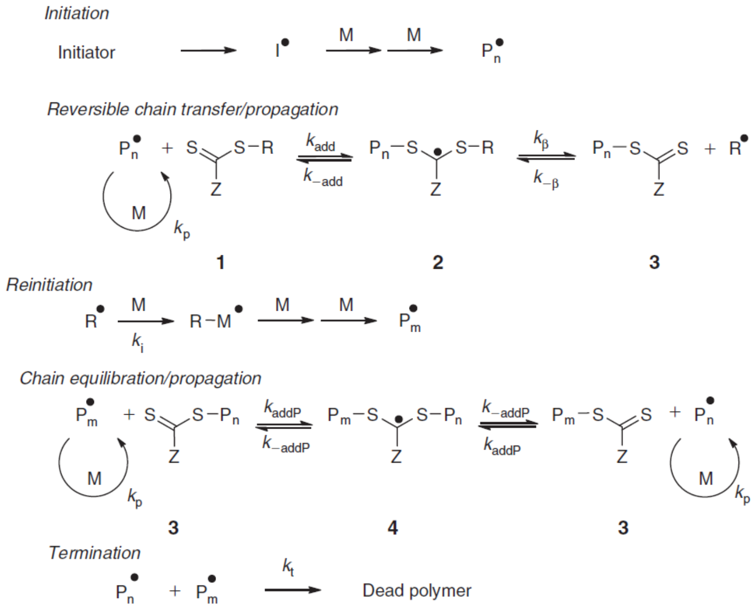

Figure 2.3: Mechanism of RAFT process.

As in free-radical polymerization, RAFT first step includes an external initiator able to generate the first radical oligomeric species. The most common initiators are thermal unstable molecules such as AIBN but also photo-initiators. The small radical oligomer can now reacts with the CTA [(Z–C(=S)S–R (**1**)], this reversible chain transfer step is governed by the relative reactivities of the C=S bond and the propagating radical ($P_n^\bullet$). After the formation of the intermediate radical (**2**) fragmentation of the latter provides the dormant species, which is the polymeric thiocarbonylthio compound [(P_n–C(=S)S–Z (**3**)]. The new radical ($R^\bullet$) acts as initiator generating a new propagating radical chain ($P_m^\bullet$). When the two propagating radicals ($P_n^\bullet$ and $P_m^\bullet$) reach similar length, in terms of monomer repeating units, a rapid equilibrium with the dormant CTA-capped species (**3**) is established by the way of intermediate (**4**). This is the crucial step of the whole process since it provides equal probability for the chains to grow meaning low dispersity of the final chains. This is due to the fact that the concentration of polymer propagating radicals remains lower than intermediate (**4**), which is more stable, so that radical-radical termination reactions are negligible. A requirement for this process to be controlled is the rapidity of the equilibrium ($k_{addP} \gg k_p$ and $k_\beta \gg k_p$).

The final polymer will have the thiocarbonylthio group to the majority of the chains ω-end. This species is called macro-CTA or macro-RAFT agent because it is able to re-initiate a second polymerization with fresh monomer allowing the production of block copolymers (as already discussed in *section 1.1.2*), and opening the door to various complex architectures such as, stars, branched, surface grafting or nanoparticles.[16–19] The livingness of the final system is measured by the number of chains which terminate with a CTA end group. Since the probability of two propagating macro radicals to react is very low the amount of dead chain in RAFT polymerization depends on the number of initiating radicals generated in the very first step. Which means that few polymer chains will have an initiator fragment at the end of the chain instead of the CTA. This feature is a great advantage because by tuning the amount of initiator also the livingness of the system can be easily manipulated. However, dead chains may also results from chain transfer to solvent, polymer and monomer becoming an issue when targeting high molar mass or with particular monomers and solvents.

2.2.2 Kinetic and parameters

RAFT transfer constant

The efficiency of the RAFT polymerization is related to the equilibrium in the initialization and chain equilibration phases and can be determined by two transfer constant $C_{tr} = k_{tr}/k_p$ and $C_{-tr} = k_{-tr}/k_{-\beta}$. The rate of transfer ($k_{tr}$) in its turn depends on two factors: the addition rate of the propagating (macro)radical ($P_n^\bullet$) to the RAFT agent and the partition coefficient (φ), which describe the partitioning of the intermediate radical (**2**) between starting material and the product:

$$k_{tr} = k_{add}\phi = k_{add}\frac{k_\beta}{k_{-add} + k_\beta} \qquad (2.2)$$

The transfer agent radical ($R^\bullet$) which result from the partitioning can take two pathways, adding back to the macro-RAFT or react with a monomer. For this reason it is possible to define another rate coefficient k_{-tr} associated with this partitioning:

$$k_{-tr} = k_{-\beta}\phi_\beta = k_{-\beta}\frac{k_{-add}}{k_{-add} + k_\beta} \qquad (2.3)$$

The parameters in equations (2.2) and (2.3)[20] are important to evaluate the RAFT agent activity. For example for high reactive transfer agents toward radical addition, C_{-tr} is seldom zero while in less active agents $C_{-tr} \leq 1$.

Molecular mass and living fraction

Living radical techniques, unlike conventional radical polymerizations, are able to achieve good predetermination of the polymer molecular weight distribution starting from the concentration of the monomer and other reagents, as reported in the equation 2.4. The result of this equation have a good match with the experimental molecular weight.

$$M_{n,th} = \frac{[M]_0 p M_M}{[CTA]_0 + 2f[I]_0(1 - e^{-k_d t})(1 - \frac{f_c}{2})} + M_{CTA} \qquad (2.4)$$

where $[M]_0$, $[CTA]_0$ and $[I]_0$ are the initial concentrations of monomer, chain transfer agent and initiator respectively, k_d the decomposition rate coefficient of the initiator, p is the monomer conversion and, M_M and M_{CTA} the molar masses of monomer and chain transfer agent respectively. The terms $2f$ in the equation indicates that from one initiator molecule two radicals are obtained with a certain efficiency f. Whereas the term $1 - \frac{f_c}{2}$ represents the number of chains produced in a radical termination event with f_c the coupling factor (if $f_c = 1$ termination occurs only by combination whereas if $f_c = 0$ only by disproportionation).

The equation 2.4 can be approximate as follow:

$$M_{n,th} = \frac{[M]_0 p M_M}{[CTA]_0} + M_{CTA} \qquad (2.5)$$

Note that the living character (where the number of living fractions can be calculated through equation 2.6) is imparted only when the molar mass or the polymer is lower than the one obtained with the same conditions but without using the RAFT agent. This is the only way to have a number of polymer chains that far exceeds the number formed as a consequence of termination. For this reason the well-known limitation of all RDRP systems is the limited range of molecular weight while keeping good control over dispersity and end-group functionality. Nevertheless, there are some polymerization techniques and particular experimental conditions which allow to obtain ultrahigh molecular weight (UHMW) polymers.[9]

$$L = \frac{[CTA]_0}{[CTA]_0 + 2f[I]_0(1 - e^{-k_d t})(1 - \frac{f_c}{2})} \qquad (2.6)$$

The livingness of the system, which means the number of end-capped chains with thiocarbonylthio group, depend by initiator concentration (both I and CTA) and can be improved by reducing the amount of $[I]_0$. Additionally, changing the f and k_d parameters can increases the rate (as shown below) decreasing the livingness. On the other hand, monomers with high k_p and low k_t allow rapid polymerization with low loss of chain end fidelity.

Rate of polymerization

The polymerization rate of the RAFT process follows the one of a common radical polymerization and can therefore be manipulated by a series of parameters as shown in the equation 2.7.

$$R_p(t) = k_p[M]\sqrt{\frac{f k_d [I]_0 e^{-k_d t}}{k_t}} \qquad (2.7)$$

Where R_p is the polymerization rate, k_p the propagation rate coefficient, $[M]$ the monomer concentration, f the initiator efficacy, k_d the decomposition rate coefficient of the initiator, $[I]_0$ the initial initiator concentration and k_t the termination rate coefficient.

As previously introduced, reducing the initiator concentration is a key to end up with good value of living fraction but it decrease the R_p. It is important to notice that not only the initiator concentration is involved in the equation and so it is still possible to optimize the rate of polymerization even keeping low $[I]_0$. For instance monomers with high propagation rate or initiators with high efficiency or high decomposition rate can lead to faster polymerization.

2.2.3 RAFT agents

Over the years RAFT agents with different chemical structures have been synthesized and tested for polymerization of various monomer families.[21,22] The chemical nature of both the R and Z groups of the CTA (**Figure 2.4**) is pivotal for their effectiveness in the polymerization. In particular, depending on the electronic properties of the two functionalities, those can deactivate or activate the thiocarbonyl C=S bond, modifying the stability of intermediates radicals (**2**) and (**4**). For a correct insertion of the monomer the reactivity of the RAFT agent should be higher than the one of the vinyl monomer bond.

The most used CTAs can be divided in four major families: dithioesters (Z = alkyl or aryl), trirhiocarbonates (Z = S-alkyl), xanthates (Z = O-alkyl), and dithiocarbamates (Z = NR'R") depending on the R and Z groups chemical nature.

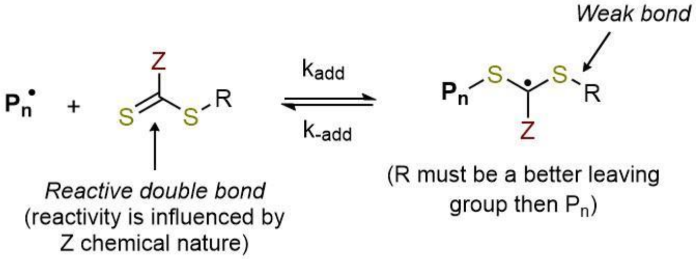

Figure 2.4: General structural features of the RAFT chain transfer agent

RAFT agents selection

One of the advantages of RAFT radical character is its ability to be applied to a wide range of monomers. This last can be considered as belonging to two broad classes in terms of reactivity and stabilization of the propagating radical. The ’more-activated’ monomers (MAMs) have their vinyl group conjugated with a double bond (*i.e.*, butadiene, isoprene), an aromatic ring (*i.e.*, styrene, vinylpyridine), a carbonyl groups (*i.e.*, (meth)acrylates and (meth)acrylamides) or a nitrile (*i.e.*, acrylonitrile). The ’less-activated’ monomers (LAMs) are those in which the double bond is close to a saturated carbon (*i.e.*, DADMAC), nitrogen or oxygen lone pair (*i.e.*, vinyl acetates, N-vinylpyrrolidone) or the heteroatom of an heteroaromatic ring (*i.e.*, N-vinylcaprolactam). Among all the monomers, those which have functionalities that may undergo side reactions with the thiocarbonylthio group (such as primary alcohol or amine nucleophilic substituents) are more challenging but can be used by fine tuning the reaction conditions. A key aspect in the choice of the more suitable RAFT agent is that the reactivity of C=S bond must be higher than the reactivity of C=C bond, this is achieved by careful selection of Z and R groups [21].

The role of the Z group The Z group influences the stabilization of the intermediates (**2**) and (**4**), and activate or deactivate the C=S bond to monomer addition, which means that modify both the addition rate of the propagating radical $P_n^\bullet$ to the RAFT agent and the fragmentation rate. In case of trithiocarbonates (Z = S-alkyl) or dithiobenzoates (Z = Ph) the radical is more stabilize and the C=S bond more reactive favoring the addition of MAMs (since they are less reactive in radical addition, lower k_p and k_{add}, more reactive RAFT agents are required for good control) but obtain poor control over LAMs. On the other hand in xhantates (Z = O-alkyl) and dithiocarbamates (Z = N-alkyl) the lone pair of oxygen and nitrogen destabilize the intermediate radical and reduces the C=S double-bond character making the radical addition more difficult. For these reasons they are more suitable for LAMs (since they are highly reactive in radical addition, higher k_p and k_{add}) but are inert over MAMs addition. When the nitrogen is part of an heteroaromatic ring or close to an electron withdrawing group, such as a carbonyl, the lone pair is less available and the reactivity is similar to that of dithioesters and trithiocarbonates.

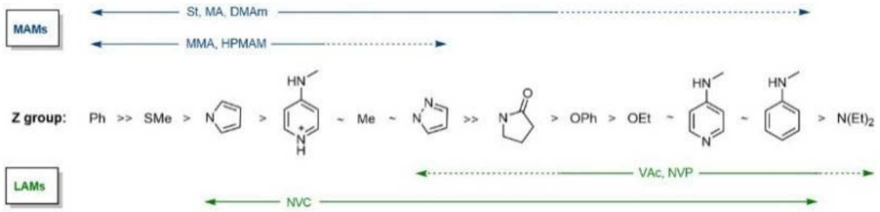

Figure 2.5: Guidelines to Z group selection depending on the monomer.

The role of the R group R group influences the radical addition to the CTA by controlling the C=S reactivity in a similar way as the Z group. Furthermore, the R group nature is important for radical intermediate fragmentation (partition coefficient φ), as it has to be a good leaving group, and propagation because of $R^{\bullet}$ become the new initiator of the polymerization and has to ensure that all the chains initiate in the same time frame to obtain low dispersity ($k_i > k_p$). A fine balance between radical stability and steric effects must be reached. In general, $R^{\bullet}$ must be a better leaving group than the propagating polymer $P_n^{\bullet}$ so for MAMs a more branched radical is needed in order to favor the partition over the product. Whereas a primary radical is enough for LAMs polymerization. This is very important regarding block copolymer synthesis; if poly(MAM)-*b*-poly(LAM) polymers want to be achieved the block comprising MAMs need to be synthesized first. $PolyLAM^{\bullet}$ are poor homolytic leaving groups with respect to $PolyMAM^{\bullet}$ and, consequently poly(LAM) macro-RAFT have very low transfer coefficient for MAMs polymerization.

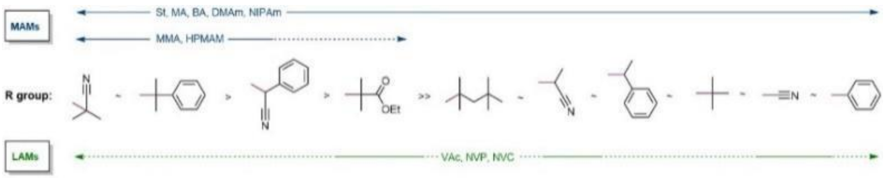

Figure 2.6: Guidelines to R group selection depending on the monomer.

2.3 Photoinduced Electron/Energy Transfer (PET)-RAFT polymerization

The combination of photocatalysts with polymer chemistry for the synthesis of precisely defined macromolecules has emerged only recently. In fact, the prospect of initiating polymerization[23] and, more recently, depolymerization,[24,25] through external stimuli has garnered considerable attention. Among these stimuli, the use of light as an activation source holds tremendous appeal. This is due to the inherent spatial and temporal control of electromagnetic irradiation, coupled with its low process costs, minimal environmental impact, and adjustable intensity and wavelength modulation. Notably, light permits reactions to be conducted in situations where elevated temperatures, rigorous reaction conditions, or the need for deoxygenation would not be tolerated.[26] Specifically, since the seminal work by Otsu and coworkers,[27] which introduced thiocarbonylthio compounds as photoiniferters (where "inifert" stands for initiator-transfer agent-terminator),[28] the photoactivation of chain transfer agents has attracted substantial investigation. In so doing, RAFT polymerization has evolved into a more versatile technique, owing to the alternative activation of the RAFT agent through a photo-redox catalyst (PC). This activation occurs via a photoinduced energy/electron transfer process and it is known as PET-RAFT.

The scientific path that led to the development of PET-RAFT techniques began with initial studies about direct photoactivation of the CTA using γ-radiation, leading to non-specific radical generation and irreversible termination.[29] Then, direct activation of CTAs under UV light has been extensively analyzed and reviewed.[30] The latter is possible due to the weak n to π* absorption of specific thiocarbonylthio compounds within the UV-Vis spectrum. These compounds, as initially proposed by Otsu, act as photoiniferters, initiating, transferring, and terminating processes upon light exposure. Despite not requiring initiators or catalysts in this approach, the high-energy electromagnetic irradiation associated with UV light caused the loss of end-group fidelity due to the photolysis of the RAFT agent, thus diminishing the "living" character of the process, as demonstrated by Davis et. al.[31] While the polymerization exhibited living characteristics at low monomer conversion, prolonged irradiation times resulted in a significant broadening of the molecular weight distribution due to the decomposition of the chain-termini. In fact, UV light has been afterwards employed for post-modification removal of the RAFT group through thiocarbonylthio-end degradation.[32] As a result, there has been a trend in recent years to shift towards longer wavelength radiation (400-700 nm) to eliminate side reactions. Finally, in 2014 an innovative contribution by Boyer et al. marked a significant milestone in merging visible light photoredox catalysis and the photoiniferter characteristics of the chain transfer agents, resulting in the development of PET-RAFT technology.[33] This process, named photoinduced electron/energy transfer (PET)-RAFT, is founded upon a novel approach of activating thiocarbonylthio compounds using photoredox catalysts (PCs), yielding a range of advantages compared to traditional RAFT protocols. Foremost, this method circumvents the initiation step of RAFT with exogenous radical sources, which can lead to undesirable α termini (via direct initiation) or ω termini (via termination of the growing chain by an exogenous radical),[34] by employing of the photocatalyst. Additionally, the use of PCs obviates the need for reaction heating, permitting polymerization at low temperatures in the presence of oxygen. Furthermore, the use of light as an external stimulus grants spatiotemporal control, given the ability to switch the lamp ON and OFF. This feature not only provides enhanced process control but also ensures orthogonality with other controlled polymerization techniques.

2.3.1 PET-RAFT mechanism

Although the RAFT mechanism is well-established, as described in *section 2.2.1*, the interaction between the excited photoredox catalyst (PC*) and the CTA remains a subject of ongoing investigations. Currently, there are two proposed mechanisms,[35,36] illustrated in **Figure 2.7**. The first possible mechanism involves a photoinduced electron transfer from the excited state of the PC to the RAFT agent, causing it to become a thiocarbonylthio anion. This transformation is made possible by the stronger reduction potential of the photoredox species with respect to the CTA. Subsequent fragmentation of this anion forms the initiating species ($R^{\bullet}$ or $P_n^{\bullet}$). These radicals can further interact with both the reduced RAFT agent and the oxidized PC, generating a dormant macro-CTA and closing the catalytic cycle. The second possible pathway follows a photo-induced energy transfer mechanism. In this scenario, energy is transferred through an electron exchange mechanism, giving rise to an electronically excited

RAFT species. This excited species then undergoes fragmentation to yield propagating radical and ZCS_2 radical, which eventually recombine with an active chain (iniferter-type process, leading to the formation of a dormant polymer chain. This energy transfer is believed to follow a Dexter electron exchange pathway (P3T, photoinduced triplet energy transfer), wherein the electron is transferred from the excited state donor to the ground state acceptor. Concurrently, a ground-state electron is transferred back to the donor species, resulting in no net gain or loss of electrons among the molecules involved. This exchange of electrons, however, does lead to the transfer of energy.

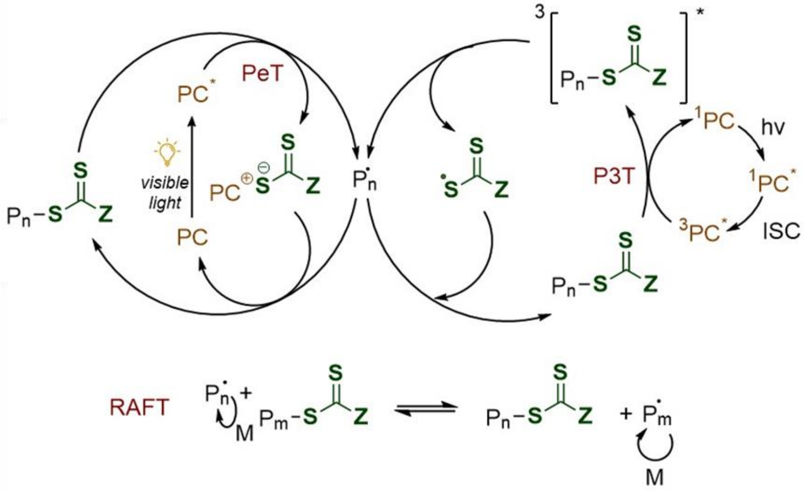

Figure 2.7: Proposed mechanisms for PeT (left) and P3T (right) RAFT polymerization. PC: photocatalyst; PeT: photoinduced electron transfer; P3T: photoinduced triplet energy transfer (Dexter electron exchange); ISC: intersystem crossing; *: excited state.

The mechanism strongly depends on the PC nature and cannot be universally applied to all other photocatalysts, as demonstrated by various computational studies.[37–39]

2.3.2 Photoredox catalysts

PET PET-RAFT polymerization was firstly developed using a very known photoredox catalyst in organic synthesis, specifically (*fac*-Ir(ppy)$_3$, Ir $^{(III)}$).[33] This catalyst was applied across a diverse range of monomers, encompassing both conjugated and non-conjugated types such as (meth)acrylates, styrene, (meth)acrylamides, and vinyl esters under low-power visible light. The PET-RAFT system was subsequently adapted for use in aqueous media in a subsequent work by employing a water-soluble ruthenium catalyst, (Ru(bpy)$_3$Cl$_2$, Ru$^{(II)}$).[40] Moreover, it was shown for the first time that the polymerization could be activated and deactivated by light, effectively creating an "ON" and "OFF" kinetic trend. In the subsequent years, a broad array of photocatalysts for PET-RAFT polymerization were explored, as depicted in **Figure 2.8**. This exploration encompassed naturally derived photoactive compounds, as well as metal-free organic catalysts, signifying a move towards more environmentally friendly polymer manufacturing processes. Among them, porphyrins and metalloporphyrins are noteworthy functional molecules characterized by a large conjugated ring structure and extended absorbance in the visible region of the electromagnetic spectrum. In nature, they are present as chlorophyll, heme, and VB12. The exploration of porphyrins as photocatalysts in PET-RAFT commenced with chlorophyll *a* (Chl *a*),[41] which demonstrated the ability to effectively activate the polymerization. Subsequently, bacteriochlorophyll *a* (BChl *a*)[42] was also investigated due to its absorption at long wavelengths, ranging from red to near-infrared (NIR). This attribute allowed the utilization of lower-energy radiation with deep light penetration which can be interesting for biomedical applications. The initial studies involving chlorophyll lay the foundation for the examination of various non-toxic and low-cost metalloporphyrins containing non-precious metals. Among them, zinc porphyrins, particularly 5,10,15,20-tetraphenyl-21H,23H-porphine zinc (ZnTPP), emerged as efficient catalyst of PET-RAFT polymerization of trithiocarbonate compounds.[43,44] ZnTPP offered certain advantages over other transition metal complexes, including a shorter inhibition period in the presence of oxygen, likely due to specific interactions between Zn and trithiocarbonate sulfur atoms resembling natural interactions. Metal-free porphyrins, such as tetraphenylporphyrin (TPP), was also shown to activate polymerization, although with somewhat lower efficiency.[45] To enhance their effectiveness, covalent conjugation with CTAs was employed, creating acceptor-donor molecules. Metal-free PET-RAFT polymerization was further provided by the use of organic dyes, such as Eosin Y (EY), fluorescein, Rhodamine 6G, Nile red, and 10-phenylphenothiazine (PHT). Among these options, only EY and PHT demonstrated effectiveness.[46,47] Furthermore, inorganic semiconducting metal oxides, including TiO_2,[48,49] and ZnO,[50] were harnessed as photocatalysts for PET-RAFT polymerization.

The aforementioned photoredox catalysts constitute just a fraction of the diverse classes suitable for PET-RAFT polymerization. Less common but still notable options include lead-halide perovskite nanocrystals ($CsPbBr_3$),[51] CdSe quantum dots (QDs),[52,53] tertiary amines (such as tris(2-(dimethylamino)ethyl)amine, pentamethyldiethylenetriamine, and triethylamine),[54] and graphitic carbon nitride.[55]

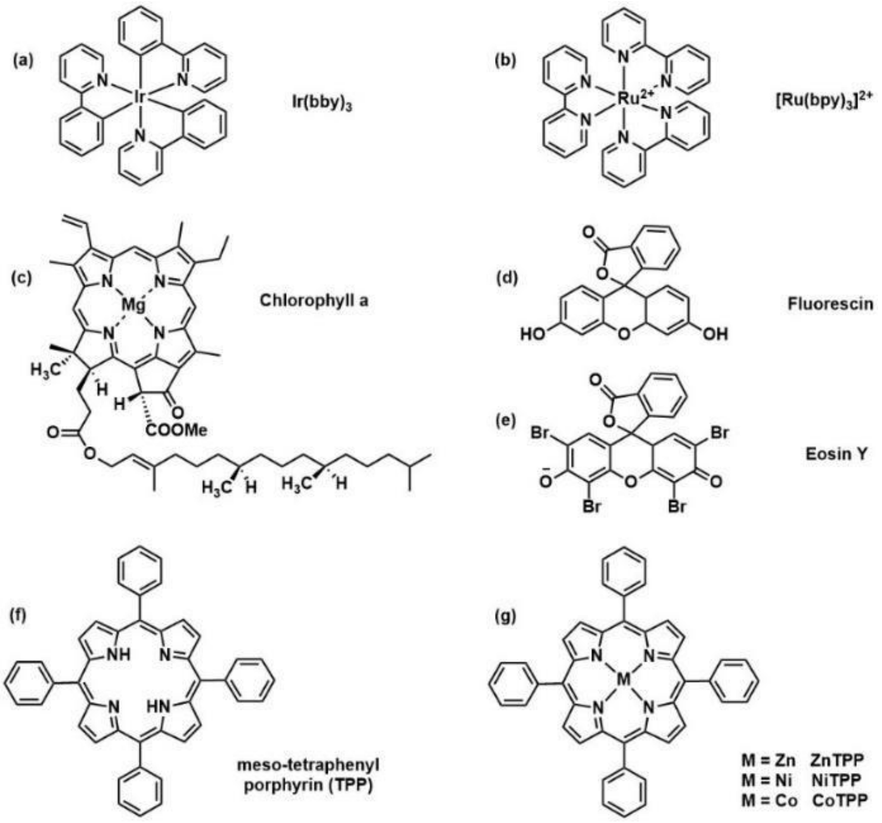

Figure 2.8: Selection of catalyst structures: ($Ir(ppy)_3$), [34] ($Ru(bpy)_3Cl_2$), [41] chlorophyll *a*,[42] Fluorescine, [46] Eosine Y, [46] and (metallo)porphyrin-based structures.[44]

Finally, Heterogeneous catalysis offers a promising avenue for advancing environmentally friendly PET-RAFT polymerization. Incorporating photoredox catalysts within the polymeric matrix, even at very low concentrations (ppm range), can potentially give rise to concerns related to toxicity, unwanted side reactions, and polymer degradation. Consequently, the efficient removal and recycling of these photoredox catalysts have garnered significant attention within the scientific community. Heterogeneous systems such as magnetic ferrite nanoparticles,[56] semiconductor QDs,[57] photocatalytic nanoparticles,[58] or heterogeneous catalysts immobilized onto solid substrates,[59–61] have proven useful tools in recycling.

2.3.3 Light sources

The employment of electromagnetic radiation allows easy manipulation of the polymerization reaction just by adjusting the light intensity and wavelength together with precise spatiotemporal control. For these reasons, the choice of the light source is of paramount importance, as both wavelength and intensity play crucial roles in photochemical reactions. Wavelength correlates with the energy of photons and, consequently, with the transitions of electrons to higher energy orbitals. On the other hand, light intensity determines the quantity of photons (photon flux) that interact with the photocatalyst.[62] These factors collectively influence the polymerization rate and can be easily adjusted, providing an additional level of control over the chemical process. Among the various external light sources available nowadays, LEDs have gained prominence in recent years, owing to several advantageous characteristics (**Figure 2.9**). LEDs function based on electroluminescent emission, resulting in precise emission wavelengths with narrow half widths.[63] Additionally, LEDs require minimal voltage to operate, leading to reduced electricity consumption and generating less heat. Finally, they are cost-effective and boast an extended operational lifetime compared to other light sources, making them highly appealing for use in photochemical processes.

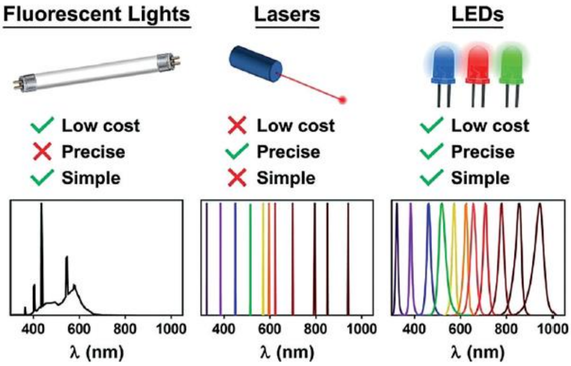

Figure 2.9: Main advantages of LED light sources.[62]

Photocatalysis in controlled polymerizations allows to achieve outstanding features which are possible only when light is used as an initiating source. By toggling the light source between "ON" and "OFF" states, the reaction can be instantly halted and reinitiated (**Figure 2.10**). Specifically, in the context of PET-RAFT polymerization, a dark environment prompts the RAFT agent to transition into a dormant state, as demonstrated in the pioneering study by Boyer et al.[64] This extraordinary capability is beyond the reach of thermally and chemically induced polymerizations, thereby expanding their range of applications.

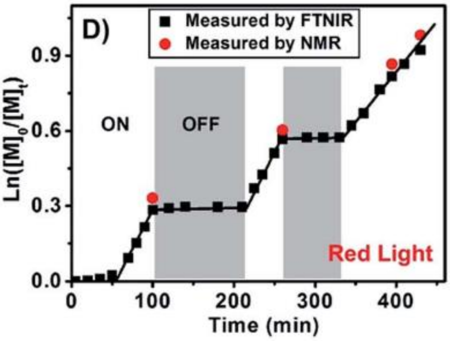

Figure 2.10: Temporal control of PET-RAFT technique. Reproduced with permission from ref. [42]

Beyond temporal regulation, light in combination with a radical process enables localized polymerization. This spatial control is achieved by activating polymerization exclusively in designated areas, facilitating the synthesis of materials with precisely tailored properties. This progress is made possible by the short life-time of both CTAs and PCs, ensuring that radical diffusion does not extend beyond a few nanometers.[65,66] Spatial control can be particularly significant for advancing techniques that heavily involve interfaces, such as lithography. The design of functional interfaces is a key factor for a wide range of industrial applications, which goes from optoelectronic devices to solar cells and biological active surfaces, and it is already been addressed in the past decades by reversible deactivation radical polymerization techniques such as ATRP and RAFT.[67] The introduction of surface-initiated (SI) control PET-RAFT polymerization in lithography allows, through the activation of targeted regions using photomasks, the one-pot synthesis of three-dimensional materials.

As an example Pester et. al. demonstrated the capability of PET-RAFT to selectively control film thickness on silica surfaces, utilizing the unique reaction control and high chain-end fidelity achieved through a Z-group approach for grafting the CTAs.[68] They successfully achieved intricate 3D topographical patterns through SI-PET-RAFT polymerization (**Figure 2.11**). Moreover, compatibility between photoinduced and traditional RAFT was addressed by subsequently extending the tethered block copolymer architectures through further reactions. Similarly, Seo an coworkers used Eosin Y as photocatalyst for SI-PET-RAFT polymerization of tridimensional polymer brushes exploiting the photomask technology.[69]

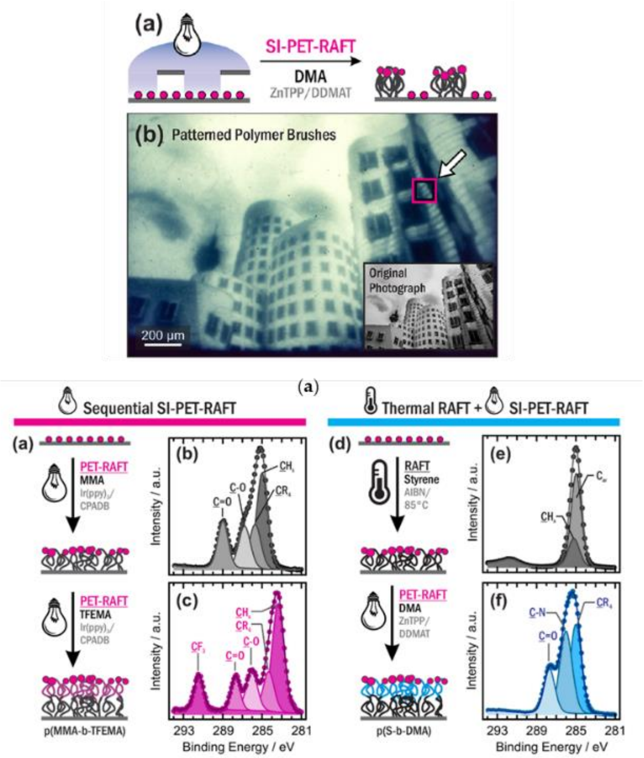

Figure 2.11: On the top: SI-PET-RAFT polymerization via localized irradiation of a CTA-functionalized substrate. Spatial control was achieved using a photomask on the SiO_2 substrate via reduction photolithography process. On the bottom: a combination of thermal initiated and photoinitiated RAFT polymerization. Reproduced with permission from ref. [69]

2.3.4 Oxygen tolerance

In conventional radical polymerization processes, the presence of oxygen can lead to termination reactions, necessitating the degassing of reaction mixtures through freeze-pump-thaw cycles and conducting polymerization under inert atmospheres. While effective, these methods involve time, costly gases, and complex equipment. PET-RAFT polymerization presents a valuable alternative that addresses this issue in terms of practicality, cost-effectiveness, and sustainability. Oxygen is known to be a radical scavenger in free radical polymerization, as it interacts with propagating radicals to generate peroxy species, thereby terminating the polymerization process. However, the PET mechanism inherently demonstrates tolerance to oxygen,[70] a property gained by a two-step process (**Figure 2.12**). First, the photocatalyst in the excited state is able to transfer its excitation to molecular oxygen, which is converted into singlet oxygen. The singlet species is far more reactive than the non excited oxygen and can react with reducing agents in the reaction mixture or the solvent itself, as demonstrated occurring in DMSO. Various singlet oxygen scavengers have been documented in the literature,[71] up to now only tertiary amines, ascorbic acid, anthracene, and limonene have been successfully used in open-air PET-RAFT polymerization.[72]

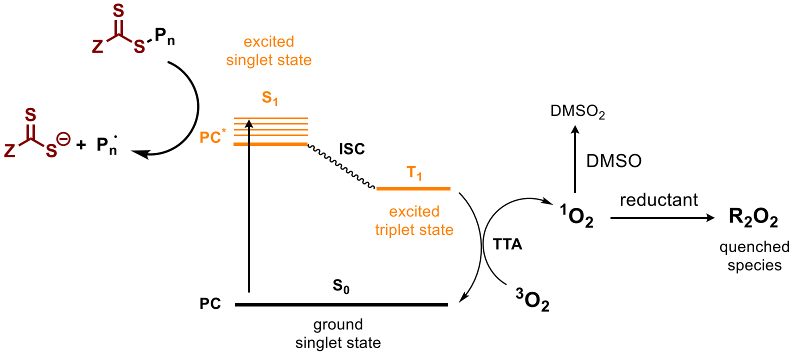

Figure 2.12: Schematic representation of the photophysic process involved in the intrinsic oxygen tolerance of PET-RAFT. ISC: intersystem crossing; *: excited state.

The intrinsic tolerance to oxygen of PET-RAFT, have paved the way for various implemented experimental protocols and applications that span from the synthesis of three-dimensional composite materials to biological applications, showcasing the versatility and potential impact of the approach. Among them high throughput synthesis, similar to biological reactions, allows for the facile and fast production of polymer libraries at very low reaction volumes into microliters scale. Polymeric libraries offers the practical advantages of a non-time-consuming systematic optimization of any polymerization protocol, reducing monomer and solvent waste.[73–75] Moreover, combination of polymer chemistry with biomedical science becomes easier, due to the mild reaction conditions, allowing the production of biomolecule-polymer conjugates. In fact, various polymer-protein bioconjugates have been produced, *i.e.* using BSA,[76] lipase,[77] or lysozyme,[78] and their biological activity has been retained. More impressively, Hawker and co-workers reported that polymer chain extension *via* EY/triethanolamine surface-initiated PET-RAFT was possible onto the surface of living yeast cells.[79] Finally, among the industrial applications of oxygen tolerant polymerization, photo-mediated 3D printing represent a remarkable example.[80–82] In this field, the oxygen tolerance characteristics, coupled with the polymerization's living nature and the ability to control the photo-polymerization in space and time, have been harnessed in the creation of intelligent materials capable of responding to environmental stimuli by altering their structure over time. This concept aligns with the notion of 4D printing.[83,84] As an outstanding example Boyer's group exploited PET-RAFT 3D printer to create sensitive water-soluble polymeric network with customized properties in a single-step process.[85] By varying durations and intensities of light exposure, they could alter the mechanical properties of the final material. The polymeric network was printed using decreasing amounts of light for each layer. When dehydrated the object flattened and then inverted its curvature (**Figure 2.13b**). In a separate work the living behavior of polymerization together with spatial control was exploited to induce bending in a preprinted strip.[86] Chain extension experiment on an already printed dormant object was performed, resulting in the creation of a 4D structure. When the printed strip was immersed in a growth medium containing the photocatalyst, a tertiary amine, and a fresh monomer after 30 minutes of exposure to green light, the strip exhibited significant bending (**Figure 2.13a**). Importantly, the bending occurred exclusively in the spatial region exposed to light, while the remaining part of the strip that remained in the dark retained its original shape.

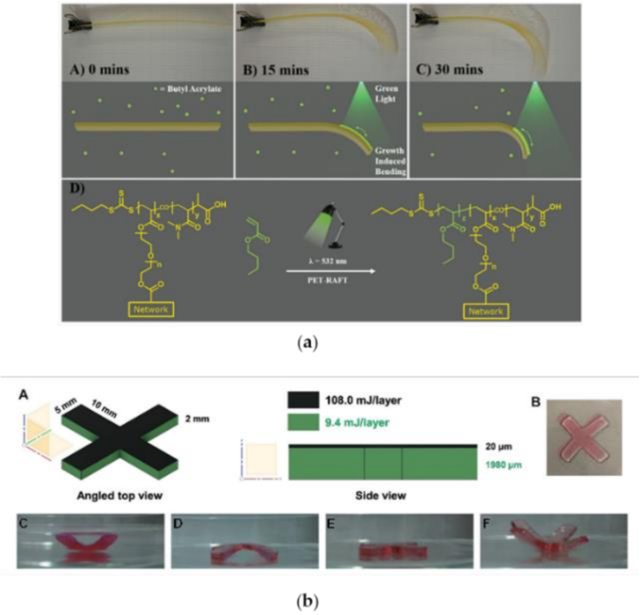

(a)

(b)

Figure 2.13: (**a**) Growth-induced bending process using PET-RAFT technique on a pre-printed strip. (**b**) Swelling induced actuation of spatially resolved 3D printed material in water. Reproduced with permission from ref.[86]

2.4 Depolymerization of RAFT-made polymers

Since the discovery of macromolecules the majority of the research has been focused on the synthesis of polymers, the understanding of the physical properties, and their applicability in a variety of fields. In fact, polymers have revolutionized modern industries and everyday life, offering lightweight, durable, and cost-effective solutions for countless applications. However, the extensive use and disposal of plastic products have given rise to an environmental crisis due to plastic pollution in terrestrial and marine ecosystems, causing serious threats to biodiversity, human health, and the overall well-being of the planet. For example, in 2015 of 6300 million tons of plastic waste produced, 12% were incinerated, 79% have been dispersed in the ground or the ocean, and only 9% could be recycled.[91,92] Consequently, there is an urgent need for innovative and sustainable strategies to manage plastic waste and reduce its impact. Polymer recycling can be categorized into various methods, including chemical, mechanical, and biological approaches. In particular, depolymerization by chemical means offers the potential to create a circular plastic economy, wherein plastics can be repeatedly broken down and remanufactured into new products, reducing the overall environmental footprint of plastic materials. It also mitigates the need for landfilling or incineration, which are associated with numerous environmental and health hazards.

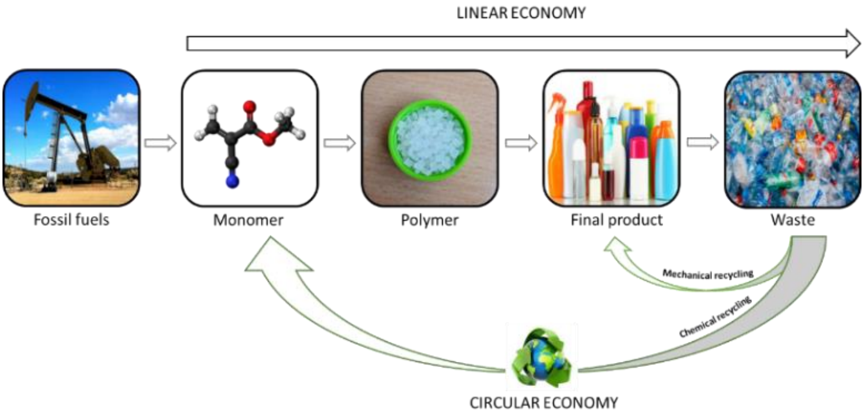

Figure 2.14: Production of plastic starting from the monomers to waste generation and ways to recycle the waste plastic in a more circular way.

Research in reversing the polymerization process has been overshadowed for many years due to the high stability of and resilience to degradation typic of plastic materials, which is the reason why they are so employed. However, chemical depolymerization is possible by selective breaking of the polymer backbone into its original building blocks, the monomers. This transformation allows for the recovery and reuse of the constituent monomers, offering a range of potential benefits. Nowadays, polymers prepared via polycondensation (*i.e.* polyesters) are easily depolymerized thanks to the presence of C-O or C-N labile bonds that can be susceptible to hydrolysis, aminolysis, methanolysis, etc. Much more difficult is to recycle polymers with C-C backbone (*i.e.* polyolefins) characterized by hydrolytic and thermal higher stability.[93] However this class of polymeric materials, including high-density polyethylene (HDPE), low-density polyethylene (LDPE), polymethyl methacrylate (PMMA), polyvinylchloride (PVC) and, polypropylene (PP), comprise the majority of industrial commercialized polymers. To overcome the high energy required for the carbon backbone to be fragmented polyolefins can be recycled through conventional methods such as pyrolysis, fluid catalytic cracking, and hydrocracking.[94] However those methods operates at very high temperatures, (from 500 °C to 900°C) and/or at elevated pressure making the process highly energy-intensive or unsuccessful due to degradation pathways becoming predominant at high temperatures.[91,95] In recent years, polymers produced through controlled polymerization techniques have shown increased susceptibility to depolymerization compared to their free radical counterparts. This susceptibility opens up new paths for depolymerization and offers numerous intriguing possibilities, both in terms of fundamental chemistry understanding and chemical recycling.

2.4.1 Thermodynamics of depolymerization

The reversibility of the propagation reaction in polymerization has been already described in terms of thermodynamic in 1948.[96] In a common addition polymerization reaction, the enthalpic contribution (ΔH) is negative due to the formation of a stable σ-bond, replacing the less stable π-bond (**Figure 2.15**). Furthermore, the degrees of molecular freedom is reduced as the monomer is converted into the polymer, which implies a negative entropic value (ΔS). The overall Gibbs free energy (ΔG), is negative for the propagation reaction (polymerization) and positive for the depropagation (depolymerization). The temperature at which the rate of propagation and depropagation are equal ($\Delta G = 0$) is known as ceiling temperature (T_c).

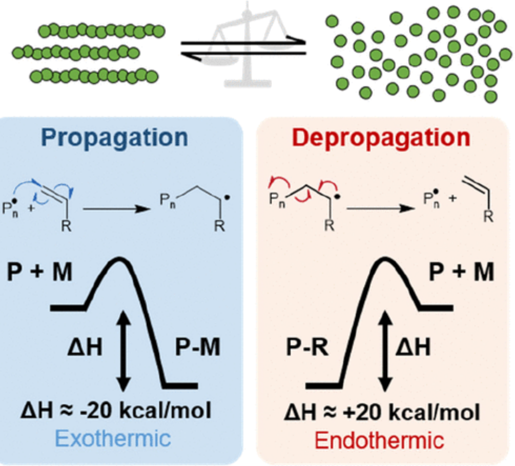

Figure 2.15: Thermodynamics of propagation vs depropagation undergoing radical polymerization/depolymerization. Figure reproduced from ref. [97]

The equilibrium constant is directly related to the Gibbs energy under standard conditions ($\Delta G°$) as reported in equation 2.9. K_{eq} is also defined as the ratio between the propagation and depropagation constants (k_p and k_{dp} respectively), which is consecutively related to the monomer concentration at equilibrium, $[M]_{eq}$ (equation 2.10). Based on this, if the reaction temperature is increased above the ceiling temperature (T_c) will cause the rate of depropagation to exceed the rate of polymerization. As a result, monomers will be produced until the new equilibrium concentration ($[M]_{eq}$) is reached.

$$\Delta G = \Delta H - T\Delta S \qquad (2.8)$$

$$\Delta G^{\circ} = -RTlnK_{eq} \qquad (2.9)$$

$$K_{eq} = \frac{k_p}{k_{dp}} = \frac{1}{[M]_{eq}} \qquad (2.10)$$

Usually, the T_c value is experimentally defined as the temperature at which there is no net monomer conversion, meaning that polymerization is no longer possible. A series of polymerization experiments are performed at increased temperatures and the results are plotted as monomer conversion *versus* temperature. The T_c values can be extrapolated or interpolated as the interception with the x-axis. Anyhow, the ceiling temperature often provides only a partial understanding of the depolymerization process. In fact, the T_c is defined considering the polymerization/depolymerization equilibrium between the monomer and the *active* propagating chains, not the terminated or capped polymer. This difference is crucial because a temperature that exceeds the T_c does not necessarily imply that the terminated/capped polymers would regenerate back the monomers. In fact, a critical prerequisite for a terminated or capped polymer chain to undergo depropagation is the supply of sufficient energy to break a bond and form an active species, such as a radical, anion, or cation. However, in practical terms, many terminated polymers can be "energetically trapped," meaning that their bonds cannot be easily cleaved to create a species capable of depropagation, even when heated above their ceiling temperature (T_c). Consequently, polymers can persist at temperatures well above their T_c, as in the case of polyolefin reported above. In empiric terms, the equilibrium between active chains and monomers, along with the concentration-dependent nature of the ceiling temperature, can result in depolymerization occurring at temperatures lower than the formally reported T_c.

2.4.2 Depolymerizing RDRP-polymers

For achieving an effective depolymerization under mild conditions two key challenges must be addressed: *(i)* generating the active polymer radical and *(ii)* designing the reaction in order to promote the depropagation of these radicals over propagation.

(i) The first challenge can be accomplished by considering controlled polymers instead of their respective free radical macromolecules. In fact, as we already explained at the beginning of this thesis, RDRP polymers are characterized by the presence of chain-ends that can be simply reactivated instead of the terminated chains of uncontrolled polymers. The ω-termini of controlled polymers in which the carbon backbone is bonded with heteroatoms (*i.e.* RAFT Z group) can be easily cleaved with the consequent formation of the active species. In this way the energetic barrier for the depolymerization to occur is lower even when the temperature is below the ceiling temperature.

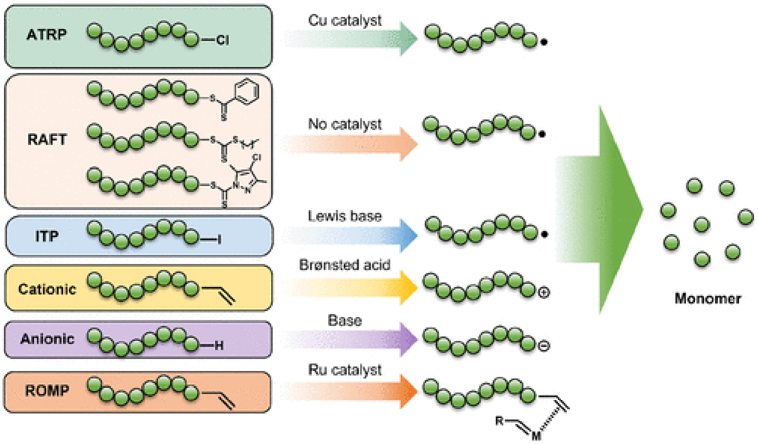

Figure 2.16: Activation of the ω-termini for different RDRP polymers and formation of the active species. Figure reproduced from ref. [97]

(ii) Regarding the second challenge, the ceiling temperature depends on the monomer structure together with the monomer concentration. In general, the lower T_c values are reported for polymers with bulkier side chains due to conformational and steric effects, making the propagation reaction more challenging and thus favoring the depropagation. On the other hand, for non-bulky polymers such as methyl methacrylate the reported ceiling temperature is around 200°C or higher.[96] However, due to the dependence of both T_c and $[M]_{eq}$ on the initial polymer concentration, increased the dilution can result in depolymerization at temperatures substantially lower than literature values of T_c. As an example when PMMA is depolymerized in dilute condition (1 M) the monomer can be regenerated at 205 °C, which is lower than the reported values for bulky polymerization (296 °C).[98]

Considering the two described consideration on how depropagation can be favored it was first reported in seminal independent works by the groups of Gramlich and Raus, that bulky bottlebrush polymers synthesized by either RAFT or ATRP could be depolymerized at very low temperatures, 70 °C and 90 °C respectively.[99,100] The perspective of these works were focused on improving the propagation of less reactive bulky monomers by suppressing the depropagation but the results set the foundation for efficient way to depolymerize RDRP-polymers. Starting from these outstanding results, the more challenging depolymerization of non-bulky polymers have been addressed. In particular ATRP-made polymers were tested for the depolymerization of PMMA using a ruthenium catalyst by the Ouchi's group and a copper catalyst by Matyjaszewski et al.[98,101,102] In the first case 24% monomer regeneration was registered at 120 °C which was improved in the second case, achieving up to 67% at 170 °C. In the case of RAFT polymers the Anastasaki's group exploited the T_c dependance on the polymer dilution developing an high efficient protocol for depolymerizing PMMA at 120 °C.[103,104] By diluting the initial polymer to 5 mM (respect to the repeating units) they obtained a near-quantitative depolymerization, up to 92% monomer regeneration in 8 hours. The low temperature suppressed the majority of side reactions and allowed it to either resynthesize the initial polymer or create a new material. It is worth noting that 100% depolymerizing of all "living" chains (*i.e.* chains containing the Z group) is possible and one has to fully eliminate side reactions occurring at high temperatures. However, 100% depolymerization of all chains ("living" and terminated chains) is not mechanistically feasible as RAFT-synthesized polymers inherently contain a certain extent of terminated chains and those would not be susceptible to depolymerization under relatively mild conditions. In addition, chains side reactions at high temperatures may also occur (*i.e.* Chugaev elimination) resulting in further loss of the end-group fidelity.

Notably, photothermal depolymerization of RAFT polymers were simultaneously developed by Sumerlin's and Anastasaki's groups in which light and a photocatalysis were used for improving the depolymerization kinetic and final yield at lower temperature (100 °C).[25,26] The use of light favors the homolytic scission of the C-S bond of the CTA, thus forming the active macroradical. A more detailed explanation of those systems will be provided in **Chapter 6**.

2.4.3 Future challenges

The depolymerization of controlled polymers opens the doors not only to more efficient and less energy-consuming polymer recycling procedure but also allows to increase the commercial appeal of RDRP polymers. This new-born approach still has to face several challenges. Among them: preserving the end-group fidelity, lowering the temperature, developing a control depolymerization procedure, expanding the polymer scope and its applicability to other RDRP techniques. Addressing these challenges will be essential for advancing the field of controlled polymer depolymerization and unlocking its full potential for sustainable materials and recycling solutions.

Preserving the end-group fidelity

As mentioned before the depolymerization of controlled polymers depends significantly on the presence of reactive end-groups to initiate depropagation. This approach is more energy-efficient compared to the alternative of inducing random chain scission to produce radicals capable of unzipping the polymer chains. However the chain-end loss heavily affects the depolymerization yield. In ATRP the halide loss by thermolysis can compete with the halide abstraction limiting the number of depolymerizable chains. In the same vein, thermal Chugaev-type elimination process has been proposed as an alternative pathway to the homolytic cleavage of the chain transfer agent. This results in the formation of a methacrylic macromonomer instead of a macroradical capable of undergoing the unzipping process. This demonstrates the importance of considering multiple reaction pathways and mechanisms in controlled depolymerization processes. Lowering the depolymerization temperature can be an effective method to suppress this side-reactions

Lowering the temperature

The monomer regeneration at low temperature is not only appealing in terms of preserving the chain-termini. For instance, low-temperature depolymerization has the potential to substantially decrease the energy requirements of depolymerization reactions. This makes depolymerization more economically attractive from both an industrial and commercial perspective, especially when it comes to chemically recycling commonly used commodity polymers. As possible methodologies to maintain high performance at lower temperatures we can imagine depolymerization under reduced pressure (moving the equilibrium toward the monomer regeneration),[98] increasing the polymer dilution, or using external stimulus such as light.[25,26]

Expand the polymer scope

The ceiling temperature is related to the monomer structure. The majority of the examples listed above concern only effective depolymerization of the polymethacrylate family. When we consider polyacrylates for example, which differ only by the absence of a methyl group along the carbon backbone, there are no evidence of chemical recycling.[105] This is due to the fact that the propagation constant values (k_p) are higher than the methacrylates analogues, so the polymers are more thermodynamically stable to the extent that they don't exhibit ceiling temperatures. Instead, they undergo degradation through alternative mechanisms at higher temperatures, such as mid chain radicals formation. The same behavior has been show for polyacrylamides which degrade before they can depolymerize.[106] Also polystyrene (PS) is still a challenging polymer to depolymerized but few reports suggest that ball-milling could be a valuable option for this very used commodity polymer.[107] Finally, the ability to depolymerizing polyolefins like polyethylene (PE) and polypropylene (PP) in an energy-efficient and cost-effective manner would be a significant environmental advancement. However, their high stability poses a considerable challenge for depolymerization. Recent pioneers works lay the foundations for a possible catalytic approach in this field which still require deeper investigation.[108,109]

Developing a control depolymerization procedure

RDRP polymers are synthesized through a control protocol, characterized by linear increase in the conversion over time, pseudo- first-order kinetics, and narrow dispersity (that decreases with the conversion). On the other hand, the same behavior in a reverse manner is not observed for depolymerization. For a control depolymerization to occur the end-groups should be rapidly removed to generate active chain ends. These active chain ends would then, in the presence of sufficient deactivation conditions, depropagate at rates that are identical to one another, resulting in a linear decrease in molecular weight as monomer units are generated. Efficient deactivation is pivotal in this process to ensure efficient capping of the depropagating radicals, minimizing termination reactions. If initiation is slow or deactivation is inefficient, some polymer chains may depolymerize rapidly, while others remain at their initial degree of polymerization. Moreover, the side reaction described above which causes the chain-end loss, can disrupt the controlled behavior. In the currently reported depolymerization of RAFT and ATRP polymers, controlled characteristics are not evident. Specifically, only a slight decrease in the molecular weight has been observed as monomers are generated, suggesting an "unzipping" behavior where depropagation occurs more rapidly than deactivation. This aspect is described in detail in **Chapter 6**.

2.5 References

[1] A. Goto, T. Fukuda, *Prog. Polym. Sci.* **2004**, *29*, 329–385.

[2] A. Gregory, M. H. Stenzel, *Prog. Polym. Sci.* **2012**, *37*, 38–105.

[3] J. Nicolas, Y. Guillaneuf, C. Lefay, D. Bertin, D. Gigmes, B. Charleux, *Prog. Polym. Sci.* **2013**, *38*, 63–235.

[4] K. Matyjaszewski, *Macromolecules* **2012**, *45*, 4015–4039.

[5] J. Chiefari, Y. K. B. Chong, F. Ercole, J. Krstina, J. Jeffery, T. P. T. Le, R. T. A. Mayadunne, G. F. Meijs, C. L. Moad, G. Moad, E. Rizzardo, S. H. Thang, C. South, *Macromolecules* **1998**, *31*, 5559–5562.

[6] K. Parkatzidis, H. S. Wang, N. P. Truong, A. Anastasaki, *Chem* **2020**, *6*, 1575–1588.

[7] A. Goto, T. Fukuda, *Prog. Polym. Sci.* **2004**, *29*, 329–385.

[8] J. Nicolas, *Chem. Mater.* **2016**, *28*, 1591–1606.

[9] S. Perrier, *Macromolecules* **2017**, *50*, 7433–7447.

[10] D. Gromadzki, *Rev. Environ. Sci. Biotechnol.* **2010**, *9*, 301–306.

[11] H. Feng, X. Lu, W. Wang, N. G. Kang, J. W. Mays, *Polymers (Basel).* **2017**, *9*, DOI 10.3390/polym9100494.

[12] A. Blanazs, S. P. Armes, A. J. Ryan, *Macromol. Rapid Commun.* **2009**, *30*, 267–277.

[13] G. Moad, E. Rizzardo, S. H. Thang, in *Aust. J. Chem.*, **2005**, pp. 379–410.

[14] J. Chiefari, Y. K. Chong, F. Ercole, J. Krstina, J. Jeffery, T. P. T. Le, R. T. A. Mayadunne, G. F. Meijs, C. L. Moad, G. Moad, E. Rizzardo, S. H. Thang, *Living Free-Radical Polymerization by Reversible Addition-Fragmentation Chain Transfer: The RAFT Process*, **n.d.**

[15] G. Moad, E. Rizzardo, S. H. Thang, in *Aust. J. Chem.*, **2012**, pp. 985–1076.

[16] G. Vaccaro, A. Bianchi, M. Mauri, S. Bonetti, F. Meinardi, A. Sanguineti, R. Simonutti, L. Beverina, *Chem. Commun.* **2013**, *49*, 8474–8476.

[17] A. Piloni, R. Simonutti, M. H. Stenzel, *J. Polym. Sci. Part A Polym. Chem.* **2019**, *57*, 1994–2001.

[18] M. Gregori, D. Bertani, E. Cazzaniga, A. Orlando, M. Mauri, A. Bianchi, F. Re, S. Sesana, S. Minniti, M. Francolini, A. Cagnotto, M. Salmona, L. Nardo, D. Salerno, F. Mantegazza, M. Masserini, R. Simonutti, *Macromol. Biosci.* **2015**, *15*, 1687–1697.

[19] A. Bianchi, M. Mauri, S. Bonetti, K. Koynov, M. Kappl, I. Lieberwirth, H. J. Butt, R. Simonutti, *Macromol. Rapid Commun.* **2014**, *35*, 1994–1999.

[20] *Handbook of RAFT Polymerization*, **n.d.**

[21] D. J. Keddie, G. Moad, E. Rizzardo, S. H. Thang, *Macromolecules* **2012**, *45*, 5321–5342.

[22] G. Moad, D. Keddie, C. Guerrero-Sanchez, E. Rizzardo, S. H. Thang, *Macromol. Symp.* **2015**, *350*, 34–42.

[23] K. Parkatzidis, N. P. Truong, M. N. Antonopoulou, R. Whitfield, D. Konkolewicz, A. Anastasaki, *Polym. Chem.* **2020**, *11*, 4968–4972.

[24] V. Bellotti, K. Parkatzidis, H. S. Wang, N. De Alwis Watuthanthrige, M. Orfano, A. Monguzzi, N. P. Truong, R. Simonutti, A. Anastasaki, *Polym. Chem.* **2022**, *14*, 253–258.

[25] J. B. Young, J. I. Bowman, C. B. Eades, A. J. Wong, B. S. Sumerlin, *ACS Macro Lett.* **2022**, *11*, 1390–1395.

[26] V. Bellotti, R. Simonutti, *Polymers (Basel).* **2021**, *13*, 1119.

[27] T. Otsu, A. Kuriyama, **n.d.**, 37–41.

[28] T. Otsu, *J. Polym. Sci. Part A Polym. Chem.* **2000**, *38*, 2121–2136.

[29] J. F. Quinn, L. Barner, T. P. Davis, S. H. Thang, E. Rizzardo, *Macromol. Rapid Commun.* **2002**, *23*, 717–721.

[30] T. G. McKenzie, Q. Fu, M. Uchiyama, K. Satoh, J. Xu, C. Boyer, M. Kamigaito, G. G. Qiao, *Adv. Sci.* **2016**, *3*, DOI 10.1002/advs.201500394.

[31] J. F. Quinn, E. Rizzardo, L. Barner, C. Barner-Kowollik, T. P. Davis, *Am.*

Chem. Soc. Polym. Prepr. Div. Polym. Chem. **2002**, *43*, 319–320.

[32] G. Moad, E. Rizzardo, S. H. Thang, *Polym. Int.* **2011**, *60*, 9–25.

[33] J. Xu, K. Jung, A. Atme, S. Shanmugam, C. Boyer, *J. Am. Chem. Soc.* **2014**, *136*, 5508–5519.

[34] D. J. Keddie, *Chem. Soc. Rev.* **2014**, *43*, 496–505.

[35] J. Phommalysack-lovan, Y. Chu, C. Boyer, **2018**, 6591–6606.

[36] N. Corrigan, S. Shanmugam, J. Xu, C. Boyer, *Chem. Soc. Rev.* **2016**, *45*, 6165–6212.

[37] N. Corrigan, J. Xu, C. Boyer, X. Allonas, *ChemPhotoChem* **2019**, *3*, 1193–1199.

[38] J. Christmann, A. Ibrahim, V. Charlot, C. Croutxé-Barghorn, C. Ley, X. Allonas, *ChemPhysChem* **2016**, 2309–2314.

[39] P. Seal, J. Xu, S. Luca, C. Boyer, S. C. Smith, *Adv. Theory Simulations* **2019**, 1900038.

[40] J. Xu, K. Jung, N. A. Corrigan, C. Boyer, *Chem. Sci.* **2014**, *5*, 3568–3575.

[41] S. Shanmugam, J. Xu, C. Boyer, *Chem. Sci.* **2015**, *6*, 1341–1349.

[42] S. Shanmugam, J. Xu, C. Boyer, *Angew. Chemie - Int. Ed.* **2016**, *55*, 1036–1040.

[43] S. Shanmugam, J. Xu, C. Boyer, *J. Am. Chem. Soc.* **2015**, *137*, 9174–9185.

[44] V. Bellotti, G. Beretta, R. Simonutti, *Polymer (Guildf).* **2023**, *271*, 125804.

[45] J. Xu, S. Shanmugam, C. Boyer, *ACS Macro Lett.* **2015**, *4*, 926–932.

[46] J. Xu, S. Shanmugam, H. T. Duong, C. Boyer, *Polym. Chem.* **2015**, *6*, 5615–5624.

[47] M. Chen, M. J. MacLeod, J. A. Johnson, *ACS Macro Lett.* **2015**, *4*, 566–569.

[48] B. F. Cheng, L. H. Wang, Y. Z. You, *Macromol. Res.* **2016**, *24*, 811–815.

[49] V. Bellotti, C. Daldossi, D. Perilli, M. D’Arienzo, M. Stredansky, C. Di Valentin, R. Simonutti, *J. Catal.* **2023**, *428*, 115074.

[50] E. Liang, M. sheng Liu, B. He, G. X. Wang, *Adv. Polym. Technol.* **2018**, *37*, 2879–2884.

[51] Y. Zhu, Y. Liu, K. A. Miller, H. Zhu, E. Egap, *ACS Macro Lett.* **2020**, *9*, 725–730.

[52] Y. Liang, H. Ma, W. Zhang, Z. Cui, P. Fu, M. Liu, X. Qiao, X. Pang, *Polym. Chem.* **2020**, DOI 10.1039/D0PY00588F.

[53] Y. Zhu, E. Egap, *Polym. Chem.* **2020**, *11*, 1018–1024.

[54] Q. Fu, T. G. McKenzie, S. Tan, E. Nam, G. G. Qiao, *Polym. Chem.* **2015**, *6*, 5362–5368.

[55] Q. Fu, Q. Ruan, T. G. McKenzie, A. Reyhani, J. Tang, G. G. Qiao, *Macromolecules* **2017**, *50*, 7509–7516.

[56] J. Wang, M. Rivero, A. Muñoz Bonilla, J. Sanchez-Marcos, W. Xue, G. Chen, W. Zhang, X. Zhu, *ACS Macro Lett.* **2016**, *5*, 1278–1282.

[57] K. P. McClelland, T. D. Clemons, S. I. Stupp, E. A. Weiss, *ACS Macro Lett.* **2020**, *9*, 7–13.

[58] S. Shanmugam, S. Xu, N. N. M. Adnan, C. Boyer, *Macromolecules* **2018**, *51*, 779–790.

[59] Y. Chu, N. Corrigan, C. Wu, C. Boyer, J. Xu, *ACS Sustain. Chem. Eng.* **2018**, *6*, 15245–15253.

[60] Y. Chu, Z. Huang, K. Liang, J. Guo, C. Boyer, J. Xu, *Polym. Chem.* **2018**, *9*, 1666–1673.

[61] M. Chen, S. Deng, Y. Gu, J. Lin, M. J. MacLeod, J. A. Johnson, *J. Am. Chem. Soc.* **2017**, *139*, 2257–2266.

[62] N. Corrigan, J. Yeow, P. Judzewitsch, J. Xu, C. Boyer, *Angew. Chemie - Int. Ed.* **2019**, *58*, 5170–5189.

[63] M. Sender, D. Ziegenbalg, *Chemie-Ingenieur-Technik* **2017**, *89*, 1159–1173.

[64] S. Shanmugam, J. Xu, C. Boyer, *Macromolecules* **2014**, *47*, 4930–4942.

[65] S. Shanmugam, J. Xu, C. Boyer, **2015**, DOI 10.1021/jacs.5b05274.

[66] C. Barner-Kowollik, G. T. Russell, *Prog. Polym. Sci.* **2009**, *34*, 1211–1259.

[67] C. Barner-Kowollik, A. S. Goldmann, F. H. Schacher, *Macromolecules* **2016**, *49*, 5001–5016.

[68] M. Li, M. Fromel, D. Ranaweera, S. Rocha, C. Boyer, C. W. Pester, *ACS Macro Lett.* **2019**, *8*, 374–380.

[69] S. E. Seo, E. H. Discekici, Y. Zhang, C. M. Bates, C. J. Hawker, *J. Polym. Sci.* **2020**, *58*, 70–76.

[70] J. Yeow, R. Chapman, A. J. Gormley, C. Boyer, *Chem. Soc. Rev.* **2018**, *47*, 4357–4387.

[71] S. C. Ligon, B. Husár, H. Wutzel, R. Holman, R. Liska, *Chem. Rev.* **2014**, *114*, 577–589.

[72] G. Ng, J. Yeow, J. Xu, C. Boyer, *Polym. Chem.* **2017**, *8*, 2841–2851.

[73] G. Ng, J. Yeow, R. Chapman, N. Isahak, E. Wolvetang, J. J. Cooper-White, C. Boyer, *Macromolecules* **2018**, *51*, 7600–7607.

[74] J. Yeow, S. Joshi, R. Chapman, C. Boyer, *Angew. Chemie* **2018**, *130*, 10259–10263.

[75] A. J. Gormley, J. Yeow, G. Ng, Ó. Conway, C. Boyer, R. Chapman, *Angew. Chemie - Int. Ed.* **2018**, *57*, 1557–1562.

[76] C. Ma, X. Liu, G. Wu, P. Zhou, Y. Zhou, L. Wang, X. Huang, *ACS Macro Lett.* **2017**, *6*, 689–694.

[77] M. Kovaliov, M. L. Allegrezza, B. Richter, D. Konkolewicz, S. Averick, *Polymer (Guildf).* **2018**, *137*, 338–345.

[78] B. S. Tucker, M. L. Coughlin, C. A. Figg, B. S. Sumerlin, *ACS Macro Lett.* **2017**, *6*, 452–457.

[79] J. Niu, D. J. Lunn, A. Pusuluri, J. I. Yoo, M. A. O'Malley, S. Mitragotri, H. T. Soh, C. J. Hawker, *Nat. Chem.* **2017**, *9*, 537–545.

[80] K. Jung, N. Corrigan, M. Ciftci, J. Xu, S. E. Seo, C. J. Hawker, C. Boyer, *Adv. Mater.* **2020**, *32*, 1–21.

[81] N. Corrigan, C. Boyer, *Trends Chem.* **2020**, *2*, 689–706.

[82] A. Bagheri, C. W. A. Bainbridge, K. E. Engel, G. G. Qiao, J. Xu, C. Boyer, J. Jin, *ACS Appl. Polym. Mater.* **2020**, *2*, 782–790.

[83] F. Momeni, S. M.Mehdi Hassani.N, X. Liu, J. Ni, *Mater. Des.* **2017**, *122*, 42–79.

[84] J. Choi, O. C. Kwon, W. Jo, H. J. Lee, M. W. Moon, *3D Print. Addit. Manuf.* **2015**, *2*, 159–167.

[85] Z. Zhang, N. Corrigan, A. Bagheri, J. Jin, C. Boyer, *Angew. Chemie - Int. Ed.* **2019**, *58*, 17954–17963.

[86] C. W. A. Bainbridge, K. E. Engel, J. Jin, *Polym. Chem.* **2020**, *11*, 4084–4093.

[87] K. V. Khopade, S. H. Chikkali, N. Barsu, *Cell Reports Phys. Sci.* **2023**, *4*, 101341.

[88] **N.d.**

[89] Y. Miao, A. von Jouanne, A. Yokochi, *Polymers (Basel).* **2021**, *13*, 1–17.

[90] J. F. W. Kaminsky, *J. Anal. Appl. Pyrolysis* **1991**, *19*, 311–318.

[91] Q. Dong, A. D. Lele, X. Zhao, S. Li, S. Cheng, Y. Wang, M. Cui, M. Guo, A. H. Brozena, Y. Lin, T. Li, L. Xu, A. Qi, I. G. Kevrekidis, J. Mei, X. Pan, D. Liu, Y. Ju, L. Hu, *Nature* **2023**, *616*, 488–494.

[92] G. K. Hughes, F. N. Lahey, *Nature* **1948**, 705–707.

[93] G. R. Jones, H. S. Wang, K. Parkatzidis, R. Whitfield, N. P. Truong, A. Anastasaki, *J. Am. Chem. Soc.* **2023**, *145*, 9898–9915.

[94] M. R. Martinez, S. Dadashi-Silab, F. Lorandi, Y. Zhao, K. Matyjaszewski, *Macromolecules* **2021**, *54*, 5526–5538.

[95] M. J. Flanders, W. M. Gramlich, *Polym. Chem.* **2018**, *9*, 2328–2335.

[96] V. Raus, E. Čadová, L. Starovoytova, M. Janata, *Macromolecules* **2014**, *47*,

7311–7320.

[97] Y. Sano, T. Konishi, M. Sawamoto, M. Ouchi, *Eur. Polym. J.* **2019**, *120*, 109181.

[98] M. R. Martinez, F. De Luca Bossa, M. Olszewski, K. Matyjaszewski, *Macromolecules* **2022**, *55*, 78–87.

[99] H. S. Wang, N. P. Truong, Z. Pei, M. L. Coote, A. Anastasaki, *J. Am. Chem. Soc.* **2022**, *144*, 4678–4684.

[100] H. S. Wang, N. P. Truong, G. R. Jones, A. Anastasaki, *ACS Macro Lett.* **2022**, 1212–1216.

[101] Joke Vandenbergh and Tanja Junkers, *Macromolecules* **2013**, *46*, 3324−3331.

[102] S. T. and T. F. Yuki Kitahara, Ko Okuyama, Keita Ozawa, Takuya Suga, *J. Therm. Anal. Calorim.* **2012**, *110*, 423–429.

[103] V. P. Balema, I. Z. Hlova, S. L. Carnahan, M. Seyedi, O. Dolotko, A. J. Rossini, I. Luzinov, *New J. Chem.* **2021**, *45*, 2935–2938.

[104] H. Hocker, *J. Macromol. Sci. Part A* **1993**, *30*, 595–601.

[105] X. Jia, C. Qin, T. Friedberger, Z. Guan, Z. Huang, *Sci. Adv.* **2016**, *2*, 1–8.

Chapter 3

UV to visible light TiO_2-catalyzed PET-RAFT polymerization

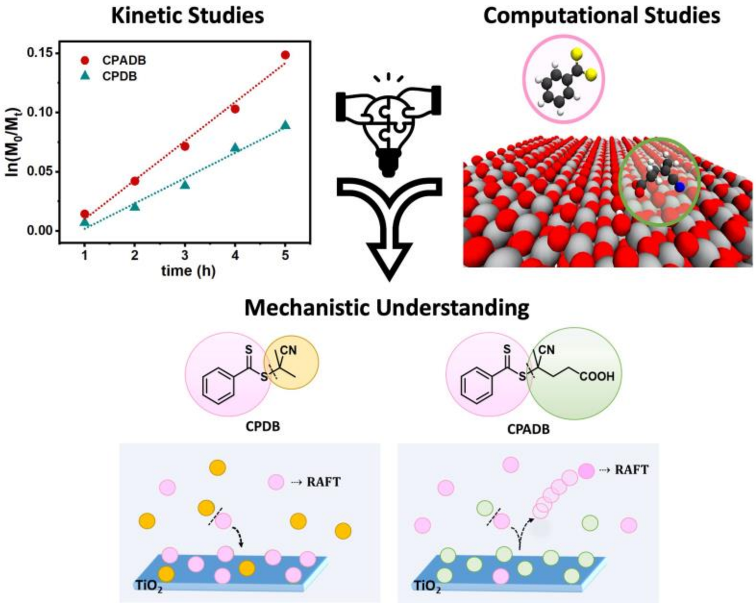

Part of this chapter has been published as:

"V. Bellotti, C. Daldossi, D.e Perilli, M. D'Arienzo, M. Stredansky, C. Di Valentin, R. Simonutti, *UV to visible light PET-RAFT polymerization catalyzed by titanium dioxide-based nanoparticles*, Journal of Catalysis, 428, (**2023**), 115074."

3.1 Introduction

Heterogeneous catalysis is an essential aspect for actual industrialization of chemical processes. The combination of photocatalysis and polymer chemistry culminating in the photoinduced energy/electron transfer (PET-RAFT) process have exploited a wide variety of photocatalysts but the vast majority of them are used in homogenous conditions (transition metal complexes[1,2] naturally derived photoactive compounds,[3–5] and organic dyes[6,7]). Few examples of heterogeneous catalysts are reported, *i.e.* perovskite nanocrystals,[8] and quantum dots[9,10] which are mostly toxic or not synthesizable on a large scale. Other solutions have been found to shift toward heterogeneous catalyst by anchoring organic catalysts onto macroscopic surface such as cellulose matrix.[11]

On this topic, titanium dioxide (TiO_2) is a highly stable, non-toxic, and inexpensive semiconducting metal oxide known for its exceptional photocatalytic properties. Its photoactivity was discovered back in the 1930s,[12] leading it to become one of the most widely used heterogeneous photocatalysts. Its applications range from environmental purposes like removing pollutants and biological contaminants[13] to more advanced technologies like solar cells[14] and water splitting.[15] However, one major limitation of TiO_2 photocatalyst is its large bandgap, with values of approximately 3.20 eV for the bulk anatase phase and 3.02 eV for the rutile phase. This means that their photocatalytic activity is primarily triggered by exposure to ultraviolet (UV) light. When photons with energy equal to or higher than the TiO_2 bandgap (E_g) are absorbed, electron-hole pairs are generated in the conduction band (CB) and valence band (VB). Unfortunately, around 90% of these photogenerated electron-hole pairs rapidly recombine, following both radiative and nonradiative pathways, reducing the overall efficiency.[16–18] The poor light absorption and charge separation under visible light irradiation have restricted TiO_2 application in fields that rely on solar energy as a renewable resource. Consequently, significant efforts have been devoted to enhancing TiO_2 light absorption in the visible spectrum. Common strategies include band gap engineering through the introduction of impurities[19–22] or surface functionalization using molecules like organic dyes sensitive to visible light.[23,24] Among these approaches, nitrogen-doped TiO_2 (N-doped TiO_2) has emerged as a promising method to achieve photocatalytic activity under visible light irradiation.[25–30]

You et. al. conducted an investigation on the potential application of TiO_2 as a photocatalyst for PET-RAFT polymerization.[31] In this study, the authors utilized Evonik P25 titanium dioxide nanoparticles (NPs) to synthesize Poly(methyl methacrylate) (PMMA) in a controlled manner under UV irradiation. Initially, the reaction was well-controlled, but after 4 hours, control was lost, and the monomer conversion remained low. The polymerization was performed using 4-cyanopentanoic acid dithiobenzoate (CPADB) as the chain transfer agent due to its redox potential being higher than that of TiO_2. This favorable difference in redox potentials allows the CTA to be reduced through the PET process, thereby initiating the polymerization. Based on the redox potential an electron transfer pathway was proposed for this process,[31] but as of now, no experimental evidence of the mechanism has been provided.

The RAFT polymerization mechanism is well-established; however, when electromagnetic irradiation is used to activate the chain transfer agent, the reaction mechanism becomes less clear. In this scenario, the CTA serves both as the chain transfer agent, as in the RAFT protocol, and as the initiating species. When exposed to light irradiation, the CTA can be directly excited, leading to homolytic fragmentation, followed by the initiation of radical reactions. This light-induced homolysis process is known as the photoiniferter (PI) mechanism.[32] It occurs when the electromagnetic irradiation provides enough energy to break the C-S bond, often leading to irreversible photolysis and degradation of the CTA.[33–35] To address this challenge, the introduction of a photoredox catalyst, as in PET-RAFT, enables the use of the entire ultraviolet, visible, and infrared spectrum, depending on the nature of the PC. In such cases, it has been proposed that the crucial step for generating the initiating radical species involves a photoinduced electron or energy transfer from the excited state photoredox catalyst to the CTA.[36,37] This process allows the CTA to directly initiate the polymerization reaction.

Despite the potential advantages of TiO_2, such as its cost-effectiveness, non-toxicity, recyclability, and ease of manipulation, its use in polymerization remains limited. In the present Chapter, our main objective is to present a comprehensive study of the photocatalytic mechanism involved in PET-RAFT polymerization using both commercial P25 TiO_2 and synthesized N-TiO_2 nanoparticles. For this study, we have selected two dithiobenzoates: 4-cyanopentanoic acid dithiobenzoate (CPADB) and 2-cyanoisopropyl dithiobenzoate (CPDB), which are commonly used as chain transfer agents for the polymerization of methacrylates and methacrylamides. In addition, these CTAs have been reported to offer good control over molecular weight, dispersity, and end-group fidelity in traditional RAFT.[38,39] To gain insights into the PET-RAFT initiation process we have combined experimental data with first-principles calculations based on hybrid density functional theory (DFT) methods. This approach allows us to determine the key steps leading to the PET-RAFT process and rationalize the factors contributing to the polymerization. Moreover, using the knowledge gained from our study, we have optimized the experimental synthesis setup by increasing the surface area of TiO_2 nanoparticles and introducing nitrogen dopants (N-TiO_2). By doing so, N-TiO_2 nanoparticles can harvest lower energy light (460 nm) in the visible range, leading to better control and an enhanced degree of livingness in the polymerization process. In conclusion, our study not only demonstrates the promising application of titania in PET-RAFT polymerization but also provides specific guidelines for better designing and optimizing the procedure.

3.2 Materials and Methods

3.2.1 Materials

Dichloromethane (DCM), methanol (MeOH), N,N’-dimethylformamide (DMF), tetrahydrofuran (THF), deuterated chloroform ($CDCl_3$) were purchased from Sigma Aldrich and used as received. Methyl methacrylate (MMA) was purchased from Sigma and purified in basic alumina column before use to remove the inhibitor. 4-dimethylaminopyridine (DMAP) and 2-cyanoisopropyl dithiobenzoate (CPDB) was purchased from Sigma Aldrich whereas 4-cyanopentanoic acid dithiobenzoate (CPADB) was synthetized as reported in literature[40,41] starting from 4,4'-azobis(4-cyanopentanoic acid) and bis(thiobenzoyl) disulfide, both purchased by Sigma Aldrich. Degussa P25 titanium dioxide (TiO_2) powder (78% anatase, 14% rutile and the remaining 8% amorphous phase) with a primary particle diameter of 30 nm and BET surface area of 50 m^2/g, was purchased by

Evonik TiO_2. N-TiO_2 was synthesized according to literature[42] starting from titanium butoxide, $Ti(OBu)_4$, and diethanolamine (DEA) purchased by Sigma Aldrich. The LED UV light source used was UV Z5 High Power series (CUN66A1G) with a peak wavelength $\lambda = 367 \pm 3$ nm and a radiant flux $\Phi e = 1.85$ W assembled on a heat sink. Blue LED light ($\lambda = 460$ nm) was purchased in strips and accommodated in circular shape in a home-made photoreactor with a light intensity of 10 mW/cm^2.

3.2.2 Experimental procedures

Synthesis of CPADB chain transfer agent

Synthesis of 4-cyanopentanoic acid dithiobenzoate (CPADB) was performed according to literature.[44,45] 4,4'-azobis(4-cyanopentanoic acid) (2.94 g, 10.5 mmol) and bis(thiobenzoyl) disulfide (DTBA) (2.15 g, 7 mmol) were dissolved in distilled ethyl acetate (40 mL) and heated at reflux for 18 hours. After the removal of solvent in vacuum the crude product was isolated by column chromatography using ethyl acetate:n-hexane 2:3 as eluent. The red fraction was collected and dried out under vacuum to afford 4-cyano-4-((thiobenzoyl)sulfanyl)pentanoic as a red oil. This latter product was placed in the freezer at -20 °C to crystallize. The compound was recrystallized from ethyl acetate:n-hexane 2:3 and analyzed through NMR and FT-IR spectroscopy; yield 50.1%.

Grafting of CPADB on TiO_2 surface

TiO_2 (1 g) and CPADB (50, 34 and 10 wt/wt) were added to a 50 mL two neck round-bottom flask thermal pretreated. The system was left under vacuum for 2 hours in order to remove any trace of water and was suspended, under anhydrous conditions, in anhydrous DMF (0.1 g/mL in all cases). The suspension was sonicated for 20 minutes and kept for 96 hours in the dark under stirring at room temperature in an inert nitrogen atmosphere. The grafted TiO_2 particles (TiO_2@CPADB) were recovered by centrifugation (30 min at 6000 rpm), removing the supernatant which contained the residual unreacted CTA. The powder was washed twice for 30 minutes with ethyl acetate and twice with CH_2Cl_2. The result powder was dry under vacuum overnight to remove the residual solvent. DLS, IR, TGA and elementary analysis were performed to analyze the degree of functionalization.

General procedure for the kinetic studies of PET-RAFT polymerization of MMA with CPDB and CPADB chain transfer agents

A stock dispersion of TiO_2 (Degussa P25) in DMF was prepared with a concentration of photocatalyst equal to 0.32 mg/mL, before each polymerization the stock dispersion was sonicated for 30 min in order to finely disperse the nanoparticles. Two different chain transfer agents were tested: CPADB and CPDB. In the first case MMA (5.75 g, 57.48 mmol) and CPADB (53.5 mg, 0.19 mmol), with a ratio of [MMA]:[CPADB]=300:1 was added to a 50 mL Schlenk tube together with 2.5 mL of TiO_2 dispersion [MMA]=6.67 M. In the second MMA (14.39 g, 143.7 mmol) and CPDB (106.0 mg, 0.48 mmol), with a ratio of [MMA]:[CPDB]=300:1 was added to a 50 mL Schlenk tube together with 5 mL of TiO_2 dispersion [MMA]=7.08 M. For the experiment with the addition of DMAP as sacrificial electron donor a ratio of [CTA]:[DMAP] = [1]:[5] was used. After four freeze-thaw-pump cycles the tube was filled with nitrogen, closed in a dark box with reflecting walls and irradiated under UV LED light. The instant in which the light source is turned on is considered the polymerization initial time (t_0). Polymerization reactions were quenched in an ice bath at selected times. The TiO_2 nanoparticles were recovered by centrifugation (15 min at 6000 rpm) and the supernatant was precipitated in a large excess of cold methanol. NMR was used for determinate M_n and conversion, GPC with St standard displayed the Mn and dispersity. The titanium dioxide powder was washed three times and the residual solvent evaporated under vacuum overnight for TGA analysis.

Increasing titanium dioxide concentrations and surface area

Different concentrations of TiO_2 were employed and the monomer to solvent ratio was varied to obtain various degrees of agglomeration, and consequently different active surface area of the photocatalyst. A stock dispersion of Degussa P25 TiO_2 in DMF was prepared with a concentration of photocatalyst equal to 5 mg/mL and sonicated for 30 minutes. Selected volumes of the dispersion were withdrawn and added to the MMA/DMF mixture with a DMF volume fraction respect to the monomer of 0.23 for the 0.15 mg/mL final TiO_2 concentration experiment, 0.11 for 0.168 mg/mL, 0.07 for 0.174 mg/mL and 0.71 for 0.32, 0.48, 1.28, 1.92, 3.20 mg/mL. All the reaction mixtures were analyzed by DLS to obtain the hydrodynamic volume of the photocatalyst aggregates in solution and then the CTA added to the mixture. The polymerization procedure is the same as described above. The ratio [MMA]:[CPDB] was maintained constant to 300:1 and all the reactions stopped after 4 hours.

Synthesis & Characterization of of N-doped TiO_2

N-doped TiO_2 was prepared by a modified literature procedure.[43] $Ti(OBu)_4$ (2.17 mg, 0.063 mmol) was added to a mixture of 8.75 mL of EtOH and diethanolamine (DEA) (1.31 g, 0.0125 mol) and stirred at room temperature. After 2 hours, the solution was hydrolyzed by the addition of

230 μL of water and stirred for another 2 h. The final product was precipitated in acetone, recovered by centrifugation (10 min at 6000 rpm) and dried overnight. Finally, the powder was calcined in air at 550 °C for 1 h.

The crystal phases of the final product were characterized by powder X-ray diffraction, Raman spectrometer and TEM. Diffuse reflectance spectroscopy was performed using a UV/vis/NIR spectrophotometer. The reflectance was transformed by the Kubelka-Munk (K-M or F(R)) method which is based on the following equation:

$$F(R) = \frac{(1-R)^2}{2R} \approx a \qquad (3.1)$$

where R is the reflectance and F(R) is proportional to the extinction coefficient (α). The determination of the optical energy gap (E_g) is possible by plotting the $(F(R) \times E)^{1/2}$ versus E and fitting the linear portion of the curve by a straight line. The x-axis intersection, calculated by dividing the intercept by the slope, provides the value for E_g.[44] Using this methodology, a shift of 0.3 eV, i.e. from 3.1 eV to 2.8 eV (438 nm) was determined. Finally, the presence of nitrogen into the synthetized N-TiO_2 structure was investigated using Electron Paramagnetic Resonance (EPR) and X-Ray Photoelectron Spectroscopy (XPS).

PET-RAFT polymerization of MMA with CPDB and CPADB chain transfer agent using Doped titanium dioxide

3.08 mg of N-TiO_2 previously synthetized were dispersed in 4.59 mL of DMF and sonicated for 30 minutes. MMA (1.73 g, 17.24 mmol), CPADB (16.05 mg, 0.057 mmol) or CPDB (12.72 mg, 0.057 mmol) were added to the dispersion. The final concentration of N-doped titanium dioxide was 0.48 mg/mL. After four freeze-thaw-pump cycles the tube was filled with nitrogen and closed in a dark box with reflecting walls and irradiated under blue LED light. Polymerization reactions were quenched in ice baths and stored in the dark. The TiO_2 nanoparticles were recovered by centrifugation (15 min at 6000 rpm) and the supernatant was precipitated in a large excess of cold methanol. NMR was used for determinate Mn and conversion, GPC with St standard displayed the M_n and dispersity.

3.2.3 Computational Methods

Considering the size of the Degussa P25 nanoparticles used experimentally, we chose to model the TiO_2 surface using a periodic slab model. In fact, the effect of the curvature of the surface can be considered negligible when the radius of the nanoparticles is sufficiently large, as it is in our experimental setup (Z-average diameter of 263 (±0.34) nm from the DLS analysis) Degussa P25 nanoparticles contain both anatase and rutile TiO_2 phases in a ratio of about 3:1, and anatase is usually considered to be more suitable for photocatalytic applications with respect to rutile because of its indirect band gap of 3.20 eV, which is higher than for rutile (3.02 eV), making the recombination of photogenerated charge carriers slower. For these reasons, we chose to model an anatase surface and, specifically, the anatase (101) TiO_2 surface since it is known to be the most stable and the most widely exposed.

All DFT calculations were performed with the CRYSTAL17[45] package where the Kohn-Sham orbitals are expanded in Gaussian type orbitals. The all-electron basis sets are Ti 86-411(d41) and O 8-411(d1) for the atoms of TiO_2; H 511(p1), C 6-311(d11), N 7-311(d1), O 8-411(d11) and S 86-3111(d11) for the atoms of the CTAs. The B3LYP hybrid functional,[46] corrected with the Grimme's approach (B3LYP-D*)[47,48] to include dispersion forces, has been used throughout this work in order to correctly describe the electronic structure of anatase TiO_2.

The anatase (101) TiO_2 surface was modelled using a periodic slab of 4×2 supercell (a = 15.1575 Å, b = 11.1457 Å) with three triatomic layers for a total of 144 atoms. The periodicity was considered along the [101] and [010] directions while no periodic boundary conditions were imposed in the direction perpendicular to the surface. The supercell model is useful to control the coverage of the surface. For this study, the obtained coverage is 0.006 molecule/$Å^2$. The calculations were performed sampling the Γ point only in the first Brillouin zone. The lowest lying row of Ti and O atoms of the bottom layer were kept fixed at the optimized bulk positions during the geometry optimization.

Cutoff limits in the evaluation of Coulomb and exchange series/sums appearing in the SCF equation were set to 10^{-7} for Coulomb overlap tolerance, 10^{-7} for Coulomb penetration tolerance, 10^{-7} for exchange overlap tolerance, 10^{-7} for exchange pseudo-overlap in the direct space, and 10^{-14} for exchange pseudo-overlap in the reciprocal space. The condition for the SCF convergence was set to 10^{-6} hartree on the total energy difference between two subsequent cycles. Convergence in the geometry optimization process is tested on the root-mean-square (RMS) and the absolute value of the largest component of both the gradients and nuclear displacements. The default thresholds for geometry optimization within the CRYSTAL code have been used for all atoms: maximum and RMS forces have been set to 4.50×10^{-4} and 3.0×10^{-4} a.u., and maximum and RMS atomic displacements to 1.80×10^{-3} and 1.20×10^{-3} a.u., respectively.

The density of states (DOS) and projected density of states (PDOS) were computed using a 30×30×1 k-point mesh, setting the zero energy to the vacuum level.

3.3 Results and Discussion

Inspired by the preliminary work of You *et. al.*[31] kinetic studies of PMMA polymerization were conducted using both CPDB and CPADB, as chain transfer agents, and the results are reported in *section 3.3.1*. Subsequently, computational studies were performed in order to obtain a deeper understanding of the experimental behavior and determine which one of the three possible mechanisms, shown in **Scheme 3.2**, is the more plausible for this system.

In *section 3.3.2* the results of hybrid DFT calculations (B3LYP-D*) are presented. In particular, we report the adsorption configurations along with their structural and electronic properties. The results were experimentally supported by the use of electron donating amines as sacrificial electron donor in *section 3.3.3.* In *section 3.3.4* the CTA fragmentation, after the PET process was computationally analyzed, and in particular, the adsorption of the two fragments of the TiO_2 surface revealed competitive interactions, which differs depending on the CTA used. In order to support and understand the role of these interactions on the polymerization the effect of catalyst agglomeration state (which imply different surface areas) on the polymerization has been studied in *section 3.3.5*. Finally, in *section 3.3.6* the attention was focused on the development of N-doped titanium dioxide nanoparticles with shifted absorption in order to allow the polymerization to occur under visible light.

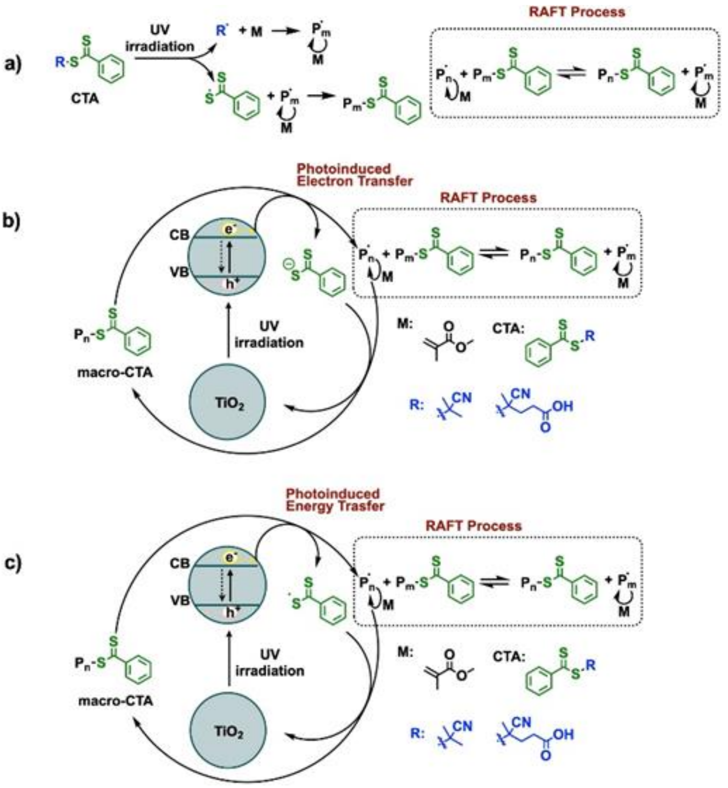

Scheme 3.1: Possible mechanisms of radical species generation: light-mediated pathway by **a)** photoiniferter process, or photocatalyst-mediated pathway by **b)** electron transfer mechanism or **c)** energy transfer mechanism.

3.3.1 Kinetic studies with different CTAs

PET-RAFT polymerization of methyl methacrylate was performed using Degussa P25 as a photocatalyst under UV irradiation (λ=356 nm) at room temperature. Dimethylformamide (DMF) is a polar aprotic solvent with good polarity, and has been selected as polymerization medium due to its capability to stabilize charge-separated species, thus facilitating the initiation of the reaction. Furthermore, the hydroxyl functionalities which cover the TiO_2 surface in a polar environment allows better dispersibility.[49,50] In fact, DLS analysis of the photocatalyst in the solvent results in a Z-average diameter of 263 (±0.34) nm. Herein, both CPDB and CPADB have been used as chain transfer agents for PET-RAFT polymerization of MMA and the kinetics of the process were analyzed (**Figure 3.1**). Monomer conversion was calculated by NMR (**Figure 3.2**).

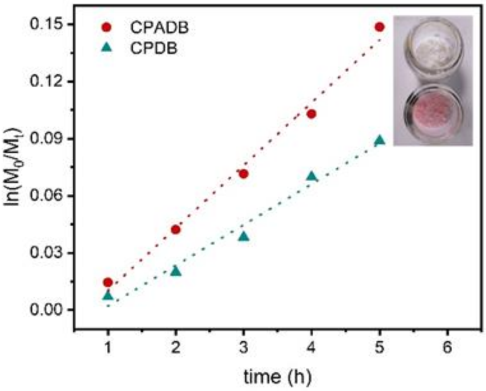

Figure 3.1: Kinetic comparison of PMMA PET-RAFT polymerization using CPADB (red dot) and CPDB (green triangle) as CTAs under UV light irradiation with TiO_2 photocatalyst. Result refers to polymer content in solution (supernatant). The picture shows the final color of the resulting purified polymers after a reaction time of 5 hours.

The faster polymerization rate of the reaction with CPADB with respect to CPDB as chain transfer agent can be attributed to the presence of the -COOH terminal group (R fragment) which allows an additional interaction with the photocatalyst surface. This short distance interaction leads to proximity of the CTA to the photocatalyst surface, which should facilitate the PET process, and consequently the reaction rate. The closeness of CPADB with the surface does not only influence the polymerization rate but also the livingness of the final chains. In particular, in the case of CPADB the red dispersion turned into white, suggesting degradation of the CTA chain-termini. In fact, the dispersity of PMMA obtained with CPADB increased significantly during the reaction reaching Đ = 1.9 after 5 hours. In contrast, when CPDB is used, higher control of the polymerization is obtained, with Đ = 1.32 (**Table 3.1**). UV light alone has been proposed to cause photolysis of dithiobenzoate CTAs, leading to a partial dithioester degradation after long irradiation time.[35] This effect is plausibly increased for CPADB due to the higher rate of electron transfer.

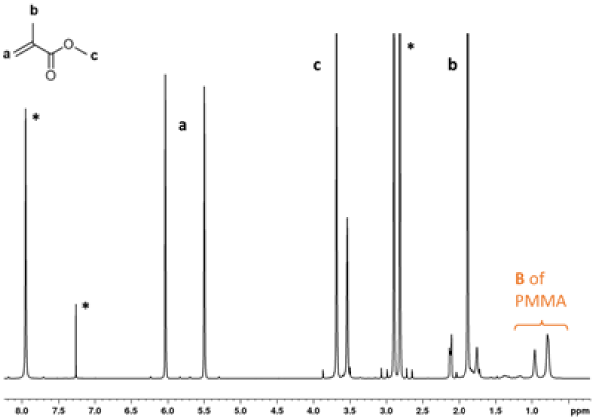

Figure 3.2: ^1H NMR spectrum of representative crude of the reaction in $CDCl_3$. (*) at 2.88, 2.96 and 8.02 ppm represent DMF impurities whereas (*) at 7.26 ppm is $CHCl_3$.

Table 3.1: PET-RFAT polymerization of MMA using CPDB and CPADB chain transfer agent. [a] Conversion has been calculated by NMR. [b] Dispersity obtained by GPC measurements.

Entry	**Time (h)**	**CTA**	**PC**	**light**	**α(%)** [a]	**M_n (g/mol)**	**$M_{n,theo}$ (g/mol)**	**Đ** [b]
1	5	CPDB	TiO_2	no	0	--	--	--
2	5	CPADB	TiO_2	no	0	--	--	--
3	5	CPADB	no	yes	46.7	28 000	14 300	2.61
4	4	CPDB	TiO_2	yes	6.75	2249	2230	1.27
5	5	CPDB	TiO_2	yes	8.50	2796	2775	1.32
6	4	CPADB	TiO_2	yes	9.79	3750	3220	1.57
7	5	CPADB	TiO_2	yes	13.81	5100	4425	1.92

As a control experiment polymerization was performed in the absence of CTAs and irradiation with a conversion proximal to zero. On the other hand, rapid polymerization was obtained under UV irradiation without the PC (**Table 3.1**, entry 3) but the final polymer results in but with a very high dispersity (Đ > 2.5) and non-symmetric molecular weight distribution (**Figure 3.3**), typical of non-controlled free radical polymerization. In this last scenario, the high energetic UV irradiation activates the C-S bond though a photoiniferter mechanism (**Scheme 3.2a**), but quickly results in the loss of polymerization control due to the fast UV photolysis of the RAFT agent.[34,51] These control experiments suggests that PET-RAFT polymerization can be achieved only when both light and the photocatalyst are present.

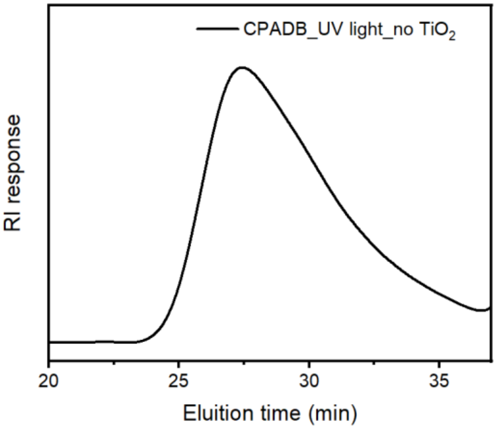

Figure 3.3: GPC traces of PMMA polymerization with CPADB under light irradiation without TiO_2 photocatalyst after 4 hours.

Interaction studies with CPADB

The ability of carboxylic-acid functionality of anchoring onto the TiO_2 surface though Ti-O bond (**Figure 3.3**) is well known[52–54] and widely exploited for the development in many fields, such as for dye sensitized solar cells.

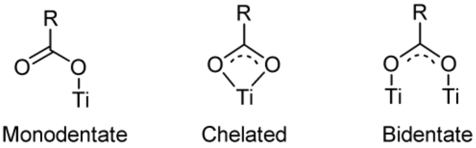

Figure 3.4: Possible coordination modes of deprotonated carboxylic group (COO^-) on TiO_2 surface.

Grafting experiments with CPADB chain transfer agent have been performed to confirm this strong interaction. Suspensions of CPADB and TiO_2 in DMF with different TiO_2/CPADB ratios were stirred at room temperature for 96 hours in the dark. After several washing cycles the powder was dried and characterized by IR, TGA (**Figure 3.5**), and elementary analysis (**Table 3.2**).

Table 3.2: Data of CPADB grafting on TiO_2 (TiO_2@CPADB). [a] Average between TGA and CHNS analysis. [b]Calculated through the following formula: $\Sigma = \frac{\left(\frac{mol\ CPADB}{g\ TiO_2}\right) \cdot N_A [ch/mol]}{A_{sup} TiO_2\ [m^2/g] \cdot 10^{18}\ [nm^2/m^2]}$

Entry	TiO_2/ CPADB (wt/wt%)	[TiO_2] (g/mL)	CPADB Covering NP[a] (wt/wt%)	Σ[b] (molecules/nm^2)	D (nm)
TiO_2@CPADB_50	50	0.1	1.7 ± 0.1	0.78	1.28
TiO_2@CPADB_34	34	0.1	2.1 ± 0.1	0.92	1.17
TiO_2@CPADB_10	10	0.1	2.7 ± 0.4	1.03	1.11

IR spectroscopy confirmed the grafting of the chain transfer agent (TiO_2@CPADB) thanks to the appearance of both asymmetric and symmetric stretching bands of the carboxyl functionality (COO^-), respectively at 1660 and 1437 cm^{-1}, which indicate the bidentate or chelating coordination mode. In addition, the characteristic C=O vibration mode, of non-coordinated aliphatic acids, (1700 cm^{-1}) is absent. The sp^3 aliphatic C-H stretching vibrations at 2967 and 2935 cm^{-1}, confirm the presence of organic material. The sp^2 stretching mode of the aromatic ring is not distinguishable because it is covered by the -OH stretching vibrations of physiosorbed moisture. When grafting experiments were repeated for CPDB, no characteristic vibration mode of the CTA on the surface was detected.

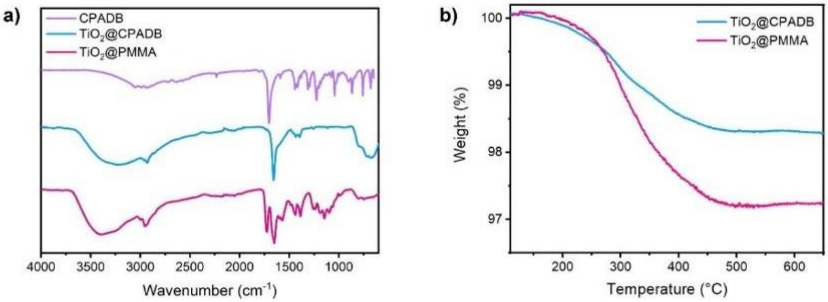

Figure 3.5: a) FT-ATR of Degussa P25 after grafting with CPADB (blue) and at the end of PET-RAFT polymerization (pink) in comparison with the spectrum of CPADB (purple). b) TGA analysis of Degussa P25 after grafting with CPADB (blue), sample TiO2@CPADB_50, and at the end of PET-RAFT polymerization (pink). The net weight loss percentage between 100 and 650° C was assigned to the organic material degradation.

In a similar fashion, grafting of PMMA on the photocatalyst surface occurs during PET-RAFT polymerization under irradiation. In order to prove it, the heterogeneous catalyst was recovered at the end of the polymerization by centrifugation of the crude mixture, and washed several times. Characteristic PMMA signals at 1721 cm^{-1} (C=O), 1147 cm^{-1} (C-O-C) and 1435 cm^{-1} (C-H stretching vibrations of the $-CH_3$ and $-CH_2-$ groups) are present in the FT-ATR spectrum (**Figure 3.5a**), confirming the grafting of the polymeric chains. The amount of grafted polymer was quantitatively assessed by TGA analysis, resulting in 3 wt% (**Figure 3.5b**).

3.3.2 Computational investigation of the PET of initiation

All the three mechanisms described in **Scheme 3.2** have been investigated by means of computational DFT calculation.

CTA activation through photoiniferter mechanism

The photoiniferter (PI) properties of CTAs (**Scheme 3.2a**) are already known and exploited in RAFT polymerization since the pioneering work of Otsu et. al.[55]. In PI polymerization the electromagnetic irradiation directly allows C-S bond fragmentation and the consequent formation of the radical initiator (R·) and the thiocarbonyl radical (ZSS·). This process occurs also during PET-RAFT polymerization, depending on the selected wavelength, but the kinetics of PI is much lower respect to PET-RAFT. The energy required for the homolytic cleavage of this specific bond ($E_{C\text{-}S}$) has been calculated as follows:

$$E_{C-S} = E_R + E_{ZSS} - E_{CTA} \qquad (3.2)$$

Where E_R is the energy of the thiocarbonyl radical, E_{ZSS} is the energy of the thiocarbonyl radical, and E_{CTA} is the energy of the chain transfer agent.

The calculated energy needed to homolytically break the C-S bond for CPDB is 1.62 eV, whereas for CPADB is 1.58 eV meaning that the UV LED source used in the experimental set up (λ_{max} = 365 nm) provide enough energy to fragment the C-S bond. This hypothesis has already been proved correct by the control experiment in the absence of the TiO_2 photocatalyst under UV irradiation. However, if this was the case, the polymerization would proceed by a fast and non-controlled pathway, different from what was observed in the presence of the photocatalyst. For these reasons we can safely exclude photoiniferter as the main reaction mechanism at play in the presence of the PC.

CTA activation through photoinduced electron/energy transfer (PET)

On the other hand, both for electron and energy transfer, excitation of the photocatalyst is firstly needed followed by an interaction of the CTA with the photocatalyst in the excited state (PC*). Once the electron-hole pair is formed the conduction-band electron can be transferred to the CTA occupying one of its first unoccupied orbitals leading to its fragmentation. This would be the case of an electron transfer mechanism (**Scheme 3.2b**). The CTA fragmentation in this occasion would not produce to radicals as in photoiniferter mechanism, instead a radical initiator and a charged thiocarbonyl species would form if the electron is transferred to an empty state of the molecule with a non-bonding orbital distribution. Instead, if the favored pathway would be an energy transfer (**Scheme 3.2c**) the PC* transfer the excitation energy *via* either a Dexter or a Förster mechanism leading to the CTA in the excited state (CTA*). This case the homolytic fragmentation of the thiocarbonylthio molecule into R· and ZSS· fragments.

In order to understand the favored pathway, the adsorption of both CPDB and CPADB on the TiO_2 (101) anatase surface model has been first calculated. In particular, difference between the total energy of the TiO_2/CTA system (E_{tot}) with the energy of the CTA alone (E_{CTA}) and that of the optimized TiO_2 surface slab model (E_{TiO2}) provided the adsorption energy (E_{ads}):

$$E_{ads} = E_{tot} - (E_{CTA} + E_{TiO_2}) \qquad (3.3)$$

Due to the presence of various heteroatomic functionality such as the nitro and/or the sulfur group the CPDB molecule, optimized in the gas phase, can have different adsorption modes: monoS, monoN, and bidentate (**Figure 3.6**). Among them, the most stable is the bidentate configuration, according to the calculated adsorption energies: -0.94 eV, -1.14 eV, and -1.34 eV, respectively. The bidentate (**Figure 3.6c**) is represented by the interaction of the cyano and the thiocarbonyl groups with two undercoordinated (five-fold coordinated) Ti_{5c} of the anatase (101) surface.

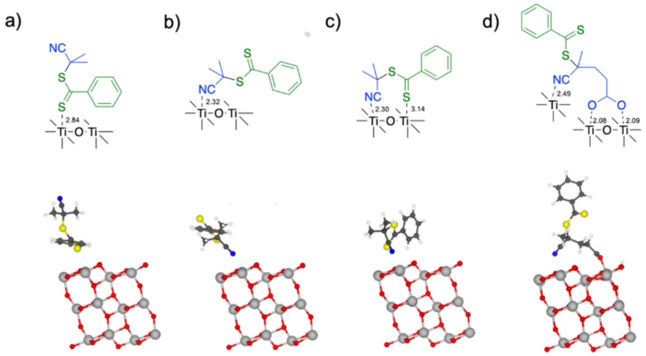

Figure 3.6: Structure of the adsorption on the TiO_2 (101) anatase surface of a,b,c) CPDB (monoS, monoN and bidentate, respectively) and d) CPADB. The length of the bonds between the atoms of the RAFT agent and those of the surface are reported in Å on the structural formula.

The presence of an additional carboxylic group in CPADB chemical structure, with respect to CPDB, changes the favorable binding mode of the latter with the TiO_2 (101) anatase surface. As already mentioned -COOH functionality is known to stably bind to the TiO_2 surface by a dissociated bridging bidentate way,[12] with the two oxygen atoms of the carboxylic group (one of which is deprotonated with the proton migrating to a surface O atom) bonding with two undercoordinated Ti_{5c} atoms. In this configuration the interaction with the thiocarbonyl group is no longer possible, whereas the cyano group and another Ti_{5c} atom of the surface can still interact (**Figure 3.6d**). This strong interaction of the carboxylic group with the surface results in a higher adsorption energy for CPADB (-1.93 eV) with respect to CPDB.

Knowing the most stable adsorption configurations of the two chain transfer agents, we investigated the electronic properties through the total (TDOS) and the projected density of states (PDOS), as shown in **Figure 3.7**. As expected for anatase surface, O 2p contribution composes the majority of states at the top of the valence band, while the bottom of the conduction band states are mainly composed of Ti 3d contribution.

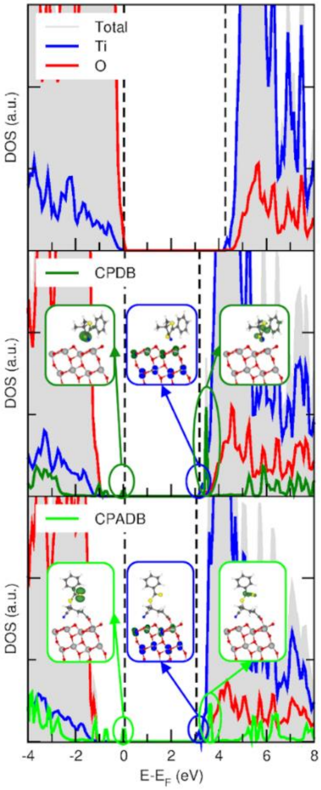

Figure 3.7: TDOS and PDOS of the TiO2 (101) anatase surface pristine (upper panel) and functionalized with CPDB (middle panel) and CPADB (lower panel). On each panel are reported the highest occupied state and the lowest unoccupied state using dashed lines, and the plotted density of the HOMO and LUMO molecular state and the lowest unoccupied state of the material.

Following the presented slab model the calculated band gap of TiO_2 is 4.25 eV. When adsorbed CPDB and CPADB were considered in the PDOS analysis, some occupied molecular levels are present inside the band gap, which correspond to π orbitals localized on one or both the S atoms of the CTAs. The presence of those states reduces the gap between the highest occupied state and the lowest unoccupied state to 3.13 eV and 3.00 eV, respectively. For both CPDB and CPADB, the bottom of the conduction band remains unchanged, while the first molecular empty states are localized inside the conduction band.

Electron transfer mechanism can only occur when an empty molecular state, with a non-bonding orbital distribution on the C-S bond to be broken, is located at the bottom of the conduction band. In this case, the electron of the PC* could populate that non-bonding state leading to CTA fragmentation. In our system, for both the PDOS of CPDB and CPADB adsorbed on the TiO_2 (101) anatase surface no such state is observed. In fact, the non-bonding orbital distribution on the C-S bond is located deep inside the conduction band, and the LUMO of the molecule is not characterized by a distribution of the C-S bond. Based on these observations the possibility of a photoinduced energy transfer initiation of the polymerization can be excluded. On the other hand, the wide band gap of the semiconductor photocatalyst still offers enough energy for the homolytic break of the C-S bond (1.62 eV and 1.58 eV for CPDB and CPADB, respectively), meaning the energy transfer mechanism is still plausible.

3.3.3 Experimental evidences of energy transfer mechanism

By experimental means, the uses of sacrificial electron donors, *i.e.* tertiary amines (R_3N), can validate or exclude the initiation by electron transfer mechanisms. In fact, it has been already shown that PET-RAFT polymerization kinetic can be accelerate in the presence of sacrificial electron donor, such as R_3N, when specific photocatalyst (*i.e.* Eosin Y[56] and cadmium selenide quantum dots[57]) are used. The electron of the tertiary amine is used to neutralize the photogenerated hole and prevents photoexcited electron-hole recombination processes, improving the photocatalyst turnover. The efficiency of this process is translated into an acceleration of the polymerization due to the higher electron lifetime.

There are no evidences in the literature on the effect of sacrificial electron donor for TiO_2 catalyzed PET-RAFT polymerization, thus we studied the polymerization kinetic in our previous conditions but in the presence of 4-dimethylaminopyridine (DMAP). If the mechanism proceeds through an electron transfer as in the case of Eosin Y[56] we would expect to notice an acceleration in the polymerization rate. However, the polymerization proceeded in the same kinetic regime as the same reaction in the absence of DMAP (**Figure 3.8**) making the hypothesis of the CTA fragmentation by energy transfer more and more plausible as already shown by computational calculations.

Finally, it should be noted that for an excited electron to be transferred to the CTAs, close proximity to the surface is essential, while energy transfer can occur up to several Angstrom far from the surface. This becomes relevant for the RAFT reaction in solution, when the polymer chains starts to grow and the ZSS fragment moves away from the surface.

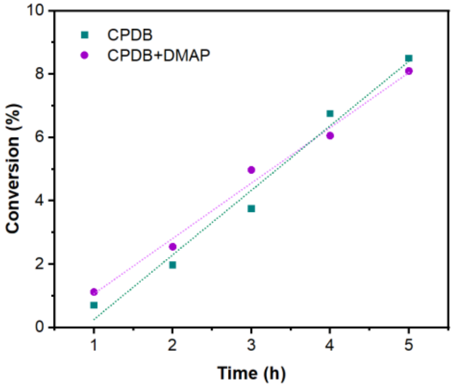

Figure 3.8: Kinetic comparison of PMMA PET-RAFT polymerization using CPDB with (violet dots) and without (green square) DMAP as sacrificial electron donor.

3.3.4 Computational investigation of CTAs′ fragments adsorption

The homolytic CTAs dissociation via energy transfer mechanism produces two radical fragments R· and ZSS·. These two compete for the adsorption on the TiO_2 (101) anatase surface (**Figure 3.9a** and **e**). In a similar fashion to the adsorption energy (E_{ads}) calculated for the two CTAs, the E_{ads} of the two fragments on the TiO_2 (101) anatase surface model has been calculated as the difference between the total energy of the TiO_2/fragment system (E_{tot}) and the energy of the fragment (E_{fragm}) and that of the optimized TiO_2 surface slab model (E_{TiO2}):

$$E_{ads} = E_{tot} - (E_{fragm} + E_{TiO_2}) \qquad (3.4)$$

For CPDB before fragmentation both the R and the ZSS fragments were in contact with the TiO_2 surface through the cyano and thiocarbonyl group (**Figure 3.9b**). The same interactions remains after the homolytic cleaving of the C-S bond, where the R· fragment interact through the CN group and the ZSS· radical through the two S atoms on which the radical is found to be delocalized (**Figure 3.9c** and **d**). The adsorption energies were found to be -1.05 eV and -0.67 eV for the radical initiator and the thiocarbonyl radical, respectively. These E_{ads} values and the preexistent interactions suggest that after fragmentation both the R· and ZSS· species will be adsorbed on the surface of TiO_2.

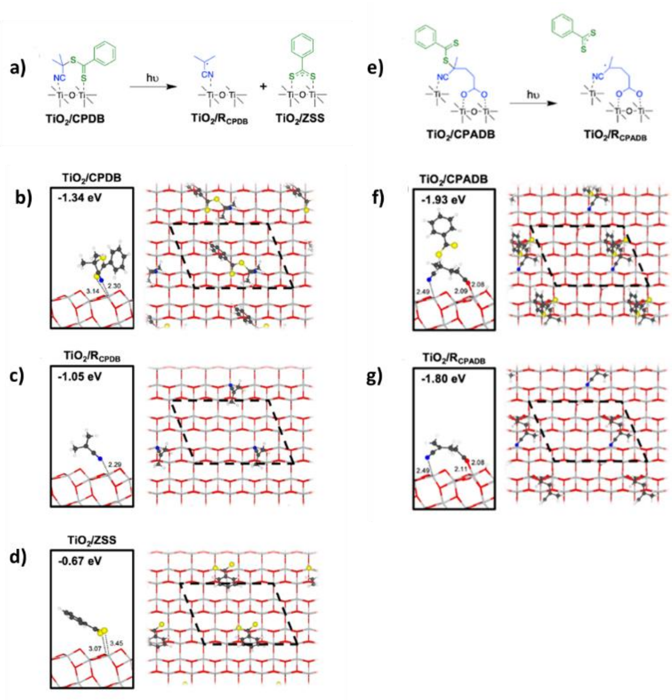

Figure 3.9: Fragmentation of a) CPDB and e) CPADB chain transfer agents on the TiO_2 surface. Schematic representations of the mechanism and adsorption modes (side and top views) on the anatase (101) TiO_2 surface of b) CPDB and f) CPADB; radical initiator generated from c) CPDB and g) CPADB; and d) ZSS radical. Adsorption energies are reported in eV. The overlying parallelogram in dashed line represents the supercell model used for the calculations. Relevant distances are reported in Å in the proximity of the dashed line.

In a different way, the non-dissociated CPADB interacts with the surface only by the R fragment (**Figure 3.9f**). After fragmentation, the R· radical maintains its interaction through both the carboxylic group and the

CN group (**Figure 3.9g**). The dissociated bidentate binding mode of the R· radical through the carboxylic group have a calculated adsorption energy of -1.80 eV, which is much higher than the one calculated for the ZSS· radical (-0.67 eV). The very different E_{ads} values and the fact that the ZSS fragment was not interacting with the surface before PET process occurred lead to the hypothesis that, after fragmentation, only the radical initiator strongly interact with the (101) surface of TiO_2, limiting the access to the ZSS fragment.

The higher probability of the ZSS· radicals, resulting from CPDB fragmentation, to stably interact with the TiO_2 surface can explain the different kinetic trends presented in *section 3.3.1*. In order for the RAFT equilibrium to occur the ZSS fragment should be available in the reaction medium, if the latter is retained by the photocatalyst surface the RAFT equilibrium should be slower, as the case for CPDB. Additionally, this information is pivotal to give a rational basis to the experimental data presented in *section 3.2.3*.

Finally, to give a complete insight of the system in terms of electronic properties, the total (TDOS) and the projected density of states (PDOS) for the thiocarbonyl radical adsorbed on the TiO_2 (101) anatase surface have been calculated. Loss of alignment of the spin α (up) and β (down) components can be observed due to the homolytic cleavage which generates a radical species (doublet spin state), as shown in **Figure 3.10**. Additionally, the plotted PDOS highlight an empty molecular state localized below the conduction band of the TiO_2, which suggest a possible reduction of the ZSS· radical into a charged fragment (ZSS^-) by means of a PC* photoexcited electron. As before, the charged fragment can bind the surface *via* the two sulfur atoms that bind on two different undercoordinated Ti_{5c} atoms.

However, the additional charge provides a stronger interaction with the surface respect to the radical species. In fact, not only the adsorption energy goes from -0.67 eV for the thiocarbonyl radical to -1.51 eV for the ZSS$^-$, but also the geometry configuration exhibits shorter S-Ti bonds (3.07 Å and 3.45 Å for the radical versus 2.66 Å and 2.66 Å for the charged).

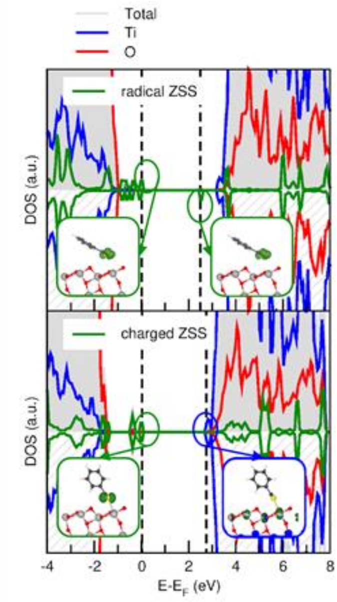

Figure 3.10: TDOS and PDOS of the a) radical and b) charged ZSS adsorbed on the TiO_2 (101) anatase surface with both spin α (up) and β (down) components. On each panel are reported the plotted density of the highest occupied state and the lowest unoccupied state, and their position using dashed lines.

3.3.5 Investigation of photocatalyst surface area

In heterogeneous photocatalysis the reaction occurs at the interface of the photocatalytic material, therefore the catalyst surface plays an important role in the reaction outcomes. In the same fashion we expect that PET-RAFT polymerization is initiated in proximity to the TiO_2 surface and the polymerization outcomes rely on that. In addition, in the previous section we demonstrated that the affinity to the surface of both the both the R· and

ZSS· fragments of the CTAs introduce competitive interactions, which are different depending on the CTA chemical nature. Therefore, not only the photocatalyst surface area is important for the polymerization, but also the available surface area (the surface that is not covered by stable interactions) is pivotal.

In order to investigate this effect PET-RAFT polymerizations were repeated, with both CTAs, varying the surface availability. In heterogeneous catalysis the reactions are carried out in solution, meaning that the catalyst surface area depends on its agglomeration state. For this reason, in order to maintain the same photocatalyst, but achieving different surface area (A_{sup}) values, the monomer to solvent ratio was modified. As already mentioned, Degussa P25 is better stabilized in a polar environment, meaning that when the amount of DMF is higher than the amount of MMA the agglomeration is reduced and high surface area can be achieved. Once the best value of A_{sup} has been found by varying the amount of solvent (i.e. $X_{DMF/MMA} = 0.71$) the surface area can still be increased by increasing the amount of TiO_2. The hydrodynamic volume of the TiO_2 aggregates in the polymerization media (solvent, monomer and CTA) has been measured by DLS analysis, and the overall surface area *per* milliliter has been calculated according to the following formula:

$$\frac{A_{sup}}{mL} = 4\pi R_H^2 * \frac{N_{part}}{mL} \qquad (3.5)$$

Where

$$\frac{N_{part}}{mL} = \frac{[TiO_2]}{\rho_{TiO_2} * \frac{4}{3}\pi R_H^3} \qquad (3.6)$$

In **Table 3.3** are reported the DMF/MMA ratio, and the PC concentration used for each experiment with the respective surface area of Degussa P25. The obtained results are summarized in **Figures 3.11**.

Table 3.3: PET-RAFT polymerization of PMMA at increasing TiO_2 concentration. [a] $\chi_{(DMF/MMA)}$ is the volume fraction of DMF in comparison with MMA. [b] Hydrodynamic radius has been obtained by DLS measurement. [c] Conversion (α) has been calculated by NMR.

				CPDB		**CPADB**	
$[TiO_2]$ (mg/mL)	**$X_{(DMF/MMA)}$ [a]**	**R_H (nm) [b]**	**A_{sup}/mL (m^2/mL)**	**Entry**	**α%[c]**	**Entry**	**α%[c]**
0.15	0.23	1099	9.31E-05	**1**	6.76	**9**	9.27
0.17	0.11	643	1.84E-04	**2**	10.25	**10**	18.38
0.17	0.07	435	2.82E-04	**3**	11.77	**11**	19.68
0.32	0.71	206	1.09E-03	**4**	13.85	**12**	16.03
0.48	0.71	159	2.13E-03	**5**	14.34	**13**	13.18
1.28	0.71	153	5.90E-03	**6**	22.46	**14**	23.55
1.92	0.71	166	8.14E-03	**7**	24.45	**15**	22.05
3.20	0.71	162	1.39E-02	**8**	26.61	**16**	19.02

The experimental results of polymerization using CPDB at increased TiO_2 surface areas are in agreement with an heterogeneous photocatalyzed polymerization. In fact, higher monomer conversion can be reached after 4 hours under irradiation just by increasing the photocatalyst surface area, following an exponential trend. For low surface areas (i.e < 0.003 m^2/mL) a linear relation with the polymerization conversion can be observed (**Table 3.1**, entries 1-4), whereas by increasing the surface values the latter deviate from linearity, until a plateau is reached. Literature studies on Degussa P25 demonstrate that high catalyst loading reduces the photocatalytic performance rather than increase it, due to high turbidity of the dispersion which obstacles the light penetration.[13,58] When the light transmission through the reaction media is low not all the nanoparticles can be photo-excited, thus they do not contribute to the catalytic process.

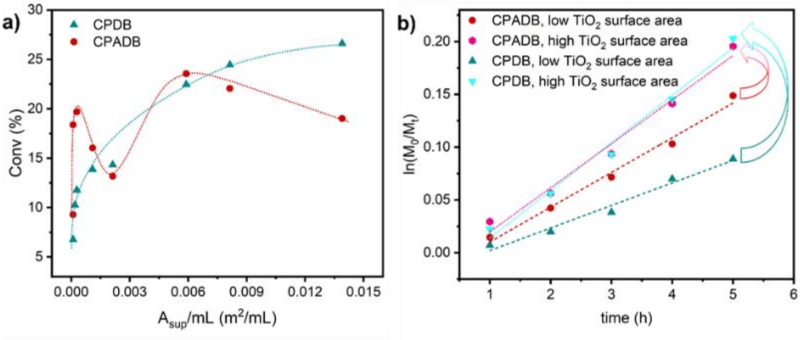

Figure 3.11: a) Monomer conversion versus the calculated surface area of polymerization using CPDB (green) and CPADB (red). Monomer conversion refers to polymer content in solution. b) Kinetic comparison of PMMA PET-RAFT polymerization using CPADB (red and pink) and CPDB (green and blue) as CTAs under UV light irradiation with TiO_2 photocatalyst. Regarding the legend, CPADB low TiO_2 surface area refers to entry 9, CPADB high TiO2 surface area refers to entry 13, CPDB low TiO_2 surface area refers to entry 1, CPDB high TiO_2 surface area refers to entry 5 from **Table 3.1**.

On the other hand, CPADB shows an unexpected trend (**Figure 3.11a,** red dots). In the low surface area range, where a linear trend was expected, the monomer conversion reaches a maximum and then decreases. This behavior can be rationalized by the mechanistic results obtained by the computational study in *section 3.3.4*. In particular, DFT calculation suggested that the faster kinetic of CPADB respect to CPDB can be explained not only by the faster electron transfer due to the higher proximity of the –COOH termini, as hypothesized in *section 3.3.1*, but also by the competitive surface adsorption between the R· and the thiocarbonyl fragments of the dissociated CTA. When low surface area TiO_2 is used the R· fragment of CPADB cover an high portion of the surface and the retention time of the ZSS· fragment by the TiO_2 is negligible, acting immediately as chain deactivator. This competition does not occur for CPDB, where the interaction of the two fragments is comparable. When the surface area of titanium dioxide further increases, also the ratio between CPADB and the available surface sites for interactions (PC/CTA) increases. Now that the availability of the surface area sites is higher, the competitive interactions between the R and the ZSS radicals become less relevant. In these conditions, the kinetics of CPADB and CPDB are comparable (**Table 3.1,** entries 5 and 13). This mechanism is illustrated in **Figure 3.12**.

At even higher surface area values, the conversion increases as expected but instead of reaching the plateau a second drop regime can be observed. This last is due to the fact that conversion is calculated by the polymer produced in the solution, thus it does not consider the chains that remain grafted to the surface. When the recovered photocatalyst has been analyzed by TGA, it has been possible to demonstrate that when the surface area was increased the relative amount of PMMA grafted also increased, explaining the apparent lower conversion in solution.

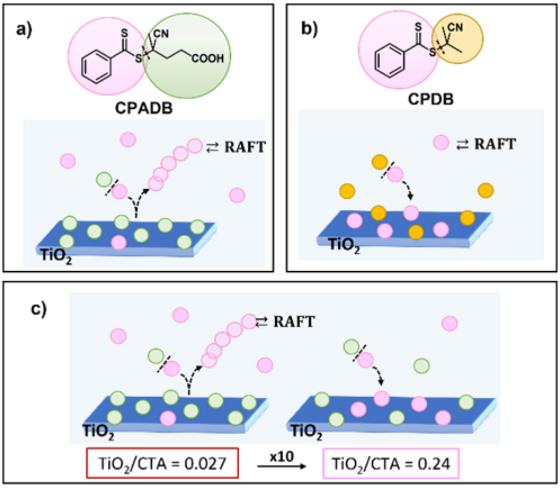

Figure 3.12: Graphical sketch of the interactions of ZSS and R groups of a) CPADB and b) CPDB on TiO_2 surface. Figure c) represents the situation in which CPADB is used as CTA and the available surface area increases, while the amount of CTA decreases. On the left side it is represented entry 9 and on the right entry 13 (see **Table 3.1**).

3.3.6 Going from UV to blue light by N-doping of TiO_2

In the first part of this Chapter, Degussa P25 has been used as photocatalyst for PET-RAFT polymerization due to its low cost, toxicity and wide employment in heterogeneous catalysis for a wide variety of fields, where titanium dioxide can absorb only short-wavelength irradiation due to its wide band gap of 3.20 eV. Unfortunately, in PET-RAFT polymerization the use of high energetic UV light is a disadvantage, due to the photolability of the C-S bond of dithiobenzoate CTAs, which causes loss of control and high dispersity, as demonstrated by the control experiments reported in *section 3.3.1*. In order to solve this problem, the absorption of titanium dioxide was chemically shifted toward the visible spectrum, with the aim to reduce or, possibly, to avoid the CTA degradation.

Synthesis of N-TiO$_2$ photocatalyst

Generally, TiO$_2$ absorption properties can be easily modified through the adsorption of dyes on the surface[23,24] but this procedure would alter the surface properties and saturate available adsorption sites, therefore it has been excluded. Herein, the red shifting of the maximum TiO$_2$ absorption has been obtained introducing nitrogen into the chemical structure of titanium dioxide by an easy sol-gel methodology.[25] XRD and Raman spectroscopy were used to structurally characterize the doped sample and identified the co-existence of anatase and rutile phases (**Figure 3.13c** and **d**). The mean crystallite size determined by TEM is 12.5 nm (**Figure 3.14**). According to several studies the inclusion of photoactive nitrogen in TiO$_2$ structures results in a modification in the sub-band gap region of titania. In fact, the presence of an absorption tail at λ above 400 nm in the UV-vis diffuse reflectance spectrum of N-doped TiO$_2$ powder (**Figure 3.13a** and **b**) confirms the successful shift of the absorption in the visible range.

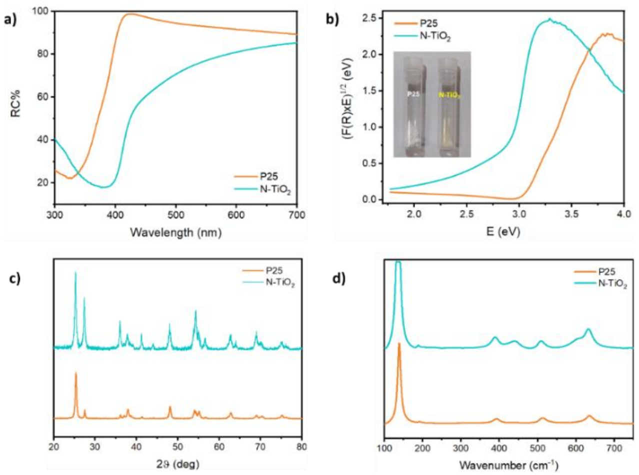

Figure 3.13: a) UV-visible absorption with integrated sphere of the powders in reflectance % and b) Kubelka-Munk transformation, plotting of $(F(R) \times E)^{1/2}$ versus E. c) XRD analysis and d) Raman spectra of N-doped titanium dioxide photocatalyst in comparison whit the commercially available P25 nanoparticles.

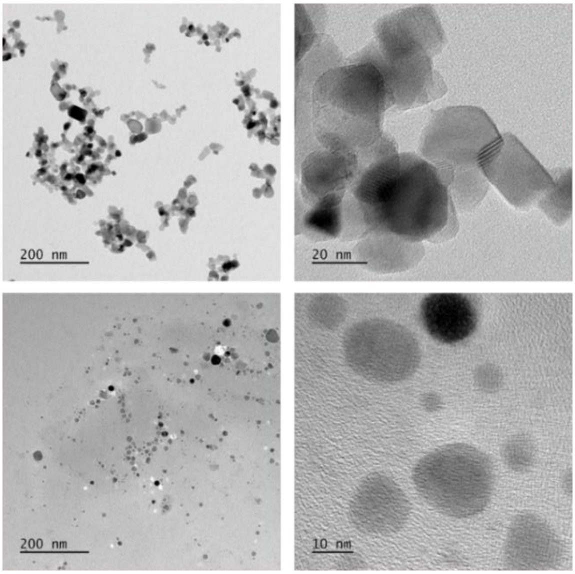

Figure 3.14: a) TEM images of commercially available P25 characterized by particles of a primary diameter of 30 nm which agglomerate in bigger nanoparticles. b) TEM images of N-TiO_2 showing mainly sphere-like morphology without agglomeration.

Additionally, N-based defects in the titanium dioxide lattice were directly detected by X-Band Electron Paramagnetic Resonance (EPR) spectroscopy. The spectrum of N-TiO_2 (**Figure 3.15a**, bottom) presents by an orthorhombic signal with EPR parameters (i.e. *g*-values and hyperfine constants) coherent with those reported in literature[59–62] and was attributed to nitric oxide (NO) species segregated in the lattice imperfection of the TiO_2 structure. By following the saturation behavior as increasing the microwaves power (**Figure 3.15b**), we discovered the presence of a second and weak paramagnetic species, which have been assigned to $NO^{2-\bullet}$ centers, due to the *g*-value and hyperfine coupling matching to those previously assigned.[62]

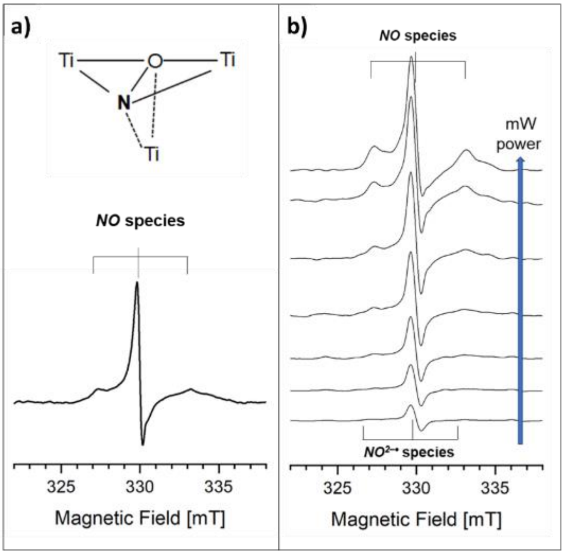

Figure 3.15: a) top, pictorial view of N interstitial center in N-TiO_2; bottom, EPR spectrum at 130 K in vacuo ($p < 10-5$ mbar) of N-TiO_2 nanocrystals. b) Spectra of N-TiO_2 recorded at different mW power at 130 K in vacuo.

Finally, X-ray photoelectron spectroscopy (XPS) was used to finely analyze the surface chemical composition and chemical states of N-doped TiO_2 analyzed (**Figure 3.16**). The analysis uncovered the presence of a single N species detectable at 399.5 eV, which is commonly assigned to NO interstitial sites.[63,64] The surface N/Ti and N/O atomic ratios were also calculated and correspond to ∼0.009. These results prove the positive outcomes of the doping, with the presence of N-interstitial centers (**Figure 3.15a**, top) in the titania structure. It should be noted that not only the nitrogen insertion extends the semiconductor adsorption in the visible region, but it could in principle influence the photocatalytic activity. Up to now there are not concrete evidence whether the effect promote hole-electron pair recombination by the localized band gap states associated with nitrogen doping (inhibiting the electron transfer), or on the contrary favor the charge separation, thus favoring electron transfer mechanisms.[62,65]

Recently, some studies demonstrated that nitrogen can enhance the recombination of the photogenerated charge carriers.[49] Recombination can be seen as a detrimental phenomenon in heterogeneous photocatalysis when electron transfer pathway is wanted, due to the dissipation of the absorbed energy: Anyhow, the energy can be absorbed by molecules with specific electronic features, encouraging energy transfer mechanisms.[66]

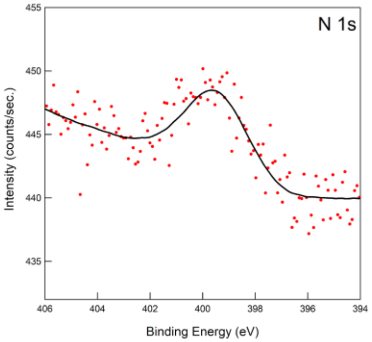

Figure 3.16: N 1s XPS spectrum of N-TiO_2 sample.

PET-RAFT polymerization with the new N-TiO_2 photocatalyst

The produced N-doped TiO_2 nanoparticles were tested for PET-RAFT polymerization of poly(methyl methacrylate) under visible blue LED light ($\lambda_{max} = 460$ nm). CPADB was selected as chain transfer agent due to its poor ability in promoting photoiniferter (PI)-RAFT of MA and MMA, as reported by Quiao et al.[67] and Boyer et al.[68]. In fact, due to their electronic properties thiocarbonate chain transfer agents are preferred over dithiobenzoate for blue light PI-RAFT polymerization.[69] In addition Konkolewicz et al.[70] demonstrated how electron-withdrawing groups decrease the efficiency of photoactivation, making CPADB the best candidate for avoiding competition between PET-RAFT and PI-RAFT in this scenario.

Table 3.4: PET-RAFT polymerization with N-TiO_2 photocatalyst under blue light for 24 hours at room temperature. [a] Monomer conversion calculated with NMR analysis. [b] Theoretical molecular weight ($M_{n,th}$) was calculated according to the formula $M_{n,th} = ([M]_0/[CTA]_0) \times MW^M \times \alpha + MW^{CTA}$, where $[M]_0$, $[CTA]_0$, MW^M, α, and MW^{CTA} correspond to initial monomer and CTA concentration, molar mass of monomer, conversion determined by ^1H NMR, and molar mass of CTA. [c] $M_{n,GPC}$ and dispersity obtained by GPC measures.

Entry	**Time (h)**	**[N-TiO_2] (mg/mL)**	**CTA**	**Conv %[a]**	**$M_{n,th}$ [b]**	**$M_{n,GPC}$ [c]**	**Đ [c]**
17	24	0.48	CPADB	43.3	13 200	13 700	1.17

After 24 hours under blue irradiation not only the monomer reached 43% of conversion (**Table 3.4**) but also good dispersity was obtained (Đ = 1.17) even at long irradiation time (**Figure 3.17b**). The increased livingness of the reaction is easily appreciable by the retention in the reddish color of the final dispersion, which did not change during the polymerization time (**Figure 3.17a**). Moreover, the NMR signals of CPADB benzyl group are appreciable in the aromatic region between 7 and 7.8 ppm (**Figure 3.17c**).

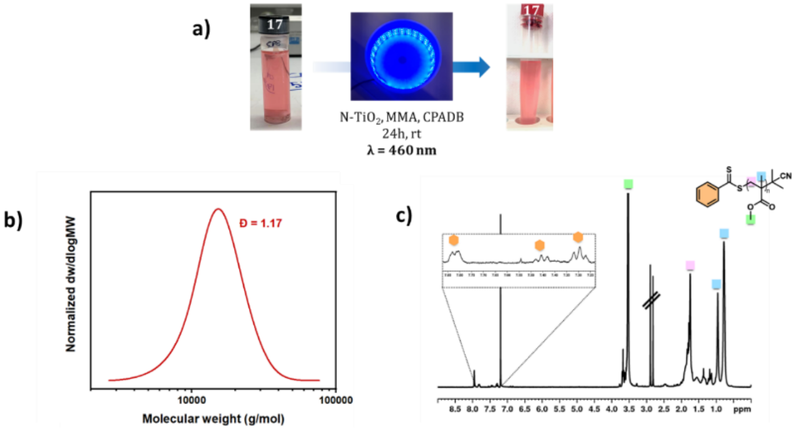

Figure 3.17: a) PET-RAFT polymerization of MMA mediated by N-TiO_2 photocatalyst with CPADB under blue light at room temperature for 24 hours. Good control over the polymerization was obtained with low dispersity and high-end group fidelity as displayed by the b) GPC traces and c) NMR spectrum of the polymer after purification.

According to the computational results which highlight the effectiveness of the two dithiobenzoate chain transfer agents as suitable species for energy transfer and the evidence of nitrogen insertion in the titanium dioxide structure, we speculate that the remarkable performance of N-doped TiO_2 in the polymerization of PMMA may find its origin in an energy-transfer-driven pathway. This is the first report of PET-RAFT polymerization using the titanium dioxide photocatalyst under visible light.

3.4 Conclusions

In conclusion, in the present Chapter the combination of experimental and computational studies has allowed us to unravel the photocatalytic mechanism of PET-RAFT polymerization using TiO_2 as the photocatalyst and CPADB and CPDB as the chain transfer agents.

The computational electronic structure analysis of both CTAs in the presence of model TiO_2 surface, highlight that the energy of the first empty state with the C-S anti-bonding character is too high for the CTAs to be activated by electron transfer. These results, together with experiments in the presence of sacrificial electron donating amins, led us to think that energy transfer is the more plausible pathway for the PC to activate the polymerization.

The interaction between the two chosen chain transfer agents and the titanium dioxide surface was found to be crucial for the outcome of the polymerization process, impacting both reaction kinetics and control. Specifically, computational investigation of the electronic properties of the different species adsorbed on the TiO_2 provided the adsorption energy of both CTAs, resulting in -1.93 eV for CPADB and -1.34 eV for CPDB. The carboxylic moiety of CPADB displayed exceptional anchoring properties, significantly influencing the adsorption mode and enhancing the binding strength to the TiO_2 surface. As a result, CPADB could be readily grafted onto the TiO_2 surface under mild conditions, facilitating its interaction with the photocatalyst. These findings highlight the significance of the CTAs' interaction with the TiO_2 surface and shed light on the mechanisms, providing valuable insights for improving reaction kinetics and control in PET-RAFT polymerization.

The different kinetic behaviors observed for the two CTA have been then justified based on the different competition for the surface interaction of the two fragments (R· and ZSS·) obtained as a consequence of the energy transfer. In fact, we observed that the ZSS· is the same fragment for both CTAs whereas the R· fragment from CPADB interact with the surface more strongly than the one from CPDB (as seen before fragmentation as well). The absorption energy of the R· fragment, after the C-S is homolytically cleaved, is -1.05 eV for CPDB and -1.80 eV for CPADB (almost three times that of the ZSS· -0.67 eV). Therefore, on one hand, the CPDB fragments compete almost equally for the interaction with the surface. On the other, the competition of the CPADB fragments results in the carboxylated R· covering the titanium surface and the ZSS· being less retained, thus more promptly available for the polymerization to occur. When the surface area of the catalyst is increased and the amount of CPADB is kept the same, the coverage of the surface by the R· is no longer the limiting factor and the kinetics of the two CTAs is then comparable.

In conclusion, in order to avoid any CTA degradation during polymerization, the successful N-doping of titanium dioxide has enabled the manipulation of polymerization using lower energy blue light. The less energetic light allows excellent control over the process, even up to 24 hours polymerization. This significant outcome indicates the potential for broader applications of TiO_2 in the controlled polymerization domain. This opens the doors for new studies and further optimization which would allow for efficient heterogeneous PET-RAFT polymerization and possible scale up in the future.

3.5 References

[1] J. Xu, K. Jung, A. Atme, S. Shanmugam, C. Boyer, *J. Am. Chem. Soc.* **2014**, *136*, 5508–5519.

[2] J. Xu, K. Jung, N. A. Corrigan, C. Boyer, *Chem. Sci.* **2014**, *5*, 3568–3575.

[3] S. Shanmugam, J. Xu, C. Boyer, *J. Am. Chem. Soc.* **2015**, *137*, 9174–9185.

[4] S. Shanmugam, J. Xu, C. Boyer, *Angew. Chemie - Int. Ed.* **2016**, *55*, 1036–1040.

[5] S. Shanmugam, J. Xu, C. Boyer, *Chem. Sci.* **2015**, *6*, 1341–1349.

[6] C. A. Figg, J. D. Hickman, G. M. Scheutz, S. Shanmugam, R. N. Carmean, B. S. Tucker, C. Boyer, B. S. Sumerlin, *Macromolecules* **2018**, *51*, 1370–1376.

[7] J. Xu, S. Shanmugam, C. Boyer, *ACS Macro Lett.* **2015**, *4*, 926–932.

[8] Y. Zhu, Y. Liu, K. A. Miller, H. Zhu, E. Egap, *ACS Macro Lett.* **2020**, *9*, 725–730.

[9] Y. Zhu, E. Egap, *Polym. Chem.* **2020**, *11*, 1018–1024.

[10] Y. Liang, H. Ma, W. Zhang, Z. Cui, P. Fu, M. Liu, X. Qiao, X. Pang, *Polym. Chem.* **2020**, *11*, 4961–4967.

[11] Y. Chu, N. Corrigan, C. Wu, C. Boyer, J. Xu, *ACS Sustain. Chem. Eng.* **2018**, *6*, 15245–15253.

[12] G. G. Rao, *Soil Sci.* **1934**, *38*, 143–160.

[13] A. Sebti, H. Lebik, F. Madjene, B. Boutra, *Int. J. Sci. Res. Manag. Stud.* **2018**, *1*, 242–247.

[14] J. Ferber, J. Luther, *J. Phys. Chem. B* **2002**, *105*, 4895–4903.

[15] A. Miyoshi, S. Nishioka, K. Maeda, *Chem. - A Eur. J.* **2018**, *24*, 18204–18219.

[16] J. Schneider, M. Matsuoka, M. Takeuchi, J. Zhang, Y. Horiuchi, M. Anpo, D. W. Bahnemann, *Chem. Rev.* **2014**, *114*, 9919–9986.

[17] K. Nakata, A. Fujishima, *J. Photochem. Photobiol. C Photochem. Rev.* **2012**, *13*, 169–189.

[18] Q. Guo, C. Zhou, Z. Ma, X. Yang, *Adv. Mater.* **2019**, *31*, DOI 10.1002/adma.201901997.

[19] M. H. N. Assadi, D. A. H. Hanaor, *Appl. Surf. Sci.* **2016**, *387*, 682–689.

[20] P. Niu, G. Wu, P. Chen, H. Zheng, Q. Cao, H. Jiang, *Front. Chem.* **2020**, *8*, 1–8.

[21] P. S. Basavarajappa, S. B. Patil, N. Ganganagappa, K. R. Reddy, A. V. Raghu, C. V. Reddy, *Int. J. Hydrogen Energy* **2020**, *45*, 7764–7778.

[22] A. Khlyustova, N. Sirotkin, T. Kusova, A. Kraev, V. Titov, A. Agafonov, *Mater. Adv.* **2020**, *1*, 1193–1201.

[23] W. M. Campbell, A. K. Burrell, D. L. Officer, K. W. Jolley, *Coord. Chem. Rev.* **2004**, *248*, 1363–1379.

[24] A. Andrzejewska, A. Krysztafkiewicz, T. Jesionowski, *Dye. Pigment.* **2004**, *62*, 121–130.

[25] R. Asahi, T. Morikawa, T. Ohwaki, K. Aoki, Y. Taga, *Science (80-.).* **2001**, *293*, 269–271.

[26] H. Irie, Y. Watanabe, K. Hashimoto, *J. Phys. Chem. B* **2003**, *107*, 5483–5486.

[27] J. Wang, D. N. Tafen, J. P. Lewis, Z. Hong, A. Manivannan, M. Zhi, M. Li, N. Wu, *J. Am. Chem. Soc.* **2009**, *131*, 12290–12297.

[28] X. Wang, S. O. Pehkonen, J. Rämö, M. Väänänen, J. G. Highfield, K. Laasonen, *Catal. Sci. Technol.* **2012**, *2*, 784–793.

[29] X. Fang, Z. Zhang, Q. Chen, H. Ji, X. Gao, *J. Solid State Chem.* **2007**, *180*, 1325–1332.

[30] C. Shifu, C. Lei, G. Shen, C. Gengyu, *Chem. Phys. Lett.* **2005**, *413*, 404–409.

[31] B. F. Cheng, L. H. Wang, Y. Z. You, *Macromol. Res.* **2016**, *24*, 811–815.

[32] M. Hartlieb, *Macromol. Rapid Commun.* **2022**, *43*, DOI

10.1002/marc.202100514.

[33] J. F. Quinn, L. Barner, C. Barner-Kowollik, E. Rizzardo, T. P. Davis, *Macromolecules* **2002**, *35*, 7620–7627.

[34] R. N. Carmean, C. A. Figg, G. M. Scheutz, T. Kubo, B. S. Sumerlin, *ACS Macro Lett.* **2017**, *6*, 185–189.

[35] M. D. Thum, S. Wolf, D. E. Falvey, *J. Phys. Chem. A* **2020**, *124*, 4211–4222.

[36] J. Phommalysack-Lovan, Y. Chu, C. Boyer, J. Xu, *Chem. Commun.* **2018**, *54*, 6591–6606.

[37] N. Corrigan, S. Shanmugam, J. Xu, C. Boyer, *Chem. Soc. Rev.* **2016**, *45*, 6165–6212.

[38] D. J. Keddie, G. Moad, E. Rizzardo, S. H. Thang, *Macromolecules* **2012**, *45*, 5321–5342.

[39] S. Perrier, *Macromolecules* **2017**, *50*, 7433–7447.

[40] S. Matsumura, A. R. Hlil, C. Lepiller, J. Gaudet, D. Guay, Z. Shi, S. Holdcroft, A. S. Hay, *J. Polym. Sci. Part A Polym. Chem.* **2008**, *46*, 7207–7224.

[41] S. H. Thang, B. Y. K. Chong, R. T. A. Mayadunne, G. Moad, E. Rizzardo, *Tetrahedron Lett.* **1999**, *40*, 2435–2438.

[42] B. Ohtani, O. O. Prieto-Mahaney, D. Li, R. Abe, *J. Photochem. Photobiol. A Chem.* **2010**, *216*, 179–182.

[43] S. J. Bu, Z. G. Jin, X. X. Liu, L. R. Yang, Z. J. Cheng, *J. Eur. Ceram. Soc.* **2005**, *25*, 673–679.

[44] S. Landi, I. R. Segundo, E. Freitas, M. Vasilevskiy, J. Carneiro, C. J. Tavares, *Solid State Commun.* **2022**, *341*, 1–7.

[45] R. ;Saunders. V. R. ;Roetti. C. ;Orlando. R. ;Zicovic.-W. C. M. ;Pascale. F. ;Civalleri. B. ;Doll. K. ;Harrison. N. M. ;Bush. I. J. ;D’Arco. P. ;Llunell. M. . C. M. . N. Y. . M. L. . E. A. . R. M. . C. S. Dovesi, **2017**.

[46] A. D. Becke, *J. Chem. Phys.* **1993**, *98*, 1372–1377.

[47] S. Grimme, *J. Comput. Chem.* **2006**, *27*, 1787–1799.

[48] B. Civalleri, C. M. Zicovich-Wilson, L. Valenzano, P. Ugliengo, *CrystEngComm* **2008**, *10*, 405–410.

[49] C. Deiana, E. Fois, S. Coluccia, G. Martra, *J. Phys. Chem. C* **2010**, *114*, 21531–21538.

[50] M. Tawfilas, M. Mauri, L. De Trizio, R. Lorenzi, R. Simonutti, *Langmuir* **2018**, *34*, 9460–9469.

[51] J. F. Quinn, E. Rizzardo, L. Barner, C. Barner-Kowollik, T. P. Davis, *Am. Chem. Soc. Polym. Prepr. Div. Polym. Chem.* **2002**, *43*, 319–320.

[52] D. Selli, M. Tawfilas, M. Mauri, R. Simonutti, C. Di Valentin, *Chem. Mater.* **2019**, *31*, 7531–7546.

[53] K. L. Materna, R. H. Crabtree, G. W. Brudvig, *Chem. Soc. Rev.* **2017**, *46*, 6099–6110.

[54] R. Luschtinetz, S. Gemming, G. Seifert, *Eur. Phys. J. Plus* **2011**, *126*, 1–13.

[55] T. Otsu, A. Kuriyama, **n.d.**, 37–41.

[56] B. Nomeir, O. Fabre, K. Ferji, *Macromolecules* **2019**, *52*, 6898–6903.

[57] Y. Zhu, E. Egap, *Polym. Chem.* **2020**, *11*, 1018–1024.

[58] A. Das, M. Patra, R. R. Wary, P. Gupta, R. G. Nair, *IOP Conf. Ser. Mater. Sci. Eng.* **2018**, *377*, DOI 10.1088/1757-899X/377/1/012101.

[59] C. Di Valentin, G. Pacchioni, A. Selloni, S. Livraghi, E. Giamello, *J. Phys. Chem. B* **2005**, *109*, 11414–11419.

[60] S. Livraghi, M. C. Paganini, E. Giamello, A. Selloni, C. Di Valentin, G. Pacchioni, *J. Am. Chem. Soc.* **2006**, *128*, 15666–15671.

[61] S. Livraghi, A. Votta, M. C. Paganini, E. Giamello, *Chem. Commun.* **2005**, 498–500.

[62] M. Chiesa, S. Livraghi, M. C. Paganini, E. Salvadori, E. Giamello, *Chem. Sci.* **2020**, *11*, 6623–6641.

[63] Y. Wang, C. Feng, M. Zhang, J. Yang, Z. Zhang, *Appl. Catal. B Environ.* **2010**, *100*, 84–90.

[64] C. Di Valentin, E. Finazzi, G. Pacchioni, A. Selloni, S. Livraghi, M. C. Paganini, E. Giamello, *Chem. Phys.* **2007**, *339*, 44–56.

[65] G. Barolo, S. Livraghi, M. Chiesa, M. C. Paganini, E. Giamello, *J. Phys. Chem. C* **2012**, *116*, 20887–20894.

[66] L. Schumacher, R. Marschall, *Top. Curr. Chem.* **2022**, *380*, 1–42.

[67] T. G. McKenzie, L. P. M. Da Costa, Q. Fu, D. E. Dunstan, G. G. Qiao, *Polym. Chem.* **2016**, *7*, 4246–4253.

[68] J. Xu, S. Shanmugam, N. A. Corrigan, C. Boyer, in *Control. Radic. Polym. Mech.*, **2015**, pp. 247–267.

[69] T. G. McKenzie, Q. Fu, E. H. H. Wong, D. E. Dunstan, G. G. Qiao, *Macromolecules* **2015**, *48*, 3864–3872.

[70] M. L. Allegrezza, N. De Alwis Watuthanthrige, Y. Wang, G. A. Garcia, H. Ren, D. Konkolewicz, *Polym. Chem.* **2020**, *11*, 6129–6133.

Chapter 4

One-pot PET-RAFT synthesis of soft-core nanoparticles for UpConversion

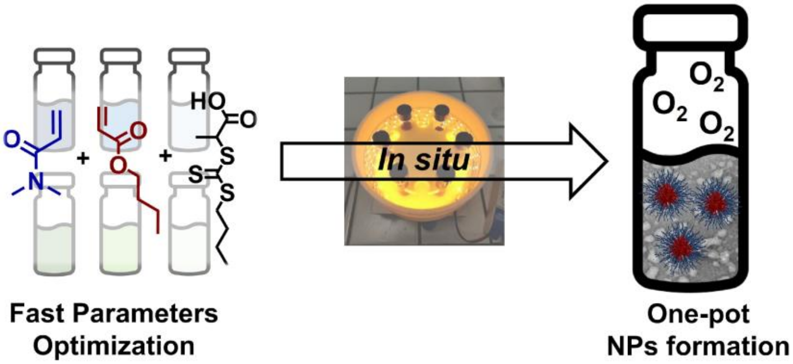

Part of this Chapter have been published as:

"V. Bellotti, G. Beretta, R. Simonutti, *Synthesis of soft-core hard-shell nanoparticles by visible PET-RAFT polymerization in dispersion conditions,* Polymer 271 (**2023**) 125804.

4.1 Introduction

The development of nano-size structures have revolutionized both scientific and industrial sectors conferring innovative characteristics upon established technologies or developing completely new materials. Among them, polymeric nanoparticles (NPs) spanning the range of 10 to 1000 nanometers in size have been deeply investigated and find applications as carriers or enclosures as biosensors,[1] catalysts,[2] drug delivery system (DDS),[3] in formulation chemistry such as in cosmesis[4] or as additives for improving mechanical properties of existing materials (*i.e.* food packaging[5]).

Traditionally, post-polymerization self-assembly of amphiphilic block copolymers by solvent switching[6] or co-precipitation[7,8] methods have been extensively used, giving access to the whole variety of possible nanoparticle morphologies. However, these methods are time-consuming and limited to meager solid concentrations (usually less than 1.0% w/w), thereby restricting their scalability and potential industrial uses. More recently, considerable attention is focused towards polymerization techniques able to generate the nanostructures without any post-polymerization treatments, with substantial solid content (ranging from 25% to 50% w/w) and notable monomer conversion rates. For this aim, polymerization in dispersion or emulsion conditions have been paired with reversible-deactivation radical polymerizations (RDRPs),[9–14] in particular RAFT,[15–20] culminating in the development of polymerization-induced self-assembly (PISA). The latter allows the production of NPs in both emulsion[21,22] (insoluble monomer) and dispersion conditions (soluble monomer but insoluble polymer),[23,24] without the need for any additional steric stabilizers, that are essential in common emulsion/dispersion polymerization. In fact, a solvophilic polymer end-capped with a RAFT functionality is used as both the stabilizing and macro-chain transfer agent for chain extension with a solvophobic block. As polymerization of the second block proceeds, the amphiphilicity of growing copolymer will increase, and bring about the *in situ* self-assembly of the nanoparticles with different morphologies.[25] If chain extension is carried out to total monomer conversion, post-polymerization purification is unnecessary.

Among the synthesized nanostructures, soft core nanocarriers are of significant interest, particularly where the inherent mobility of the encapsulated moiety should be preserved, such as in confining dyes for sensitized up-conversion (SUC)[26] or in the context of nano-reactors.[27] Photon upconversion (UC) consists in the emission of light at higher energy respect the excitation wavelength, which brings to promising applications in light-sensitive devices including photovoltaic, photochromic displays and biological imaging.[28] Conventional UC systems relying on nonlinear phenomena, as two-photon absorption, necessitate high excitation intensities. However, the more recent approach of sensitized triplet-triplet annihilation-based upconversion (sTTA-UC) presents an appealing alternative.[29] This method allows for the use of low-power densities, like solar irradiance. One of the main obstacles in UC systems is that achieving high upconversion yields is feasible only when the sensitizer-emitter pairs are dissolved in low viscosity solutions. However, efficiency diminishes in solid materials, which are nevertheless better suited for device integration.[30–32] This decline in efficiency is attributed to the diminished translational mobility of the sensitizer-emitter pair, precluding efficient collisions and orbital overlapping. The employment of core-shell nanoparticles is a valid solution for enhance efficiency in solid matter.[33,34] If the nanoparticles core is designed with a low-viscosity and hydrophobic polymer the inner part of the nanometer-scale container would resemble the properties in solution and the collision between the two encapsulated components within the confined volume will lead to higher orbital overlapping. Consequently, each nanoparticle operates as an independent up-conversion unit and the efficiency of TTA-UC is increased.

A well-suited candidate for generating stable soft nanoparticles in aqueous environments is poly(dimethyl acrylamide)-b-poly(butyl acrylate) (PDMA-b-PBA) copolymer. The hydrophilic and biocompatible PDMA offers good mechanical stability for the nanoparticle shell, while the PBA core should impart high mobility to the encapsulated components due to its very low glass transition temperature (T_g) of approximately -45°C. In a previous study, Charleux et al. successfully demonstrated the synthesis of PDMA-b-PBA nanoparticles using surfactant-free thermally activated RAFT polymerization under water emulsion conditions.[35] Their findings revealed that the particle dimensions ranged from 60 to 150 nm, with variations attributed to the molecular weight of the components.

Herein, we present a new robust and versatile synthetic protocol for the polymerization of amphiphilic PDMA-b-PBA soft nanoparticles *via* PET-RAFT polymerization as a confined system for up conversion using metal-based porphyrin as photoredox catalysts. The latter have undergone extensive investigation in various field, such as in organic synthesis,[36] photodynamic therapy,[37] and as sensitizers for up-conversion processes, applied in both solar-energy harvesting technologies and imaging.[38–41] Due to the poor water solubility of metal-based porphyrins they can be easily encapsulated into the nanoparticles, spontaneously migrating into the hydrophobic core during PISA. In so doing, the porphyrin acts both as the catalyst for the polymerization and the cargo for the desired application. The synthetic procedure has been finely optimized in terms of kinetics, morphology and PC encapsulation studies, using the well known Zinc tetraphenylporphyrin (ZnTPP) as the photocatalyst. Subsequently, Platinum octaethylporphyrin (PtOEP) has been tested for the first time as PC for PET-RAFT polymerization due to its better performance in TTA-UC process. Finally, after the emitter encapsulation the efficiency of this system for UC has been evaluated.

4.2 Materials and Methods

4.2.1 Materials

Methanol (MeOH) and diethyl ether were purchased from Honeywell, ethanol (EtOH), tetrahydrofuran GPC grade (THF), deuterated chloroform ($CDCl_3$), and deuterated DMSO were purchased from VWR. Zinc tetraphenyl porphyrin (ZnTPP), Platinum octaethylporphyrin (PtOEP), diphenyl anthracene (DPA), 1-butanethiol, carbon disulfide, 2-bromopropionic acid, N-dimethyl acrylamide (DMA), and butyl acrylate (BA) was purchased from Sigma-Aldrich. The monomers were purified in basic alumina column before use to remove the inhibitor. Ascorbic acid and dimethyl sulfoxide (DMSO) were purchased from Alfa Aesar. The orange and green LEDs source used was flexible LED RS pro LS IP20 series (SMD3528) with a peak wavelength $\lambda = 595$ nm and $\lambda = 530$ nm and a power of 4.8 W/m.

4.2.2 Experimental procedures

Synthesis of BTPA chain transfer agent

2-(n-butyltrithiocarbonate)-propionic acid (BTPA) was synthesized according to literature [42]. 1-butanethiol (0.040 mol, 3.61 g) and acetone (2.0 mL) were first added to a three-neck round flask equipped with a thermometer and dropping funnel can; then 50% NaOH solution (3.28 g) and water (6.0 mL) were introduced. The mixture was stirred for 30 minutes, bubbling nitrogen. Carbon disulfide (0.040 mol, 3.42 g) was added and the color turned to clear orange. After 30 minutes under stirring reaction was cooled in an ice bath reaching an internal temperature below 10°C and 2-bromopropionic acid (0.040 mol, 6.27 g) was added dropwise, followed by 3.28 g of 50% NaOH solution, stirred again for 30 minutes. Ice bath was removed and 6 mL of water was added, the mixture was stirred at room temperature for 24 hours. 10 mL of water was used to dilute the mixture, which was cooled again in order to slowly add HCl 10 M (6 mL) keeping the temperature below 10 °C. A yellow oil separated with the further formation of bright yellow solid, after 1 hour under stirring at low temperature the solid was collected by filtration, washed several times with water, and dry in high vacuum until constant weight. Purification occurred by recrystallization from hexane to give the desired product in high yield (7.48g, 78.5%).

PET-RAFT polymerization of Poly(dimethyl acrylamide)

Poly(dimethyl acrylamide) (PDMA) macro-CTA of different lengths was polymerized exploiting PET-RAFT polymerization photocatalyzed by ZnTPP. Firstly, a stock solution of ZnTPP in DMSO was prepared with a concentration of photocatalyst equal to 1 mg/mL. DMA (4387 mg, 44.25 mmol), BTPA (210.98 mg, 0.89 mmol; and 105.49 mg, 0.44 mmol), ZnTPP (1.5 mg, 2.2 x10^{-3} mmol) and 9 mL of DMSO were added to a 4 mL vial. The selected ratios were [DMA]:[BTPA] = 50:1 and 100:1 respectively, and [DMA]/[ZnTPP] = 50 ppm . Without any deoxygenation step, the vial was sealed and irradiated with orange light (λ_{max} = 595 nm) for 24 hours under stirring at room temperature. The moment in which the light source is turned on is considered the polymerization initial time (t_0). NMR of the crude product was used for determinate monomer conversion. Precipitation in diethyl ether allows the ZnTPP removal, the product was centrifuged at 8000 rpm for 10 minutes at 10 °C, washed three times, and dried in vacuum till constant weight. DSC analysis was used to determine the glass transition temperature (first cycle from 25 °C to 200 °C with heating rate of 20 °C/min followed by cooling and a final heating cycle till 200 °C, under nitrogen flow), GPC with PS standard displayed the M_n and dispersity.

Chain extension experiments with BA by PET-RAFT PISA polymerization with ZnTPP

Polymerization-induced self-assembly of n-butyl acrylate (BA) was performed using the previously synthesized poly(dimethyl acrylamide) ($PDMA_{47}$ and $PDMA_{99}$) as macro-CTA in two different alcoholic solvents, ethanol, and methanol. Since ZnTPP is not well soluble in these polar mediums a stock solution in THF was prepared, with a concentration of 1 mg/mL, and the solvent was removed by evaporation under nitrogen stream before the addition of the reaction mixture. In a classic experiment BA (214 mg, 1.67 mmol), $PDMA_{47}$ (39.05 mg, 0.008 mmol) or $PDMA_{99}$ (83.77 mg, 0.008 mmol), ZnTPP (0.06 mg, 8.33x10^{-5}), ascorbic acid (3.81 mg, 0.02

mmol) and 3 mL of the alcoholic mixture (EtOH and MeOH water mixture 70/30, 75/25, 80/20, 85/25, 90/10), with a ratio of [BA]:[PDMA]:[ZnTPP] = 200:1:0.01 were added to a 4 mL vials equipped with rubber septum, following a previous work of Boyer et al.[43]. In order to achieve different PDMA/PBA volume fractions also [BA]:[PDMA] = 850:1 and 125:50 ratio were also attempted. Nitrogen was purged through the reaction mixture for 1 hour in an ice bath at 0 °C in order to remove oxygen. The polymerization mixture was irradiated with orange light (λ_{max} = 595 nm) at room temperature under vigorous stirring for 24 hours before it was quenched by exposure to air in an ice bath and stored in the dark. The crude product was analyzed by NMR and purified in dialysis against pure water for two days. GPC with PS standard displayed the M_n and Đ and DLS and TEM microscopy were used to study the average diameter size and particle morphology.

General procedure for one-pot PET-RAFT PISA polymerization

Polymerization-induced self-assembly of BA was repeated, maintaining the same experimental conditions but in a one-pot strategy. DMA has been firstly used for the polymerization of the first hydrophilic macro-CTA. DMA (165.2 mg, 1.67 mmol) was dissolved in 2 mL of EtOH:H_2O (70:30) mixture together with BTPA (7.94 mg, 0.033 mmol; and 3.97 mg, 0.0167 mmol), ascorbic acid (15.26 mg, 0.09 mmol; and 7.63 mg, 0.04 mmol) and ZnTPP (0.06 mg, 8.33e^{-05} mmol) from the stock solution in THF. The selected ratios were: [DMA]:[CTA]=50:1 and 100:1, and [BA]:[macro-CTA]=200:1 and 400:1, where the macro-CTA amount was calculated considering the complete conversion of the PDMA block. The amount of PC ([ZnTPP]/[BA]=50 ppm) was calculated considering only the amount of the second monomer. The reaction mixture was added to an 8 mL vial equipped with a rubber septum and purged with nitrogen for 1 hour in an ice bath at 0 °C in order to remove oxygen. The polymerization mixture was irradiated with orange light (λ_{max} = 595 nm) at room temperature under vigorous stirring for 19 hours. The second solution of BA (854 mg, 6.66 mmol) in 3 mL of EtOH/H_2O mixture and ZnTPP (0.17 mg, 2.50 x10^{-4} mmol) was degassed and added to the reaction environment under nitrogen flux. The polymerization was stopped 24 hours after the addition of the second solution. NMR analysis of the crude product in d-DMSO was performed to calculate monomer conversion, GPC with PS standard displayed the M_n and Đ and DLS and TEM microscopy were used to study the average diameter size and particle morphology.

Chain extension experiments with BA by PET-RAFT PISA polymerization with PtOEP

Following the previously described method for polymerization-induced self-assembly of n-butyl acrylate (BA) with ZnTPP, the nanoparticles synthesis was repeated by using PtOEP as photoredox catalyst. Since PtOEP is not well soluble in these polar mediums a stock solution in THF was prepared, with a concentration of 1 mg/mL, and the solvent was removed by evaporation under nitrogen stream before the addition of the reaction mixture. In a classic experiment BA (214 mg, 1.67 mmol), $PDMA_{47}$ (39.05 mg, 0.008 mmol), PtOEP (182 µg, 2.5 x 10^{-4} mmol, 182 µL of the stock solution), ascorbic acid (3.81 mg, 0.02 mmol) and 3 mL of EtOH/water mixture 70/30, with a ratio of [BA]:[PDMA]:[PtOEP] = 200:1:0.03 were added to a 4 mL vials equipped with rubber septum. Nitrogen was purged through the reaction mixture for 1 hour in an ice bath at 0 °C in order to remove oxygen. The polymerization mixture was irradiated with green light (λ_{max} = 530 nm) at room temperature under vigorous stirring for 24 hours before it was quenched by exposure to air in an ice bath and stored in the dark. The crude product was analyzed by NMR and purified in dialysis against pure water for two days. GPC with PS standard displayed the M_n and Đ and DLS and TEM microscopy were used to study the average diameter size and particle morphology. Finally, UV-visible spectroscopy with an integrated sphere was used to calculate the amount of encapsulated porphyrin.

Addition of the emitter

Encapsulation of 9,10-diphenylantracene (DPA) has been performed by addition drop by drop of a 12.75 mg/mL stock solution in dichloromethane (DCM), [DPA]:[PtOEP]=50. The reaction mixture was left under stirring overnight without the cap in order to let the DCM evaporate.

4.3 Results and Discussion

4.3.1 Synthesis of PDMA-b-PBA nanoparticles with ZnTPP photocatalyst

In order to initiate our study, poly(dimethyl acrylamide) (PDMA) was synthesized by PET-RAFT polymerization with ZnTPP, in a 3D printed home-made photoreactor under orange irradiation (**Scheme 4.1**). Poly(dimethyl acrylamide) was selected as the polymer constituting the hydrophilic NPs shell due to its high T_g in the solid state, which would provide additional mechanical stability of the final material. 2-(butyltrithiocarbonothioyl-thio)propionic acid (BTPA) was used as the chain transfer agent due to its higher compatibility for the polymerization of acrylates in presence of ZnTPP. In fact, it was previously reported that the Zn metal center of the porphyrin strongly interact with trithiocarbonates rather than other CTA families, reassembling interaction similar to the ones occurring in nature.[44–46]

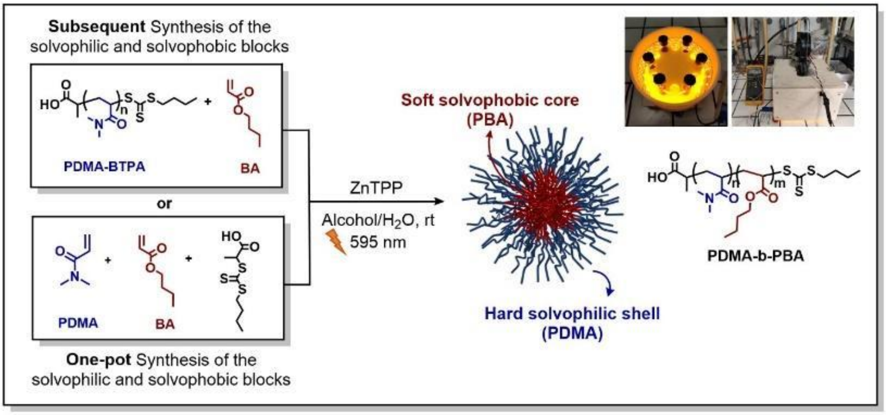

Scheme 4.1: Two steps synthesis of PDMA-b-PBA block copolymer in dispersion conditions using BTPA as chain transfer agent and ZnTPP and photocatalyst under orange light inside a designed 3D printed photo- reactor. Chain extension experiments were conducted both in a subsequent way, including the purification step of the macro-CTA, and in a one-pot fashion.

Two different PDMA chain lengths were targeted by increasing the monomer to CTA ratio (50 and 100), with the aim of providing different thickness to the polymeric shell. In both cases high yield, 95% (DP_n=47) and 99% (DP_n=99) respectively, and good dispersity (Đ = 1.05 and 1.07, **Figure 4.1**) were obtained in the presence of oxygen.

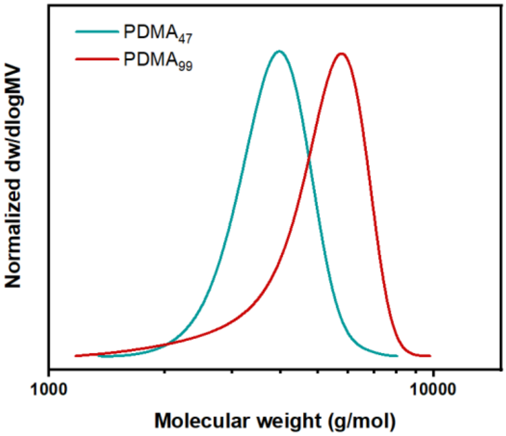

Figure 4.1: SEC trace of PDMA synthesized via PET-RAFT polymerization with 2-(n-butyltrithiocarbonate)-propionic acid as a chain transfer agent ([CTA]:[MMA] = 1:50, Mn = 4,700; Đ = 1.05), ([CTA]:[MMA] = 1:100, Mn = 9,800; Đ = 1.07).

The PDMA homopolymer was used as macro-CTA for the dispersion polymerization of butyl acrylate. The most common monomer used for PISA protocol in dispersion condition, as the solvophobic block, is benzyl methacrylate due to its perfect solubility in ethanol, in which the polymer is not soluble.[47–50] On the other hand, *n*-butyl acrylate is not commonly used for this purpose and solvent optimization was required. Ethanol and methanol were herein selected as dispersing media and different amounts of water were added (**Table 4.1**).

Table 4.1: Dispersion polymerization of BA with PDMA$_{47}$ and PDMA$_{99}$ macro-CTA in ethanol and methanol mixtures with water. Polymerization preceded for 24 hours except for sample 4 (*) which was stopped after 28 hours. [ZnTPP]/[BA] = 50 ppm and [PDMA macro-CTA]:[BA] = 1:200. [a] Water fraction respects the total amount of alcoholic mixture. [b] Monomer conversion calculated with NMR analysis. **[c]** Volume fraction calculated using $\rho_{(PDMA)} = 1.21$ g/cm^3 and $\rho_{(PBA)} = 1.087$ g/cm^3. **[d]** Molecular weight of PDMA-b-PBA polymers calculated with NMR analysis. [e] Dispersity obtained by GPC measures.

Solvent	**Entry**	**x(H_2O)[a]**	**α (%)[b]**	**$DP_{n,PBA}$**	**f_{PBA}[c]**	**M_n (Da) [d]**	**Đ[e]**
EtOH	PDMA$_{47}$-b-PBA$_{153}$ (1)	0	76.7	153	0.78	24 300	N.A.
	PDMA$_{47}$-b-PBA$_{143}$ (2)	0.1	71.7	143	0.77	23 350	1.17
	PDMA$_{47}$-b-PBA$_{150}$ (3)	0.15	75.1	150	0.78	23 950	1.25
	PDMA$_{47}$-b-PBA$_{174}$ (4)*	0.2	86.8	174	0.80	26 700	1.18
	PDMA$_{47}$-b-PBA$_{165}$ (5)	0.25	82.3	165	0.80	25 800	1.20
	PDMA$_{47}$-b-PBA$_{183}$ (6)	0.3	91.3	183	0.81	27 900	1.27
MeOH	PDMA$_{47}$-b-PBA$_{146}$ (7)	0	73.2	146	0.78	23 450	N.A.
	PDMA$_{47}$-b-PBA$_{140}$ (8)	0.1	70.2	140	0.77	22 450	1.22
	PDMA$_{47}$-b-PBA$_{164}$ (9)	0.15	81.9	164	0.80	25 670	1.14
	PDMA$_{47}$-b-PBA$_{166}$ (10)	0.2	83.2	166	0.80	25 800	1.23
	PDMA$_{47}$-b-PBA$_{180}$ (11)	0.25	89.9	180	0.81	27 800	1.08
	PDMA$_{47}$-b-PBA$_{197}$ (12)	0.3	98.4	197	0.82	29 700	1.31

Solvent	**Entry**	**$x(H_2O)$[a]**	**α (%)[b]**	**$DP_{n,PBA}$**	**f_{PBA}[c]**	**M_n (Da) [d]**	**Đ[e]**
EtOH	$PDMA_{99}$-b-PBA_{135} (13)	0.1	67.4	135	0.60	27 300	1.27
	$PDMA_{99}$-b-PBA_{140} (14)	0.15	70.1	140	0.61	28 000	1.27
	$PDMA_{99}$-b-PBA_{169} (15)	0.25	84.5	169	0.66	31 700	1.25
	$PDMA_{99}$-b-PBA_{180} (16)	0.3	90.2	180	0.67	33 200	1.29
MeOH	$PDMA_{99}$-b-PBA_{144} (17)	0.1	72.2	144	0.62	28 500	1.20
	$PDMA_{99}$-b-PBA_{169} (18)	0.15	84.3	169	0.65	31 700	1.19
	$PDMA_{99}$-b-PBA_{175} (19)	0.2	87.4	175	0.66	32 500	1.09
	$PDMA_{99}$-b-PBA_{187} (20)	0.25	93.7	187	0.68	34 100	1.12
	$PDMA_{99}$-b-PBA_{190} (21)	0.3	94.8	190	0.68	34 400	1.11

Chain extension was confirmed by ^{1}H NMR analysis of the crude reaction mixture by comparing the monomer vinyl protons (6.3 ppm) with the side chain $–CH_3$ of the resulting polymer (**Figure 4.2a**). Accordingly, GPC traces shifted to higher molecular weights (**Figure 4.2b**), with respect to the macro-CTA, preserving low dispersity values. These considerations, together with a linear increase of the $\ln([M]_0/[M]_t)$ over time (**Figure 4.2c**), suggest a control behavior of the polymerization, typical of RDRPs.

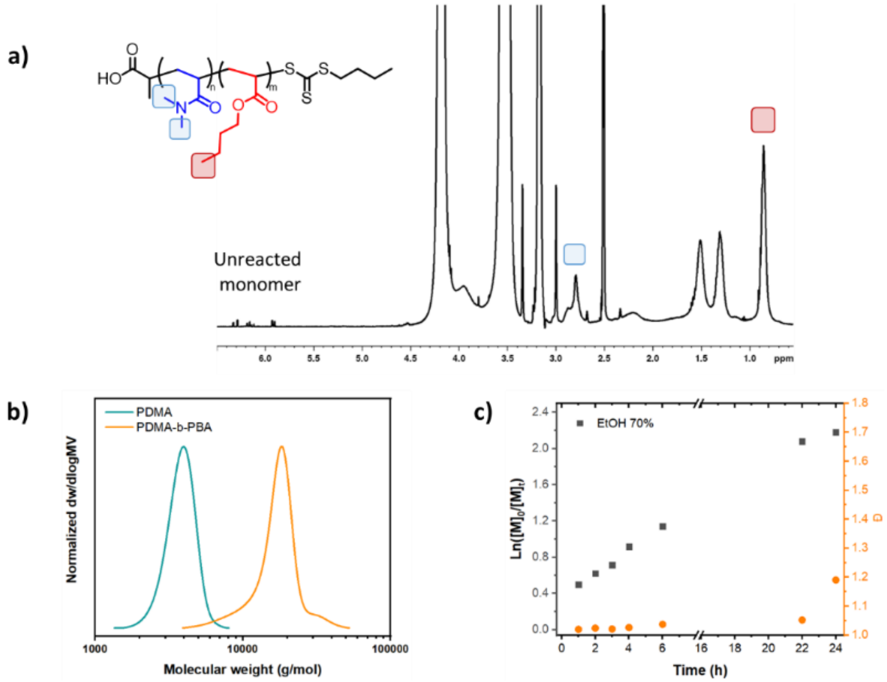

Figure 4.2: a) NMR spectrum of $PDMA_{47}$-b-PBA_{183} (6) crude product and b) SEC traces of PDMA macro-CTA (M_n = 4 700 Da, Đ = 1.05), and after the chain extension with PBA in 70% EtOH solution, $PDMA_{47}$-b-PBA_{183} (6) (M_n = 27 900 Da, Đ = 1.27). c) Kinetic study of the chain extension experiment with n-BA in EtOH 70% media ($PDMA_{47}$-b-PBA_{183} (6)).

The final nanomaterials were characterized before and after purification through dialysis against pure water by DLS and TEM. A detailed morphological analysis is discussed below (**Figures** from **4.4** to **4.7**).

Kinetic studies of NPs formation

When the PBA conversion after 24 hours is analyzed in both ethanol and methanol media with increasing amounts of water a linear trend between the polymerization kinetics and the water fraction in the alcoholic media was noticed, as shown in **Figure 4.3**. In particular, higher amounts of water resulted in higher butyl acrylate conversion.

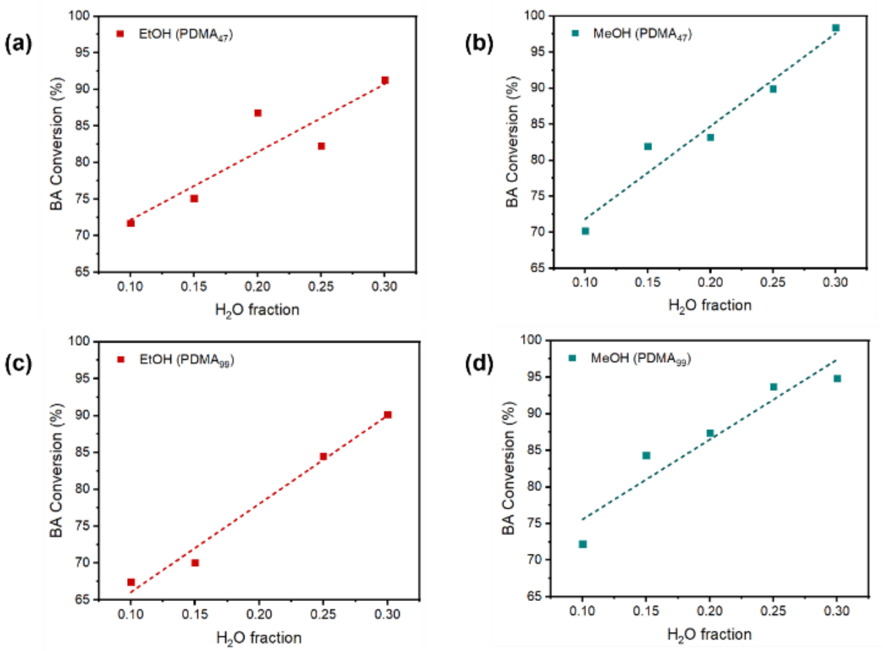

Figure 4.3: Monomer conversion versus water fraction of chain extension experiments of butyl acrylate using PDMA macro-CTA in both ethanol (red squares) and methanol (green squares) alcoholic media. Chain extension with $PDMA_{47}$ macro CTA are represented in graphic a) and b) whereas for c) and d) $PDMA_{99}$ was used.

The observed behavior is in accordance with the formation of NPs considering that the micelle formation/growth and the polymerization kinetic are interconnected and, in this case, strictly related with the water amount. Poly(butyl acrylate) exhibits high solubility in apolar solvent and it can be dissolved in both ethanol and methanol whereas it’s high insoluble in water, consequently, formation of NPs is faster when the H_2O to alcohol ratio is higher. With the newly formed particles a new poly(butyl acrylate) rich domain is formed, where the affinity of the monomer is higher with respect to the solvent. The present situation resembles an emulsion polymerization, as mentioned by Warren et al.,[51] and the reaction rate accelerates. Interestingly, the slope of the linear plots reported in **Figure 4.3** is not influenced by the length of the solvophilic shell. The final conversion of the chain extension in pure ethanol and methanol (**Table 4.1**, entries 1 and 7) were excluded from the discussion because no particles were observed (discussion follow), meaning that the kinetic of the process is no longer the one of dispersion polymerization.

Nanoparticles morphology

Not only the polymerization kinetic is related to the amount of water but also the nanoparticles' morphology relies on it. When pure alcohol is used as polymerization media core segregation is not thermodynamically favored due to the limited, but still high enough, solubility of PBA. The result, confirmed by DLS, is a PET-RAFT polymerization of linear PDMA-b-PBA diblock copolymer in solution. When water is added to the crude product mixture, achieving a total water fraction of $x(H_2O) = 0.3$, nanoparticles are quickly formed, as occur in post polymerization self-assembly (**Figure 4.4**).

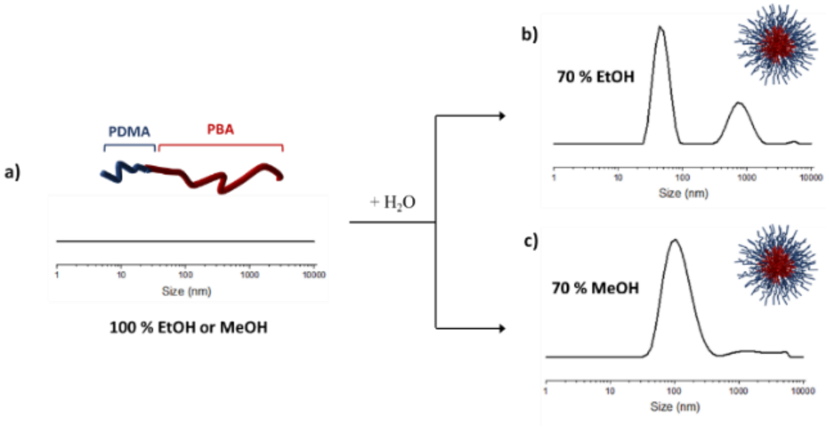

Figure 4.4: DLS analysis of samples a) PDMA$_{47}$-b-PBA$_{153}$ (1) and PDMA$_{47}$-b-PBA$_{146}$ (7) at the end of the chain extension experiments in pure alcohol and b), c) after the addition of water until reaching a solution of alcohol/water = 70:30. The absence of peaks after the polymerization indicate that pure MeOH and EtOH are not good solvents for the polymerization self-assemble of nanoparticles.

Therefore, addition of small amounts of water is necessary in order to decrease the solubility of the polymer while maintaining sufficient solubility of the monomer. In fact, it was previously reported that dispersion polymerization of homo-poly(butyl acrylate) could be achieved in in 70% EtOH and 90% MeOH/water mixtures.[52] However, the addition of different amounts of water increases the complexity of the system and to rationalize the morphologic behavior observed the interactions between the dispersing media with the monomer, the stabilizer shell and the solvophobic block have been considered.

When the nanoparticles are produced in ethanol aqueous media a simple spherical-like morphology is obtained, whereas methanol-derived particles present a more complex second-order morphology as shown in **Figure 4.5**.

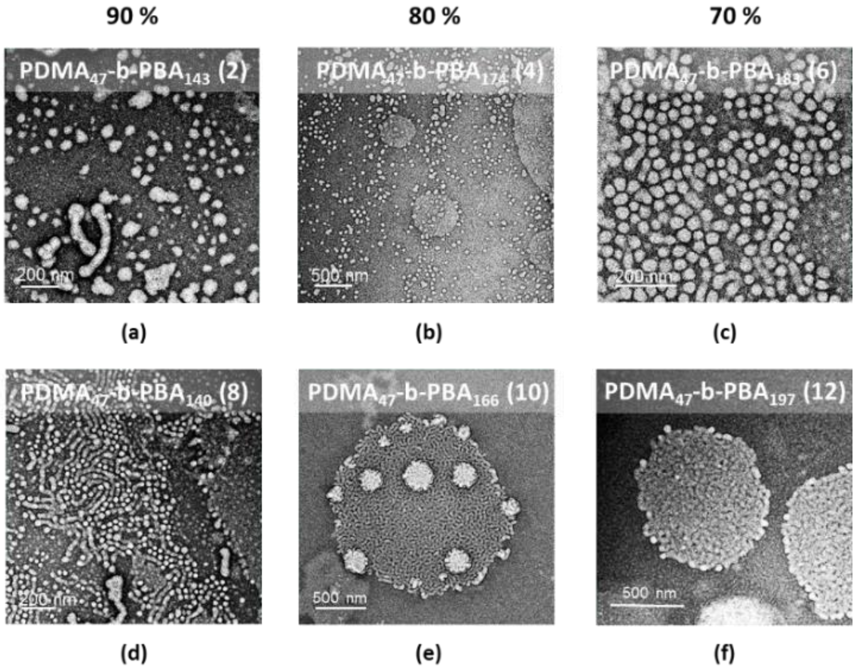

Figure 4.5: TEM images of PDMA-b-PBA nanoparticles in water, self-assembled from different solvents. In the first row are represented the NPs synthetized from EtOH/water mixture: (a) 90:10 with a spherical and worm-like morphology, (b) and (c) respectively 80:20 and 70:30 with spherical morphology. In the second row are represented the NPs synthetized from MeOH/water mixture: (d) 90:10 with a spherical and worm-like morphology, (e) and (f) respectively 80:20 and 70:30 with second order morphology in which particles tend to agglomerate in more complex structures.

In order to rationalize the different morphologies Flory-Huggins interaction parameters (χ_{P-S}) between the solvophilic shell PDMA (P) and the solvents (S) has been taken into account. The value of χ_{P-S} can be easy estimated by the Hansen solubility parameters as reported in the formula below:

$$\chi_{P-S} = \left(\frac{V_m}{RT}\right)\left[\left(\delta_D^S - \delta_D^P\right)^2 + 0.25\left(\delta_P^S - \delta_P^P\right)^2 + 0.25\left(\delta_H^S - \delta_H^P\right)^2\right] \quad (4.1)$$

where δ_D, δ_P and δ_H are the contributions of dispersion forces, polar interactions and hydrogen bonds to solubility, respectively, V_m is the molar volume of the solvent, T is temperature and R is the gas constant.

Given that, high solubility of the polymer chain (P) in the considered solvent (S) is expected for small value of χ, the resulted Flory-Huggins interaction parameters ($\chi_{PDMA-MeOH} = 0.214$, $\chi_{PDMA-EtOH} = 0.4$ and $\chi_{PDMA-H_2O} = 0.48$) indicates that PDMA has stronger interaction with MeOH than EtOH and its solubility decreases in pure water (MeOH > EtOH > H_2O).

In fact, considering the DLS curve of the NPs pre and post dialysis synthetized in methanol (**Figure 4.6**, left side), when low water fraction was used (x_{H_2O}= 0.1) a single and narrow peak with an average size of 47 nm is obtained. By increasing the amount of water to x_{H_2O}= 0.2 and x_{H_2O}= 0.3 a second broad peak appears (**Table 4.2** entries 10, and 12). This result is in perfect accordance with the decreased ability of water to solvate the shell with respect to methanol, which induced a partial agglomeration. In the same way, after dialysis against pure water the Flory-Huggins interaction parameters increase and the second peak in DLS shifts toward higher hydrodynamic radius while the first one remains at similar size. The hierarchical aggregation in second order structures of PDMA core-shell NPs have been reported in water and attributed to strong attractive forces between the short coronas.[8]

On the other hand, ethanol and water have similar interactions with the PDMA corona, for this reason the trend is less appreciable when pre and post dialysis DLS curves are considered. Anyhow, another interesting behavior is shown in EtOH media, related with the dimension of the particles at small average size ($<D_H>1$). An opposite trend can be noticed in **Table 4.2** when the water fraction is decreased: the nanoparticles' average size of the first peak increases. The interaction of the PDMA coronas with the reaction media and themselves is not enough in this case to explain the trend. In fact, for sample $PDMA_{47}$-b-PBA_{143} (2) the dimension shifts from 452 nm post-polymerization to 61 nm after dialysis. To rationalize the change in dimension the solubility of PBA crore should be considered. In fact, it was previously demonstrated that dispersion polymerization of PBA without any stabilizer block results in controlled nanoparticles formation when ethanol content is lower than 80%. On the other hand, higher values causes a drastic drop in the recover polymer due to an appreciable amounts that remained solubilized in the solvent.[52] Due to the higher solubility of the core in ethanol rather that in methanol, in the first case the core is considerably swollen decreasing the control over the dispersion process which is less thermodynamic favored. The bigger particles shrink when water is added during dialysis, resulting in drastic decreases of the size in uncontrolled ways due to the rapid change of dispersion medium, bringing to the formation of anisotropic morphologies such as worm-like structures (**Figure 4.5a**).

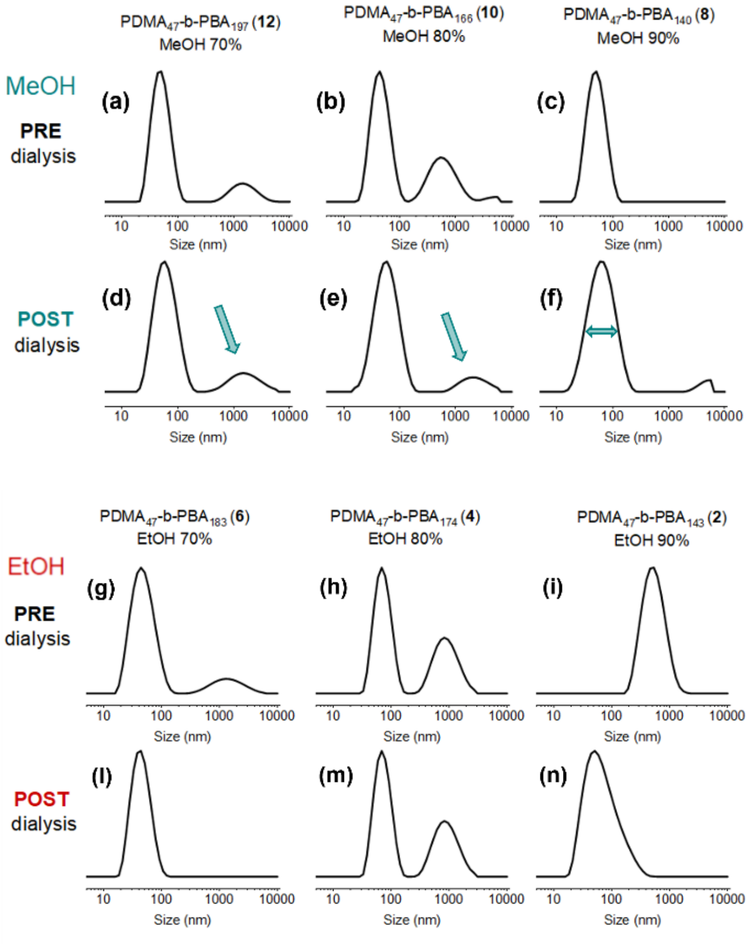

Figure 4.6: DLS analysis pre (first line) and post (second line) dialysis in methanol (left) and ethanol (right) with different water content. (a, d, g and l) alcohol/water mixture 70:30; (b, e, h and m) alcohol/water mixture 80:20; (c, f, i and n) alcohol/water mixture 90:10.

Table 4.2: DLS maximum peaks (<D_H>1 refers to the first peaks and <D_H>2 to the second one) pre and after dialysis in water of the synthetized nanoparticles

NPs from MeOH							
Entry	**x(H_2O)**	**PRE dialysis**			**POST dialysis**		
		<D_H>1 (nm)	**<D_H>2 (nm)**	**PdI**	**<D_H>1 (nm)**	**<D_H>2 (nm)**	**PdI**
PDMA$_{47}$-b-PBA$_{197}$ (12)	0.3	52.4	1651	0.3	65	1821	0.32
PDMA$_{47}$-b-PBA$_{166}$ (10)	0.2	47.4	652	0.53	62.4	2350	0.34
PDMA$_{47}$-b-PBA$_{140}$ (8)	0.1	46.7	--	0.12	58.5	--	0.26
PDMA$_{47}$-b-PBA$_{146}$ (7)	0	No formation of NPs					
NPs from EtOH							
PDMA$_{47}$-b-PBA$_{183}$ (6)	0.3	43.8	1484	0.3	46.8	--	0.23
PDMA$_{47}$-b-PBA$_{174}$ (4)	0.2	73.6	976	0.55	80.3	1267	0.37
PDMA$_{47}$-b-PBA$_{143}$ (2)	0.1	452	--	0.27	61.7	--	0.34
PDMA$_{47}$-b-PBA$_{153}$ (1)	0	No formation of NPs					

Finally, the volume fraction of the core and shell forming blocks is an important parameter to regulate the particle's morphology. Nanoparticles with increasing volume fraction of PDMA have been synthesized, equal to f_{PDMA} = 0.12, 0.19, 0.27 and 0.33 in EtOH 70% (**Table 4.3**). In **Figure 4.7.** It is appreciable that the nanoparticles dimension, when normalized with respect to the molecular weight, linearly increases with the corona volume fraction indicating a stronger contribution of the latter to the final NPs size. In addition, when the DLS curve is considered, a single monodisperse peak is obtained for $0.12 < f_{PDMA} < 0.27$, suggesting a spherical morphology as obtained for previous cases (**Figure 4.5c**). When $f_{PDMA} > 0.3$ more than two peaks appear in the DLS curve, indicating that aggregate are formed, probably due to the stronger interaction between the polar corona chains of the neighboring NPs, repelling the solvent.
When $f_{PDMA} > 0.3$ more than two peaks appear in the DLS curve, indicating that aggregate are formed, probably due to the stronger interaction between the polar corona chains of the neighboring NPs, repelling the solvent.

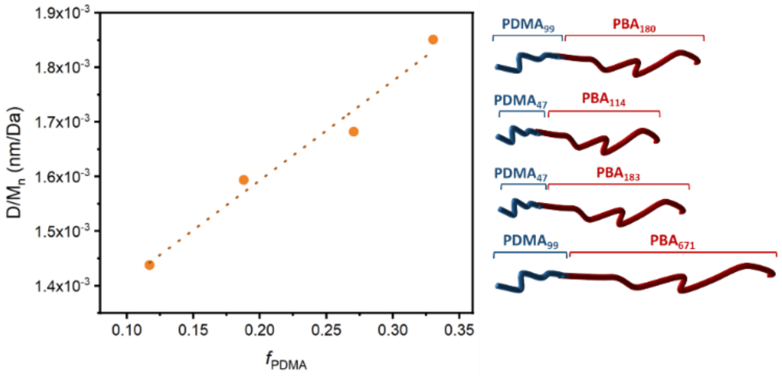

Figure 4.7: Average particle size, normalized respect the molecular weight, (orange dots) versus PDMA volume fraction. Increasing the volume of PDMA block respect to the hydrophobic core agglomeration of nanoparticle occurs.

Table 4.3: Dispersion polymerization of BA with $PDMA_{47}$ and $PDMA_{99}$ macro-CTA in ethanol/water mixtures 70/30. Polymerization proceeded for 24 hours under orange light irradiation (λ_{max} = 595 nm) and different PDMA/PBA length have been synthetized using [PDMA macro-CTA]:[BA] = 1:200 for samples 6 and 16, 1:850 for 22 and 1:150 for 23. [a] Volume fraction calculated using $\rho_{(PDMA)} = 1.21\ g/cm^3$ and $\rho_{(PBA)} = 1.087\ g/cm^3$. [b] Monomer conversion and molecular weight calculated with NMR analysis. [c] Morphology analysed by DLS and TEM, S = sphere.

$PDMA_n$-b-PBA_m NPs from EtOH 70%

Sample	f_{PBA}[a]	f_{PDMA}[a]	M_n (Da)[b]	Morphology[c]
$PDMA_{99}$-b-PBA_{671} (22)	0.88	0.12	96 100	S
$PDMA_{47}$-b-PBA_{183} (6)	0.81	0.19	27 900	S
$PDMA_{47}$-b-PBA_{114} (23)	0.73	0.27	19 300	S
$PDMA_{99}$-b-PBA_{180} (16)	0.67	0.33	33 200	aggregate

One-pot synthesis of PDMA-b-PBA nanoparticles

From a scaling-up perspective the synthesis of the nanoparticles should be not only as easy as possible, but also trying to meet the green chemistry requirements. To do so we aim to remove any intermediate purification steps (*i.e.* PDMA macro-CTA) and use non-toxic solvents (*i.e.* ethanol and water). Therefore, one-pot PET-RAFT polymerization for the formation of PDMA-b-PBA nanoparticles was studied. Unfortunately, one-pot one-step synthesis is not possible for this system due to the very similar reactivity ratio of BA and DMA which would end up with the concomitant formation of both statistical copolymers and homopolymers chains without the presence of separate blocks.[53] On the other hand, for the one-pot two-steps procedure dimethylacrylate has been polymerized overnight in ethanol aqueous media and the reaction stopped by simply switching off the light, exploiting the temporal control of PET-RAFT polymerization. A solution of the second monomer was added and the polymerization restored by switching on the light. Turbid and homogeneous solution was obtained after 24 hours and the formation of a block copolymer was encouraged by ^{1}H NMR analysis, that highlighted the presence of both PDMA and PBA peaks (**Figure 4.8a**), a single polymer population which was supported by a single GPC elution peak (**Figure 4.8b**), and the DLS/TEM analysis confirmed the formation of spherical nanoparticles (**Figure 4.9**), as expected for the selected solvent (EtOH 70%), with an average size of 54 nm.

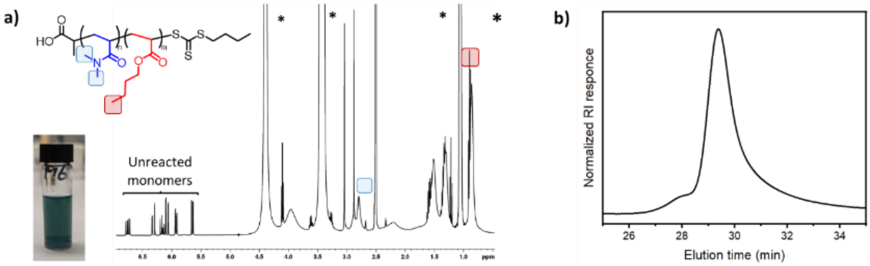

Figure 4.8: a) ^{1}H NMR spectrum of the crude product and b) SEC trace of one-pot polymerization (PDMA$_{21}$-b-PBA$_{173}$ (24))

Table 4.4: One-pot polymerization of PDMA-b-PBA nanoparticles in ethanol water mixtures 70:30. Polymerization proceeded for 34 hours. [a] Conversion of BA calculated by NMR of the crude product, in case of one-step polymerization conversion refers to the precipitate. [b] Conversion of dimethyl(acrylamide) calculated by NMR of the purified product by comparison of PDMA and PBA peaks. [c] Molecular weight obtained by the sum of M$_{n,\ PDMA}$ and M$_{n,\ PBA}$ calculated by NMR. [d] Dispersity obtained by GPC measures. [e] Nanoparticle formation observed with DLS.

One-pot PISA of PDMA$_n$-b-PBA$_m$					
Sample	**α_{BA} (%)[a]**	**α_{DMA} (%)[b]**	**M$_n$ (Da) [c]**	**Đ[d]**	**NPs[e]**
PDMA$_{21}$-b-PBA$_{173}$ (24)	86.5	42.1	24 300	1.17	yes
PDMA$_{56}$-b-PBA$_{355}$ (25)	88.7	55.5	51 000	1.24	yes

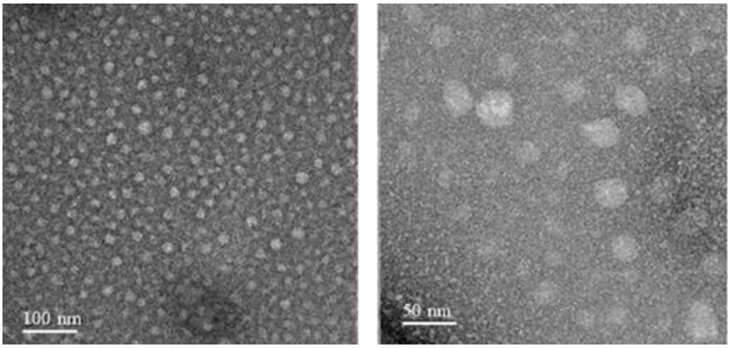

Figure 4.9: TEM images of PDMA$_{56}$-b-PBA$_{355}$ (26) nanoparticles in water obtained by one-pot two-steps PET-RAFT PISA polymerization.

ZnTPP encapsulation during self-assembly

As mentioned in the introduction, metal porphyrin-based compounds have been extensively investigated as sensitizer for up-conversion with application in various fields.[40,41] Even though ZnTPP is not widely exploited as sensitizer in UC it can be used as photosensitizer for singlet oxygen production in photodynamic therapy.[37] For this reasons, we decided to study the possible encapsulation of ZnTPP during the polymerization induced self-assembly process as a simple and reduced-waste protocol for the synthesis of nanoparticles for photodynamic therapy.

When the nanoparticles start to assemble, a new solvophobic region composed by PBA and BA is formed. It is therefore plausible that the photocatalyst, which is more soluble in apolar media due to its high conjugate structure, would spontaneously migrate inside the particle hydrophobic core. ZnTPP encapsulation was determined by UV-visible spectroscopy of the dialysed nanoparticles considering the peaks at 426 nm (**Figure 4.10a**) and interpolating the absorbance with a ZnTPP calibration curve in butyl acetate. The amount of ZnTPP encapsulated into the nanoparticles was found to be related to the water content and the alcohol nature (**Figure 4.10b**). In particular, both ethanol and methanol exhibited greater ZnTPP content after dialysis when the polymerization was conducted in a dispersing media with low amount of water; conversely, the content decreased for dispersing media with higher water fractions. This pattern can be associated with the well-established phenomenon of ZnTPP dimerization in water-rich environments.[54] Nevertheless, in ethanol, the quantity of encapsulated porphyrin remained significant, exceeding 4%.

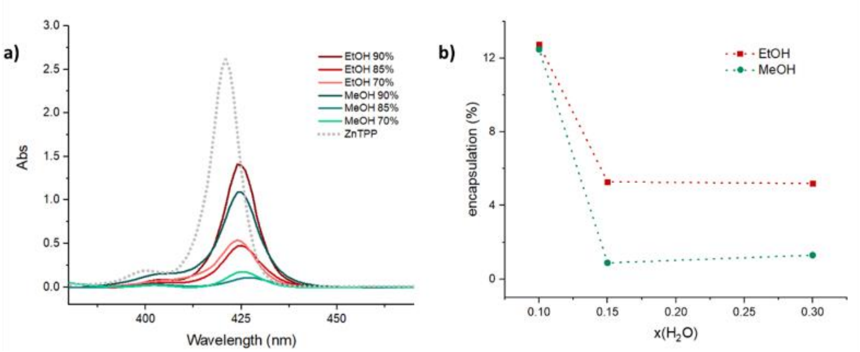

Figure 4.10: (a) UV-visible spectra of purified NPs (starting from $PDMA_{47}$ macro-CTA) synthesize in various alcoholic environments with different water fractions compared with absorption spectrum of ZnTPP in butyl acetate. (b) encapsulation percentage of ZnTPP calculated by interpolation of maximum absorbance at 426 nm with a ZnTPP calibration curve versus water fraction.

4.3.2 PtOEP as photocatalyst for NPs production and upconversion evaluation

The optimized procedure for the synthesis of soft-core hard-shell nanoparticles was then employed for the one-pot production of nanomaterials for upconversion (**Scheme 4.2**). For this aim ZnTPP was replaced by PtOEP because this last is far more efficient for upconversion purposes. Due to the similar solubility of the two metal-based porphyrins it is expected that, during the chain-extension PISA polymerization in alcohol/aqueous media, the PtOEP will undergo similar migration into the nanoparticle core, in the same fashion as ZnTPP.

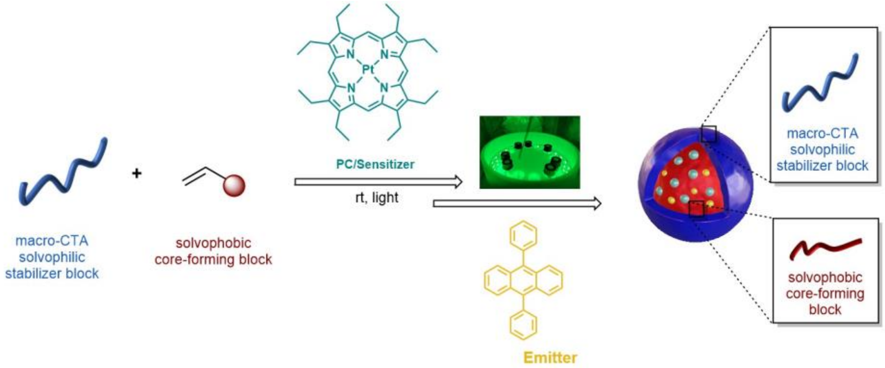

Scheme 4.2: Schematic representation of the one-pot production of UC polymeric nanoparticles *via* PET-RAFT polymerization.

The chain-extension experiment was performed in EtOH 70% in order to obtain spherical nanoparticles, reducing the core swelling and maximizing the particle's growth control. No polymerization could be observed when orange LED was used due to the blue shift of the absorption peak of PtOEP with respect to ZnTPP, for this reason green irradiation (λ_{max} = 520 nm) was used to initiate the polymerization. Remarkably, PtOEP has proven to be an effective photocatalyst for PET-RAFT polymerization, used herein for the first time. ^{1}H NMR of the crude product confirmed the success of the chain-extension with lower conversion with respect to the previous ZnTPP catalyst (α = 66%). In addition, DLS and TEM (**Figure 4.11**) analysis show the presence of nanoparticles with an average size of 43.4 nm and spherical morphology, consistent with the results obtained with ZnTPP.

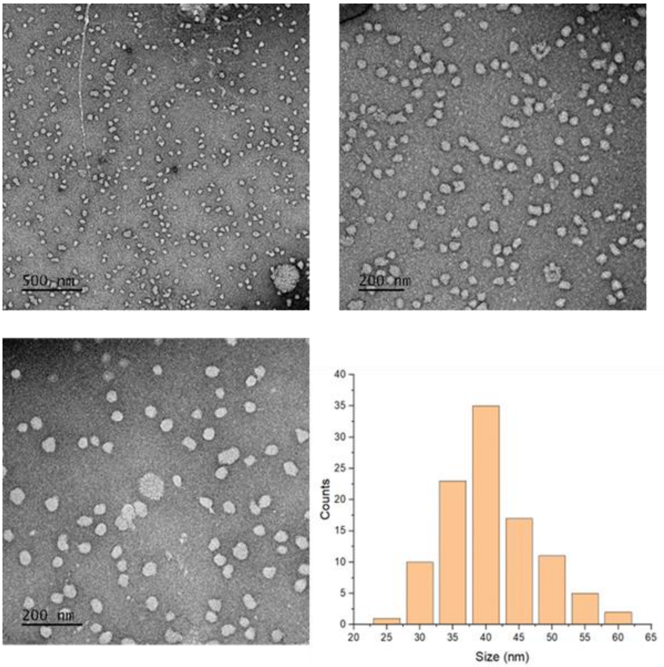

Figure 4.11: TEM images with negative stains and statistical analysis of NPs dimension.

UV-visible spectroscopy in solution with integrated sphere was exploited to quantify the amount of porphyrin inside the dialyzed particles. The UV-vis spectrum of the PtOEP inside the NPs perfectly match with the sensitizer in solution (**Figure 4.12**) and its concentration was calculated by interpolation of the maximum absorbance at 534 nm with the calibration curve registered in butyl acetate. The encapsulation efficiency resulted to be 10%, higher respect to the one of ZnTPP in the same alcoholic media.

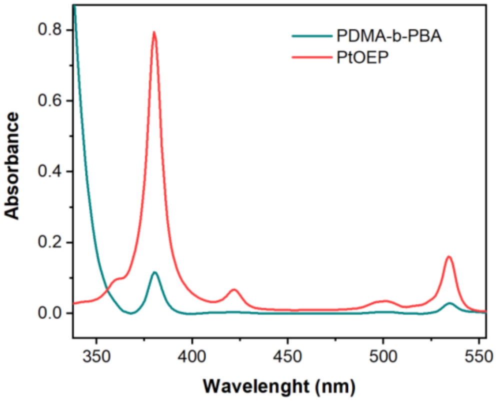

Figure 4.12: Comparison between absorption spectra of free PtOEP and PDMA-b-PBA nanoparticles dispersed in water (measured with an integrated sphere).

Diphenyl anthracene was then encapsulated into the nanoparticles core by addition of a solution of the emitter in DMC into the aqueous nanoparticles suspension, following an established method.[34] Time-resolved photoluminescence measurements provided insights about the donor-acceptor energy transfer efficiency (Φ_{ET}) process inside the NPs. The latter has been calculated as 1-(I/I_0), where I and I_0 are the intensity of the PtOEP emission in presence/absence of DPA respectively, and it results as high as 70%. **Figure 4.14a** reports the PL spectrum of the dual doped NP as a function of the excitation intensity at 532 nm. At the maximum excitation intensity employed the reference material doped with PdOEP only displays an intense red-PL upon excitation at 532 nm. This suggests that the synthetic strategy has been successful in incorporating enough DPA molecules to collect the energy absorbed by PtOEP quite efficiently. However, the upconverted emission at 430 nm is barely detectable with respect to the residual PtOEP phosphorescence at 645 nm thus suggesting a possible quenching of the ultrasensitive annihilator triplets by residual molecular oxygen. For this reason, the nanoparticles production was repeated, following the same synthetic protocol, but in a deoxygenated environment inside a glove box. The NP prepared in the glove box shows a more intense and clear upconverted emission (**Figure 4.14b**), thus indicating that the preparation in controlled atmosphere completely avoids molecular oxygen quenching. The Φ_{ET} is assessed as high as 60%, while the maximum UC quantum yield (QY) results in 10%.

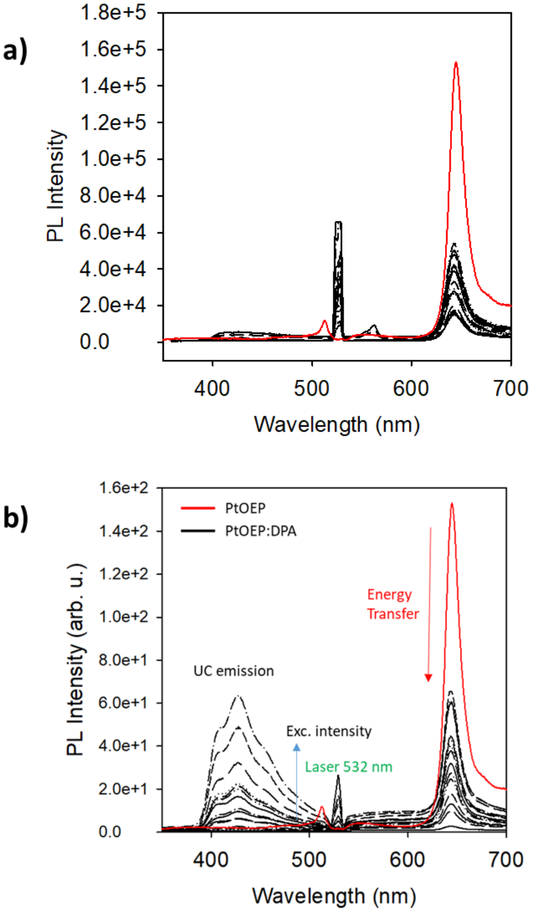

Figure 4.13: Photoluminescence spectra of DPA:PtOEP (50:1) doped NPs (a) degassed solvent and b) glove box photopolymerization) in EtOH/H_2O (70/30) solution under continuous wave 532 nm laser excitation as a function of the incident excitation intensity.

The red line marks the PL spectrum of PtOEP doped NP under 532 nm excitation at the maximum intensity employed.

This promising results is in between the maximum UC of the two dyes dissolved in low viscous media such as THF (23%) and in bulk polymers, (*i.e.* 0.2% for such as polystyrene), due to the very low diffusion coefficient of the two molecules. The higher yield respect to rigid polymer but lower yield respect to solution indicates that the soft-core NPs effectively work as confined system for increasing the efficiency of the UC in the solid systems but due to the still lower mobility respect to the solution the donor-acceptor energy transfer efficiency is not that efficient to allow the same QY. In fact, according to bimolecular nature of the TTA process, the UC emission intensity as function of the exaction intensity increase as the square of the excitation intensity (**Figure 4.15b**), indicating that we are far from the maximum efficiency excitation regime for the sensitized TTA in the NP environment. Additionally, the UC emission intensity decays as a single exponential function with a characteristic lifetime of τ_{uc} = 83.5 μs (**Figure 4.15a**). This implies that the DPA triplet exciton in the NP has a spontaneous decay time of $2\tau_{uc}$ = 167 μs, instead of 500 μs usually observed in literature, suggesting that the TTA process is slow.

Overall, the final 10% upconversion quantum yield of the nano-object is significantly enhanced with respect to the 0.2% of bulk polymer. The gap between this result and the maximum UC achievable in solution is in agreement with the lower mobility of dyes that does not allow fast ET and TTA due to the lower mobility and partial quenching of the annihilator triplets.

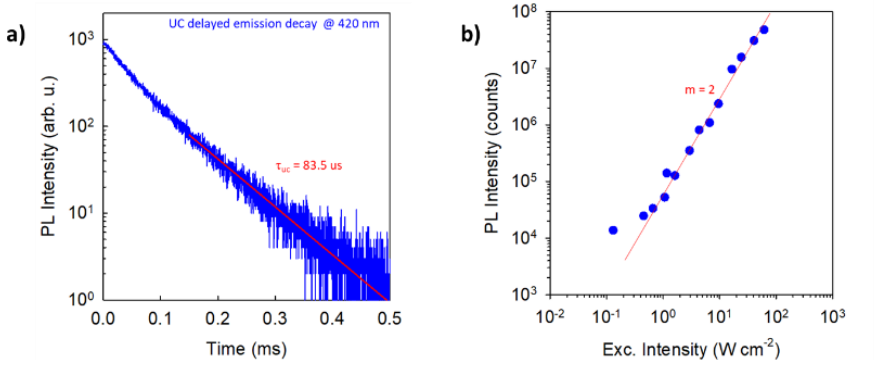

Figure 4.14: a) UC-PL intensity at 435 nm as a function of time of DPA:PtOEP (50:1) doped NPs (glove box photopolymerization) in EtOH/H_2O (70/30) solution under modulated 532 nm laser excitation (90 W cm^{-2}, 1 kHz, duty cycle 50% b) Integrated intensity of the UC emission of the same sample under continuous wave 532 nm laser excitation as a function of the incident excitation intensity. Solid line is a straight line with slope 2.

4.4 Conclusions

In conclusion, PET-RAFT polymerization using ZnTPP as a photocatalyst has been successfully used for the synthesis of hard shell soft core nanoparticles based on PDMA-b-PBA block copolymers. Very good control over the polymerization has been achieved maintaining low molecular weight dispersity and high livingness as demonstrated by the chain extension experiments. Alcoholic media with different water contents have been tested as solvents determining a linear relation between the water fraction and the monomer conversion of the second block which also influences the final particle's morphology, mostly spherical. The polymerization strategy has been simplified, avoiding the purification step of the solvophilic block, reducing the environmental impact of this process. In addition, reaction optimization is a non-time-consuming process due to high throughput synthesis setup, and produces minimum waste due to the possibility of exploiting low volumes. Finally, ZnTPP encapsulation during the self-assembly has been evaluated resulting in a remarkable 12% efficiency for EtOH and MeOH 90% dispersing media.

The concept just described has the ambition to be quite general in order to extend its applicability to a wide range of systems just by changing the chemical nature of monomers or the porphyrin/emitter pairs employed. In fact, this optimized procedure has been employed for the one-pot synthesis of nanoparticles for upconversion. In particular, the design of a soft PBA core is essential for increasing the donor/acceptor mobility, allowing for high yield in solid state. We demonstrated for the first time the efficiency of PtOEP as a photocatalyst for PET-RAFT and its direct encapsulation on the synthesized nanocarriers. The morphology of the final nano-object was consistent with the one obtained for ZnTPP in the same experimental conditions. Finally the upconversion efficiency has been confirmed by optical characterization, resulting in 10% efficiency. This result highlights the potential applicability of this easy, robust, and waste-minimization synthetic protocol.

Further optimization will be studied to increase the oxygen impermeability of the polymeric shell, achieving higher energy transfer efficiency. In particular, further implementation of the NPs structure can be achieved by the shell-crosslinking using post-polymerization modifications. Glycidyl methacrylate is a promising monomer thanks to the presence of an epoxidic functionality that can be crosslinked by using bifunctional linkers or can be exploited for the decoration of the particle surface.

4.5 References

[1] M. Holzinger, A. Le Goff, S. Cosnier, *Front. Chem.* **2014**, *2*, 1–10.

[2] F. Eisenreich, E. W. Meijer, A. R. A. Palmans, *Chem. - A Eur. J.* **2020**, *26*, 10355–10361.

[3] X. Hu, Y. Zhang, Z. Xie, X. Jing, A. Bellotti, Z. Gu, *Biomacromolecules* **2017**, *18*, 649–673.

[4] X. Wu, R. H. Guy, *J. Drug Deliv. Sci. Technol.* **2009**, *19*, 371–384.

[5] T. Singh, S. Shukla, P. Kumar, V. Wahla, V. K. Bajpai, *Front. Microbiol.* **2017**, *8*, 1–7.

[6] N. Li, A. Nikoubashman, A. Z. Panagiotopoulos, *Langmuir* **2019**, *35*, 3780–3789.

[7] G. Vaccaro, A. Bianchi, M. Mauri, S. Bonetti, F. Meinardi, A. Sanguineti, R. Simonutti, L. Beverina, *Chem. Commun.* **2013**, *49*, 8474–8476.

[8] A. Bianchi, M. Mauri, S. Bonetti, K. Koynov, M. Kappl, I. Lieberwirth, H. J. Butt, R. Simonutti, *Macromol. Rapid Commun.* **2014**, *35*, 1994–1999.

[9] K. Wang, Y. Wang, W. Zhang, *Polym. Chem.* **2017**, *8*, 6407–6415.

[10] G. Wang, M. Schmitt, Z. Wang, B. Lee, X. Pan, L. Fu, J. Yan, S. Li, G. Xie, M. R. Bockstaller, K. Matyjaszewski, *Macromolecules* **2016**, *49*, 8605–8615.

[11] K. Parkatzidis, M. Rolland, N. P. Truong, A. Anastasaki, *Polym. Chem.* **2021**, *12*, 5583–5588.

[12] G. Delaittre, M. Save, B. Charleux, *Macromol. Rapid Commun.* **2007**, *28*, 1528–1533.

[13] G. Delaittre, M. Save, M. Gaborieau, P. Castignolles, J. Rieger, B. Charleux, *Polym. Chem.* **2012**, *3*, 1526–1538.

[14] G. Delaittre, J. Nicolas, C. Lefay, M. Save, B. Charleux, *Soft Matter* **2006**, *2*, 223–231.

[15] M. Guerre, M. Semsarilar, F. Godiard, B. Améduri, V. Ladmiral, *Polym.*

Chem. **2017**, *8*, 1477–1487.

[16] S. Qu, R. Liu, W. Duan, W. Zhang, *Macromolecules* **2019**, *52*, 5168–5176.

[17] S. Sugihara, A. Blanazs, S. P. Armes, A. J. Ryan, A. L. Lewis, *J. Am. Chem. Soc.* **2011**, *133*, 15707–15713.

[18] X. Wang, Z. An, *Macromol. Rapid Commun.* **2019**, *40*, 1–14.

[19] M. J. Derry, L. A. Fielding, S. P. Armes, *Prog. Polym. Sci.* **2016**, *52*, 1–18.

[20] N. J. Warren, S. P. Armes, *J. Am. Chem. Soc.* **2014**, *136*, 10174–10185.

[21] O. Colombani, M. Ruppel, M. Burkhardt, M. Drechsler, M. Schumacher, M. Gradzielski, R. Schweins, A. H. E. Müller, *Macromolecules* **2007**, *40*, 4351–4362.

[22] S. L. Canning, G. N. Smith, S. P. Armes, *Macromolecules* **2016**, *49*, 1985–2001.

[23] L. P. D. Ratcliffe, A. Blanazs, C. N. Williams, S. L. Brown, S. P. Armes, *Polym. Chem.* **2014**, *5*, 3643–3655.

[24] X. Liu, M. Sun, J. Sun, J. Hu, Z. Wang, J. Guo, W. Gao, *J. Am. Chem. Soc.* **2018**, *140*, 10435–10438.

[25] S. L. Canning, G. N. Smith, S. P. Armes, *Macromolecules* **2016**, *49*, 1985–2001.

[26] A. Monguzzi, F. Bianchi, A. Bianchi, M. Mauri, R. Simonutti, R. Ruffo, R. Tubino, F. Meinardi, *Adv. Energy Mater.* **2013**, *3*, 680–686.

[27] G. Cheng, J. Perez-Mercader, *Chem* **2020**, *6*, 1160–1171.

[28] J. Chen, J. X. Zhao, *Sensors* **2012**, *12*, 2414–2435.

[29] M. J. Bennison, A. R. Collins, B. Zhang, R. C. Evans, *Macromolecules* **2021**, *54*, 5287–5303.

[30] H. Kouno, T. Ogawa, S. Amemori, P. Mahato, N. Yanai, N. Kimizuka, *Chem. Sci.* **2016**, *7*, 5224–5229.

[31] T. Dilbeck, K. Hanson, *J. Phys. Chem. Lett.* **2018**, *9*, 5810–5821.

[32] P. Bharmoria, N. Yanai, N. Kimizuka, *Gels* **2019**, *5*, 1–10.

[33] R. Vadrucci, A. Monguzzi, F. Saenz, B. D. Wilts, Y. C. Simon, C. Weder, *Adv. Mater.* **2017**, *29*, 1–8.

[34] A. Monguzzi, M. Frigoli, C. Larpent, R. Tubino, F. Meinardi, *Adv. Funct. Mater.* **2012**, *22*, 139–143.

[35] J. Rieger, W. Zhang, F. Stoffelbach, B. Charleux, *Macromolecules* **2010**, *43*, 6302–6310.

[36] K. Rybicka-Jasińska, T. Wdowik, K. Łuczak, A. J. Wierzba, O. Drapała, D. Gryko, *ACS Org. Inorg. Au* **2022**, *2*, 422–426.

[37] J. Jiao, J. He, M. Li, J. Yang, H. Yang, X. Wang, S. Yang, *Nanoscale* **2022**, 6373–6383.

[38] J. Pedrini, A. Monguzzi, *J. Photonics Energy* **2017**, *8*, 1.

[39] C. Wohnhaas, A. Turshatov, V. Mailänder, S. Lorenz, S. Baluschev, T. Miteva, K. Landfester, *Macromol. Biosci.* **2011**, *11*, 772–778.

[40] Q. Liu, B. Yin, T. Yang, Y. Yang, Z. Shen, P. Yao, F. Li, *J. Am. Chem. Soc.* **2013**, *135*, 5029–5037.

[41] J. Lu, Z. Liu, N. Pai, L. Jiang, U. Bach, A. N. Simonov, Y. B. Cheng, L. Spiccia, *Chempluschem* **2018**, *83*, 711–720.

[42] H. Tao, L. Xia, G. Chen, T. Zeng, X. Nie, Z. Zhang, Y. You, *Polymers (Basel).* **2019**, *11*, DOI 10.3390/polym11050892.

[43] J. Yeow, S. Shanmugam, N. Corrigan, R. P. Kuchel, J. Xu, C. Boyer, *Macromolecules* **2016**, *49*, 7277–7285.

[44] Z. Zhang, N. Corrigan, A. Bagheri, J. Jin, C. Boyer, *Angew. Chemie* **2019**, *131*, 18122–18131.

[45] J. Xu, S. Shanmugam, C. Fu, K. F. Aguey-Zinsou, C. Boyer, *J. Am. Chem. Soc.* **2016**, *138*, 3094–3106.

[46] S. Shanmugam, J. Xu, C. Boyer, *J. Am. Chem. Soc.* **2015**, *137*, 9174–9185.

[47] V. J. Cunningham, Y. Ning, S. P. Armes, O. M. Musa, *Polymer (Guildf).* **2016**, *106*, 189–199.

[48] S. P. Wen, J. G. Saunders, L. A. Fielding, *Polym. Chem.* **2020**, *11*, 3416–3426.

[49] E. R. Jones, M. Semsarilar, P. Wyman, M. Boerakker, S. P. Armes, *Polym. Chem.* **2016**, *7*, DOI 10.1039/c5py01795e.

[50] N. Zaquen, W. A. A. W. Azizi, J. Yeow, R. P. Kuchel, T. Junkers, P. B. Zetterlund, C. Boyer, *Polym. Chem.* **2019**, *10*, 2406–2414.

[51] R. Takahashi, S. Miwa, F. H. Sobotta, J. H. Lee, S. Fujii, N. Ohta, J. C. Brendel, K. Sakurai, *Polym. Chem.* **2020**, *11*, 1514–1524.

[52] D. Wang, V. L. Dimonie, E. David Sudol, M. S. El-Aasser, *J. Appl. Polym. Sci.* **2002**, *84*, 2692–2709.

[53] D. Neugebauer, K. Matyjaszewski, *Macromolecules* **2003**, *36*, 2598–2603.

[54] A. L. Stevens, N. K. Joshi, M. F. Paige, R. P. Steer, *J. Phys. Chem. B* **2017**, *121*, 11180–11188.

Chapter 5

Polymer/perovskite nanocomposite in one-step strategy *via* PET-RAFT polymerization

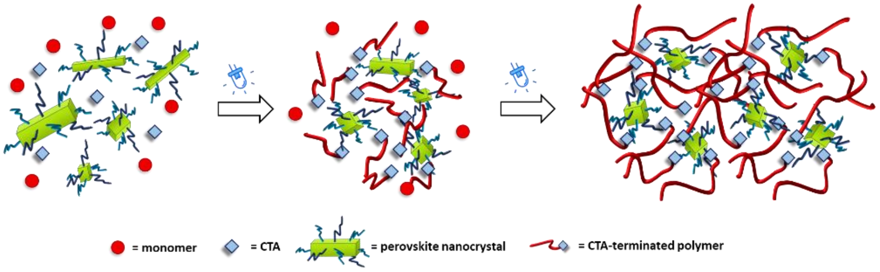

5.1 Introduction

Lead halide perovskites ($APbX_3$; where A = $CH_3NH_3^+$, $CH(NH_2)_2^+$, Cs and X = Cl, Br, I) nanocrystals (LHP-NCs) gained incredible attention in the last decades revolutionizing many technological applications.[1–6] The interest in such materials is due to their high absorption coefficient, long exciton diffusion lengths, and low exciton binding energies, together with their bright and narrow-band photoluminescence (PL) with tunable emission over the visible spectrum, and excellent photoluminescence quantum yield (PLQY) properties.[7–10] In particular, LHP-NCs are emerging as versatile candidates as efficient emitters for light management technologies, such as artificial lighting, display,[11] as well as bright scintillators for radiometric applications.[12,13] However, LHPs suffer from long-term instability issues and decomposition in the presence of moisture, oxygen, and thermal exposure, together with low processability, limiting their effectiveness for the potential applications.[14–17] For these reasons, polymers have been used to encapsulate the LHPs NCs, to improve their stability and processability and to enhance their optical properties by passivating charge traps.[18,19] Poly(methyl methacrylate) (PMMA) is a well-known commercial polymer with excellent characteristics for the fabrication of plastic nanocomposites owing its high glass transition temperature that provides mechanical stability, simple manufacturing, good optical properties, and radiation hardness.[13,20]

The current approaches for the fabrication of LHP-NCs/polymer composites relies mainly on three methods: (i) physical embedding of LHP-NCs into polymer matrix by solvent evaporation method,[21–23] (ii) direct synthesis of the LHP-NCs into polymer solution by thermal annealing,[24,25] and (iii) *in situ* polymerization of the polymer matrix in the presence of the NCs.[26] However, all such techniques present some disadvantages: the solvent evaporation method is incompatible with large-scale production, employs toxic solvents, and results in inhomogeneous composites. The direct synthesis of LHP into polymer solution results in uncontrolled NCs size and aggregation, affecting the optical quality. Finally, the *in situ* polymerization is the most appealing for the production of bulk nanocomposites, but it relies on the use of radical photo-initiators (*i.e.* 2,2-dimethoxy-2-phenylacetophenone), activated under UV illumination which limits the maximum NCs loadings due to competitive light absorption by the NCs.[26] Moreover, photo-initiators might damage the photophysical properties of the NCs,[27] resulting in lower PLQY.[28] Both Lalevée[29] and Tan[30] groups demonstrated that the uses of external photo-initiators could be avoided exploiting the perovskite NCs as initiator for free radical polymerization (FRP). This method resulted in improved optical properties of the nanocomposites and good dispersibility of the NCs at the expense of low polymerization conversion and NCs loading. The limitations of perovskite-initiated FRP in terms of monomer conversion and NCs loading are interconnected and related to the uncontrolled nature of the polymerization technique. In fact, the termination of the polymer chains are negatively affected by high initiator amounts. On the other hand, the more controlled reversible deactivation radical polymerization (RDRP) such as RAFT allows for a constant radical concentration during the polymerization, independent of the initiator amount, and would allow to obtain high LHP-NCs loadings. Prelaminar work of Egap et al,[31] followed by the work of Gao et al,[32,33] show the remarkable ability of $CsPbX_3$ (X = Br, Cl, I) of acting as photoinitiators in control PET-RAFT (photo-induced electron/energy transfer-reversible activation chain-transfer) polymerization. Higher polymerization performance with respect to FRP were obtained for acrylates, but with limitation in more activated monomers (*i.e.* methyl methacrylate (MMA)), which are more interesting for nanocomposites production.

To date, low polymerization yield, together with the low LHP-NCs loadings, shared by the majority of the *in situ* polymerization techniques, represent an open challenge for the synthesis of bulk LHP-NCs polymer composites. Herein, we aim to contribute to this field by introducing an efficient protocol for the production of $CsPbBr_3$/PMMA nanocomposite in one-step procedure by perovskite-initiated PET-RAFT polymerization. The composites are obtained at room temperature, in the presence of oxygen and by avoiding the production of toxic wastes containing heavy metal ions due to very high polymerization yield. We report a monomer conversion of methyl methacrylate (MMA) close to 90% with very high LHP-NCs loadings (up to 7%) and a positive evolution of the NCs immersed in the polymer matrix, increasing their optical properties (PLQY up to 90%). The $CsPbBr_3$ NCs plays a dual role, first acting as a photocatalyst for the control polymerization of MMA, and then as the inorganic active compound of the nanocomposite by direct encapsulation in the newly formed polymeric matrix.

5.2 Materials and Methods

5.2.1.Materials

Cesium carbonate (Cs_2CO_3, 99%) and lead(II) bromide ($PbBr_2$, 99.99%) were purchased from Fluorochem. Propionic acid (PA, >99.5%) were purchased from Merck. Heptane (Hept, Gpr rectapur, 99.8%) and isopropanol (iPrOH, HiPerSolv chromanorm for HPLC >98%) were purchased from VWR. Toluene, tetrahydrofuran (THF), deuterated chloroform ($CDCl_3$)) were purchased from Sigma Aldrich and used as received. Oleylamine (OAm, 80%−90%) was purchased from Acros Organic. Isopropanol was dried over CaH_2 for a week and then distilled before use. Methyl methacrylate (MMA) was purchased from Sigma and purified in basic alumina column before use to remove the inhibitor. 2-cyanoisopropyl dithiobenzoate (CPDB) was purchased from TCI. All other chemicals were used without any further purification and stored in a dryer. A turboemulsifier homogenizer was bought from IKA and is composed of a motor group T25/T50 digital Ultra Turrax + dispersing tool with codes S25N-25G and S50N-G45 M for volumes, respectively, up to 2 L and above 2 L. Blue LED light ($\lambda = 460$ nm) was purchased in strips and accommodate in circular shape in a home-made photoreactor with a light intensity of 10 mW/cm^2.

5.2.2. Experimental procedures

Synthesis of $CsPbBr_3$ NCs with Turboemulsifier

A solution containing the Cs^+ precursor (from here on defined as solution A) is prepared by reacting Cs_2CO_3 (6 mmol, 1.95 g) with PA (6 mL, 79.8 mmol) and then diluting the resulting solution with 3600 mL of Hept/iPrOH 2:1 vol mixture. A solution containing the Pb^{2+} precursor (from here on defined as solution B) is prepared by dissolving $PbBr_2$ (60 mmol, 22 g) and TBAB (60 mmol, 19.3 g) in a mixture of OAm (540 mmol, 177.6 mL), PA (540 mmol, 40.2 mL), and iPrOH (60 mL) at 80 °C. After the complete dissolution of the precursors, the mixture is cooled to room temperature (no precipitation observed over 8 h). Solution A is put under stirring with a turboemulsifier homogenizer (15k RPM) in a 5 L beaker, and then, solution B is swiftly poured. The mixture is further homogenized for 30 s to give a clear yellow solution. Upon dilution with 1.8 L of iPrOH, a fine precipitate forms, that is collected by centrifugation at 4500 rpm for 2 min. The bright yellow solid is dried under reduced pressure until constant weight (8 g) and stored in a glovebox under argon atmosphere. No further purification nor size selection steps are performed.

General PET-RAFT polymerization of MMA using 2-cyano-2-propyl dithiobenzoate as a RAFT agent (PMMA-DTB).

2.77 mg of 2-cyanoprop-2-yl dithiobenzoate (0.0125 mmol, 1 eq) and 1.067 mL of MMA (1 g, 10 mmol, 800 eq) were added in a 8 mL glass vial. Subsequently, 25 µL of a $CsPbBr_3$ toluene solution were added from a stock solution 20 mg/mL (corresponding to the 0.05 % wt catalyst loading experiments), and the vial was sealed with a rubber septum, prior to deoxygenation by nitrogen bubbling for 10 min. Polymerization was conducted under blue LED irradiation at room temperature for 24 h. The solution was sampled under a nitrogen blanket for GPC and NMR analysis. The final material was stored at 4 °C in oxygen atmosphere.

For the experiments at higher PC loading the $CsPbBr_3$ NCs were weighted and added into the reactor and the solution was left under stirring for the first 3 hours to help homogenization. The magnetic stirrer was then removed to allow the formation of the solid disk. The polymerization in this case was conducted in the presence of oxygen by the addition of 5.6 µL of limonene (4.72 mg, 0.03 mmol, 2.77 eq).

Analysis of ^{1}H NMR during polymerization

Polymerization conversions were determined by ^{1}H NMR, comparing the monomer vinyl signals at 5.5 and 6.1 ppm designed as I_M to the polymer backbone -CH_3 signals between 0.8 and 1ppm designed as I_P according to the following formula:

$$conv\,\% = \frac{(I_P)/3}{(I_P + I_M)} * 100$$

Evaluation of interaction between CPDB and $CsPbBr_3$

The $CsPbBr_3$/CPDB (donor/acceptor) interaction has been analyzed by time-resolved PL experiments. Toluene dispersion of $CsPbBr_3$ nanocrystals were prepared, maintaining the donor concentration constant to 1 mg/mL. To the latter constant volumes (0.05 mL) of a CPDB solution in toluene at various concentrations were added. The solution was transferred into a glass cuvette with optical path length 1mm for the optical measurements. The typical donor-acceptor distance has been calculated considering that each perovskite nanocrystals is embedded into a pertinent volume of CPDB in solution. The average volume occupied by CPDB in solution, pertinent to the $CsPbBr_3$ NCs (V_p), is estimated by the number of molecules per unit volume at a given concentration. The maximum distance between two species is determined considering the V_p with the approximation that each CPDB is located at the center of a sphere with radius R.

$$V_p = \frac{1}{[CPDB] \cdot N_A} \qquad (5.1) \qquad\qquad R = \sqrt[3]{\frac{3V_p}{4\pi}} \qquad (5.2)$$

The average distance <d> between CPDB and $CsPbBr_3$ have been calculated by weighting the donor-acceptor distances (R) respect to the probability of the nanocrystals to be in a particular fraction of a spherical shell with radius r+dr.

$$< d \geq = \frac{\int_0^R r\,4\pi r^2 \cdot rdr}{\frac{4}{3}\pi R^3} \qquad (5.3)$$

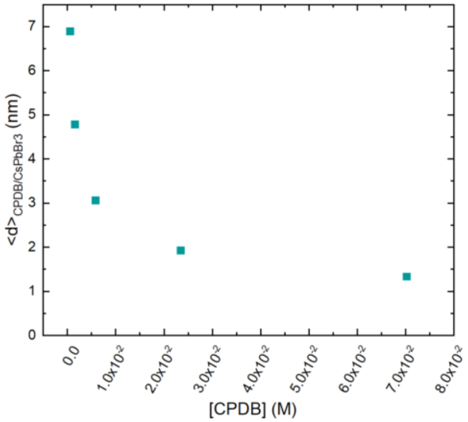

Figure 5.1: Average distance between CPDB and $CsPbBr_3$ NCs in toluene solution as a function of the CPDB concentration.

5.3 Results and discussion

5.3.1.Synthesis of Perovskite nanocrystals

To initiate our study, $CsPbBr_3$ NCs were synthesized *via* a turbo-emulsified process at room temperature as reported in the method section, following a recent procedure.[34] This technique allows for the large-scale synthesis of NCs (up to 8g) in a single batch, and the recycling of the waste generated during the NCs production, which is highly appealing for the synthesis of high-loaded nanocomposites in large quantity. The pristine NCs were determined to be an ensemble of polydisperse nanocrystals, resembling a rods-bricks morphology, with cubic phase (**Figure 5.2**), consistently with previous report.[26] The NCs have an average particle size of 14 ± 2 nm and thickness of 4 ± 1 nm, determined both *via* calculation[35] and transmission electron microscope (TEM). The PLQY of the NCs in solution was measured to be 44%, reaching up to 90% in the composites, as described in more detail in the following sections (*vide infra*).

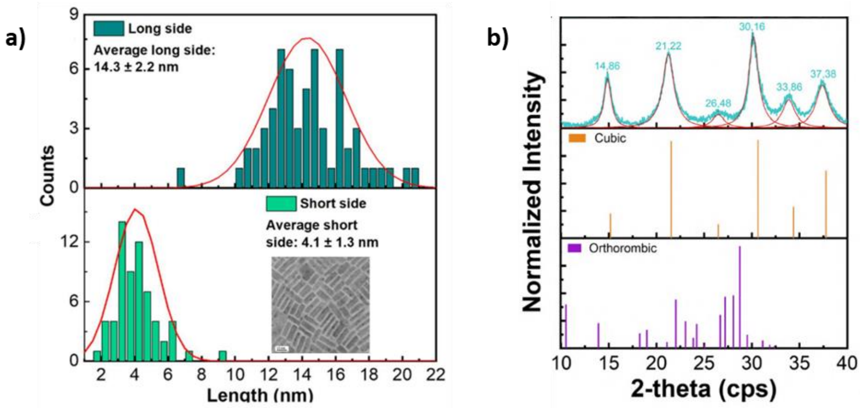

Figure 5.2: a) Transmission electron microscopy (TEM) image of the pristine NCs and the corresponding distributions of dimension of long and short side, fitted with a gaussian curve. b) Powder X-ray diffractograms. Lorentzian fit and the 2-theta degrees of the main peaks are reported. $CsPbBr_3$ cubic and orthorhombic phases diffractograms are also reported for comparison (respectively PDF Card No.: 01-084-0464 and PDF Card No.: 01-074-2251).

5.3.2. Kinetics and performance of PK initiated PET-RAFT

Polymerization of MMA was conducted with 2-cyano-2-propyl benzodithioate (CPDB) as the CTA (M/CTA = 800) in semi-bulk condition with a very low amount of photocatalytic NCs (0.05% wt relative to the monomer). Nevertheless, the synthetized $CsPbBr_3$ NCs show outstanding performances in PET-RAFT polymerization of MMA, allowing a conversions of 87.1% (**Table 5.1,** entry 4), with the consequent one-pot formation of $CsPbBr_3$-PMMA disks after 24 hours under irradiation, without any purification steps.

The progress of the polymerization over time was monitored by ^{1}H NMR of the reaction crude. Linear increases of conversion over time identify a pseudo first-order kinetic (**Figure 5.2b**) confirming that the polymerization follows RDRP behavior, as expected for PET-RAFT mechanism. It is worth noting that negligible conversion was obtained in the absence of light, whereas when the polymerization was performed in the presence of CTA but not $CsPbBr_3$ PMMA was obtained but with drastically lower conversion. Finally, in presence of $CsPbBr_3$ NCs without the CTA, the polymerization produces very high molecular weight PMMA but in uncontrolled fashion, as demonstrated by the high polydispersity of the molecular weights (Đ > 2), and low conversion (**Table 5.1**, entries 1-3). These results are in accordance with previous reports on perovskite-initiate FRP and the photoiniferter properties of the CTA.[30,36]

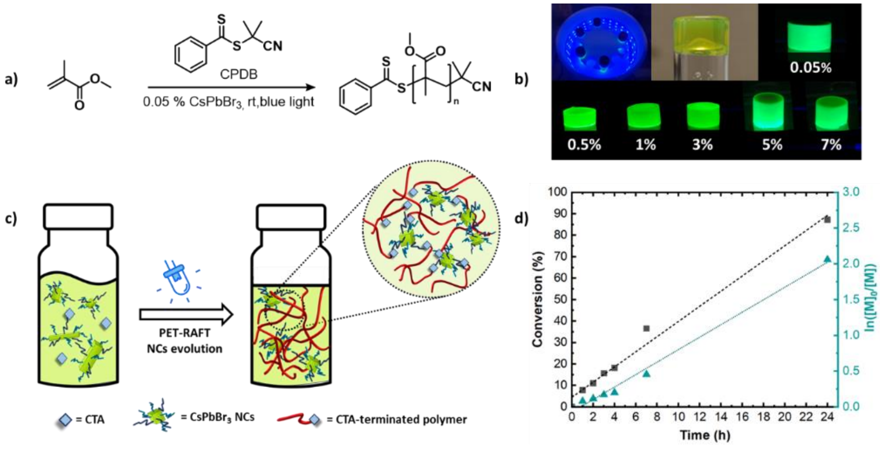

Figure 5.3: a) Reaction scheme of PET-RAFT polymerization of MMA under blue irradiation with CPDB as chain transfer agent. b) Picture of the reaction set up and the final solid sample after 24 hours under irradiation. c) cartoon of the polymerization reaction with the consequent formation of the polymeric matrix and the embedded NCs. d) Kinetic of the polymerization (0.05 % wt of PC) showing a linear conversion of the monomer over time with a pseudo first-order kinetic.

Table 5.1: PET-RAFT polymerization of methyl methacrylate (MMA) using $CsPbBr_3$ in toluene as photocatalyst. Reactions were conducted under 460 nm blue light, at room temperature for 24 hours. *entry 1 experiment was performed without light irradiation. [a] Monomer conversion (α) calculated with NMR analysis. [b] Molecular weight and dispersity were obtained by GPC measures.

Entry	[M]/[CPDB]	PC loading (wt %)	α (%)[a]	$M_{n,GPC}$[b]	$M_{n,theo}$	Đ[b]
1*	800	0.05	--	--		--
2	800	0	18.2	21 800	14 800	1.12
3	0	0.05	37.5	330 000	--	>2
4	800	0.05	87.1	81 000	70 000	1.3
5	400	0.05	87.0	39 000	35 000	1.24
6	200	0.05	89.2	24 900	18 050	1.16
7	100	0.05	88.8	12 800	9 200	1.12
8	800	0.5	87.6	73 000	70 700	1.28
9	800	1	88.7	83 000	71 500	1.29
10	800	3	87.9	80 000	70 600	1.32
11	800	5	85.0	91 200	69 200	1.39
12	800	7	78.8	93 400	62 900	1.43

Moreover, the polymerization was repeated by decreasing the monomer to CTA ratio (from 800 to 100), maintaining the $CsPbBr_3$ concentration constant (**Table 5.1**, entries 5-7). In all cases, a high yield, close to 90%, was obtained with increased control over the polymerization ($1.12 < D < 1.3$). Importantly, the presence of the CTA is not detrimental to the $CsPbBr_3$ perovskites stability as highlighted **Figure 5.4** by the lifetime analysis (consistent with the value of pristine crystals). However, high CTA concentrations (M/CTA = 100) decreases the optical properties of the final nanocomposites due to an overlap of the week absorption of 2-cyano-2-propyl benzodithioate at 525 nm correlated to forbidden n-π^* transition of the thiocarbonyl bond. Overall, low amount of CTA allows for very efficient one-pot synthesis of the polymeric nanocomposites with high yield, and preserving the perovskite optical properties.

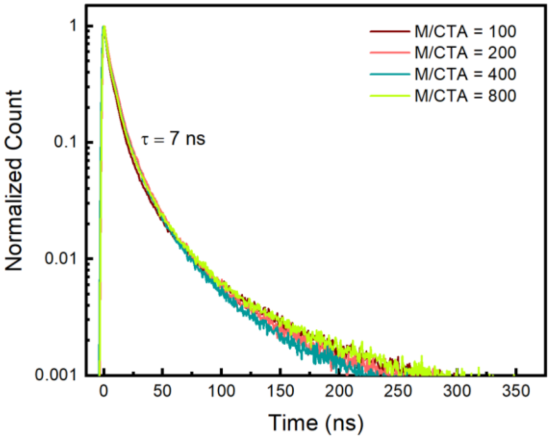

Figure 5.4: TRPL analysis of PMMA-$CsPbBr_3$ nanocomposites after the polymerization with increasing M/CTA ratio.

Additionally, PET-RAFT polymerization offers intriguing advantages for the production of high-loaded LHP-NCs/polymer nanocomposites. The amount of initiator does not affect the polymerization yield in RDRP, allowing for the one-step synthesis of bulk composites with high amounts of NCs as a photocatalyst. Moreover, the activation of the CTA by the excited perovskite NCs occurs at the catalyst interface.[37] Lewis bases, and in particular sulfur-based compounds (*i.e.* thiocarbonylthio-containing CTAs), exhibit strong electron-donating properties which make them perfect candidates for the coordination with the electron-deficient Pb atoms,[38] facilitating the PET process (**Figure 5.5a**), and ensuring high homogeneity of the NCs embedded in the polymer matrix.

The effectiveness of PET-RAFT polymerization to produce high-loaded nanocomposites was demonstrated by increasing the photocatalyst concentration up to 7 wt% with respect to the monomer as shown in **Table 5.1**, entries 8-12, and corroborated by thermogravimetric analysis (**Figure 5.5a**). Impressively, our method resulted in the one-pot production solid disks without affecting the monomer conversion even at high NCs loadings (**Figure 5.3b**). TEM analysis of various slices of the material at different dept confirmed the excellent dispersibility of the embedded nanocrystals into the polymer matrix (**Figure 5.5b**), supporting the hypothesis of an interaction of the CTA with the NCs surface as the polymerization proceed. The high mechanical stability of the PMMA is not affected by the presence of increased NCs loading, as demonstrated by compression test (**Figure 5.5b**), coherent with the high glass transition temperature (116°C, **Figure 5.5c**) characteristic of PMMA. Finally, the crystalline structure of the $CsPbBr_3$ NCs is preserved during the synthesis, maintaining a cubic phase (**Figure 5.5d**). Noteworthy, for improving the processability and scalability of our methodology the polymerizations were conducted in an oxygenated environment, by the addition of limonene as an oxygen quencher, further simplifying the synthetic procedure. The unreacted monomer has been removed simply by evaporation at room temperature and atmospheric pressure, resulting in complete absence of the monomer as demonstrated by solid state NMR (**Figure 5.5e**).

Remarkably, the polymerization leads to a positive evolution of the native NCs from a polydisperse mixture to a more uniform ensemble. The improved optical properties of the nanocomposite come from the efficient passivation of the $CsPbBr_3$ surface as demonstrated by the increases of the

PLQY to 70%, in case of 0.05% (entry 4) loading, and 90% for the 0.5% (entry 8).

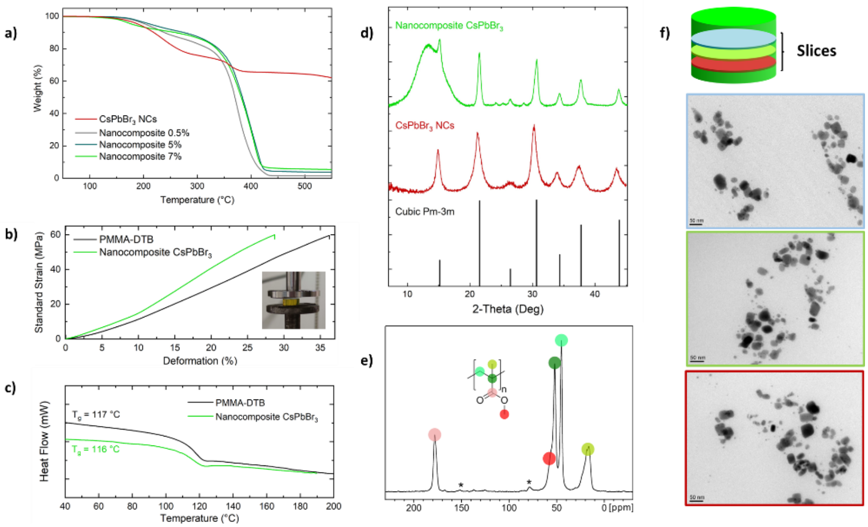

Figure 5.5: a) TGA analysis of the nanocomposites with 0.5, 5, and 7% loadings, compared to the native NCs (red line). The weight loss in the native NCs is attributed to the ligand surface coverage. b) Compression test and c) DSC measurements of the nanocomposite material (green line) compared to PMMA synthetized by RAFT polymerization with the same chain length and DTB as the CTA (black line). d) Powder X-ray diffraction patterns of the nanocomposites with 7% of embedded NCs (top, green line), the native NCs (middle, red line) and the calculated PXRD pattern for cubic $CsPbBr_3$. e) ^{13}C Cross Polarization Magic Angle Spinning (CPMAS) spectrum of the nanocomposite with 7% loading, showing no peaks in the alkene region (120-150 ppm).* refers to spinning sidebands. f) TEM micrographs of three different 70 nm thin nanocomposite section obtained from entry 11, Table 1 (0.5 cm thick).

5.3.3. Mechanistic evaluation of $CsPbBr_3$ initiated PET-RAFT

For a more deep understanding of these results, investigation of the main mechanistic aspects, which differentiate perovskite-initiated PET-RAFT polymerization with respect to common FRP, have been taken into account. Initiation of PET-RAFT polymerization is driven by the PET process from the excited photocatalyst to the CTA, causing the C-S bond fragmentation.

In heterogeneous catalysis, the process occurs to the catalyst interface and the CTA/PC interaction is of crucial importance. The polymerization has been followed step by step by time-resolved photoluminescence (TRPL) measurements as shown in **Figure 5.6**, where two distinct regimes can be observed as the polymerization proceeds.

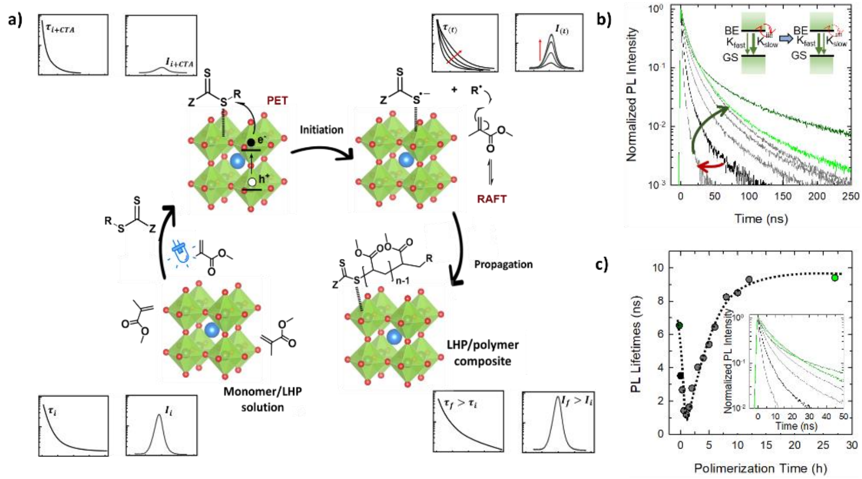

Figure 5.6: a) Reaction scheme of the $CsPbBr_3$-initiated polymerization step-by-step showing the graphic representation of the lifetime and PL intensity associated whit each step. b) Time-resolved PL spectra c) lifetime plot of the polymerization kinetic. Reactions were conducted at room temperature, under blue irradiation with 0.05% catalyst loading and [M]/[CTA]=800.

Initially, the PL and life time of nanocrystals in MMA follows a multi-exponential decay with a long tail due to the presence of traps that decrease the optical performance of the NCs. The introduction of the CTA into the reactor quenches the lifetime, in line with the introduction of the new efficient channel for the PET process to occur, initiating the reaction. As the polymerization progresses, there is a recovery of the PL and lifetime. Ultimately, the crystals embedded in the polymeric matrix (after 24 h) exhibit a slower excitonic component and a less pronounced tailing, which is the spectral signature of bromine vacancy passivation, in accordance with the increased PLQY.

Additionally, as the polymerization proceeds, shifting and shrinking of the PL curve, as well as the absorption edge are a further confirmation of the evolution from a more various size population to a homogeneous ensemble of NCs as already observed in FRP.[26] The absorbance profile attributable to PK does not vary over time but the absorption of the CTA associated to the C=S n-π* transition undergoes rapid blue shift after the first 10 minutes and remains unvaried thereafter (**Figure 5.7**). This period correspond with the so-called initiation period in which the CTA is activate into its single monomer adducted.[39–41] Additionally, the absorbance of this peak decreases, indicating that the extinction coefficient of the monomer adduct is lower, which is advantageous for the formation of the nanocomposites because of a lower, if any, overlap with the nanocrystals emission.

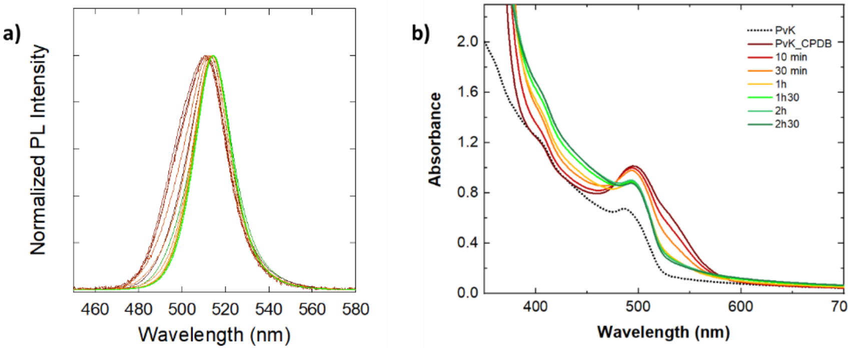

Figure 5.7: a) Normalized PL intensity at various time during the polymerization. b) UV-vis absorption spectra of the reaction mixture at increasing time. The dot line indicate perovskite (PvK) nanocrystals in MMA without the CTA and the red line (PvK_CPDB) is the mixture after the addition of CPDB previous irradiation. Reaction were conducted at room temperature, under blue irradiation with 0.05% catalyst loading and [M]/[CTA]=800.

5.4 Conclusions

In conclusion, in the present work we introduced the uses of PET-RFAT technology as an efficient polymerization technique for the synthesis of $CsPbBr_3$/PMMA nanocomposites in a one-pot one-step fashion. This method allowed for high reaction yield (around 90%) of MMA combined with a positive evolution of the NCs into a uniform ensemble, enhancing the optical properties of the final material (PLQY up to 90%). Moreover, the control character of PET-RAFT polymerization is an additional advantage for the synthesis of high-loaded composites maintaining high polymerization yield and NCs compatibility with the polymer matrix. The RDRP character of the polymerization, in combination with the oxygen tolerance of the technique and the multi-grams scale protocol for the synthesis of the perovskite NCs open possibility for the large scale production of the nanocomposites. Not less importantly, the development of this methodology allowed for a more deep mechanism understanding of the perovskite-initiate process.

More studies are now under investigation in terms of NCs/CTA interaction and applicability of the nanocomposites as plastic scintillators. Good results have been already obtained with a linear increase of the radioluminescence with respect to the perovskite concentrations.

5.5 References

[1] H. Huang, L. Polavarapu, J. A. Sichert, A. S. Susha, A. S. Urban, A. L. Rogach, *NPG Asia Mater.* **2016**, *8*, DOI 10.1038/am.2016.167.

[2] S. Arya, P. Mahajan, R. Gupta, R. Srivastava, N. kumar Tailor, S. Satapathi, R. R. Sumathi, R. Datt, V. Gupta, *Prog. Solid State Chem.* **2020**, *60*, 100286.

[3] L. Zhang, L. Mei, K. Wang, Y. Lv, S. Zhang, Y. Lian, X. Liu, Z. Ma, G. Xiao, Q. Liu, S. Zhai, S. Zhang, G. Liu, L. Yuan, B. Guo, Z. Chen, K. Wei, A. Liu, S. Yue, G. Niu, X. Pan, J. Sun, Y. Hua, W. Q. Wu, D. Di, B. Zhao, J. Tian, Z. Wang, Y. Yang, L. Chu, M. Yuan, H. Zeng, H. L. Yip, K. Yan, W. Xu, L. Zhu, W. Zhang, G. Xing, F. Gao, L. Ding, *Advances in the Application of Perovskite Materials*, Springer Nature Singapore, **2023**.

[4] K. S. Schanze, P. V. Kamat, P. Yang, J. Bisquert, *ACS Energy Lett.* **2020**, *5*, 2602–2604.

[5] R. J. Sutton, G. E. Eperon, L. Miranda, E. S. Parrott, B. A. Kamino, J. B. Patel, M. T. Hörantner, M. B. Johnston, A. A. Haghighirad, D. T. Moore, H. J. Snaith, *Adv. Energy Mater.* **2016**, *6*, 1–6.

[6] C. R. Kalaiselvi, N. Muthukumarasamy, D. Velauthapillai, M. Kang, T. S. Senthil, *Mater. Lett.* **2018**, *219*, 198–200.

[7] M. Righetto, D. Meggiolaro, A. Rizzo, R. Sorrentino, Z. He, G. Meneghesso, T. C. Sum, T. Gatti, F. Lamberti, *Prog. Mater. Sci.* **2020**, *110*, 100639.

[8] J. Shamsi, A. S. Urban, M. Imran, L. De Trizio, L. Manna, *Chem. Rev.* **2019**, *119*, 3296–3348.

[9] Q. A. Akkerman, V. D'Innocenzo, S. Accornero, A. Scarpellini, A. Petrozza, M. Prato, L. Manna, *J. Am. Chem. Soc.* **2015**, *137*, 10276–10281.

[10] Y. F. Makableh, R. Al-Abed, G. Aljaiuossi, *J. Mater. Sci. Mater. Electron.* **2021**, *32*, 7106–7122.

[11] K. Ji, M. Anaya, A. Abfalterer, S. D. Stranks, *Adv. Opt. Mater.* **2021**, *9*,

DOI 10.1002/adom.202002128.

[12] C. Dujardin, E. Auffray, E. Bourret-Courchesne, P. Dorenbos, P. Lecoq, M. Nikl, A. N. Vasil'Ev, A. Yoshikawa, R. Y. Zhu, *IEEE Trans. Nucl. Sci.* **2018**, *65*, 1977–1997.

[13] M. Gandini, I. Villa, M. Beretta, C. Gotti, M. Imran, F. Carulli, E. Fantuzzi, M. Sassi, M. Zaffalon, C. Brofferio, L. Manna, L. Beverina, A. Vedda, M. Fasoli, L. Gironi, S. Brovelli, *Nat. Nanotechnol.* **2020**, *15*, 462–468.

[14] M. Wu, N. Haji Ladi, Z. Yi, H. Li, Y. Shen, M. Wang, *Energy Technol.* **2020**, *8*, 1–12.

[15] X. Zhao, N. G. Park, *Photonics* **2015**, *2*, 1139–1151.

[16] B. R. Jheng, P. T. Chiu, S. H. Yang, Y. L. Tong, *Sci. Rep.* **2022**, *12*, 1–13.

[17] T. A. Berhe, W. N. Su, C. H. Chen, C. J. Pan, J. H. Cheng, H. M. Chen, M. C. Tsai, L. Y. Chen, A. A. Dubale, B. J. Hwang, *Energy Environ. Sci.* **2016**, *9*, 323–356.

[18] S. Liang, M. Zhang, G. M. Biesold, W. Choi, Y. He, Z. Li, D. Shen, Z. Lin, *Adv. Mater.* **2021**, *33*, 1–36.

[19] D. Yang, X. Li, H. Zeng, *Adv. Mater. Interfaces* **2018**, *5*, 1–13.

[20] P. G. Papagiorgis, A. Manoli, A. Alexiou, P. Karacosta, X. Karagiorgis, G. Papaparaskeva, C. Bernasconi, M. I. Bodnarchuk, M. V. Kovalenko, T. Krasia-Christoforou, G. Itskos, *Front. Chem.* **2019**, *7*, 1–12.

[21] K. Děcká, F. Pagano, I. Frank, N. Kratochwil, E. Mihóková, E. Auffray, V. Čuba, *J. Mater. Chem. C* **2022**, *10*, 12836–12843.

[22] L. Zhao, Y. W. Yeh, N. L. Tran, F. Wu, Z. Xiao, R. A. Kerner, Y. L. Lin, G. D. Scholes, N. Yao, B. P. Rand, *ACS Nano* **2017**, *11*, 3957–3964.

[23] S. N. Raja, Y. Bekenstein, M. A. Koc, S. Fischer, D. Zhang, L. Lin, R. O. Ritchie, P. Yang, A. P. Alivisatos, *ACS Appl. Mater. Interfaces* **2016**, *8*, 35523–35533.

[24] H. Liao, S. Guo, S. Cao, L. Wang, F. Gao, Z. Yang, J. Zheng, W. Yang,

Adv. Opt. Mater. **2018**, *6*, DOI 10.1002/adom.201800346.

[25] M. Meyns, M. Perálvarez, A. Heuer-Jungemann, W. Hertog, M. Ibáñez, R. Nafria, A. Genç, J. Arbiol, M. V. Kovalenko, J. Carreras, A. Cabot, A. G. Kanaras, *ACS Appl. Mater. Interfaces* **2016**, *8*, 19579–19586.

[26] A. Erroi, S. Mecca, M. L. Zaffalon, I. Frank, F. Carulli, A. Cemmi, I. Di Sarcina, D. Debellis, F. Rossi, F. Cova, K. Pauwels, M. Mauri, J. Perego, V. Pinchetti, A. Comotti, F. Meinardi, A. Vedda, E. Auffray, L. Beverina, S. Brovelli, **2023**, DOI 10.1021/acsenergylett.3c01396.

[27] X. Peng, L. Hu, X. Sun, Y. Lu, D. Chu, P. Xiao, *ACS Appl. Nano Mater.* **2023**, *6*, 646–655.

[28] J. Wu, J. Tong, Y. Gao, A. Wang, T. Zhang, H. Tan, S. Nie, Z. Deng, *Angew. Chemie - Int. Ed.* **2020**, *59*, 7738–7742.

[29] H. Mokbel, F. Dumur, B. Raveau, F. Morlet-Savary, C. Simonnet-Jégat, D. Gigmes, J. Toufaily, T. Hamieh, J. P. Fouassier, J. Lalevée, *Tetrahedron* **2016**, *72*, 7686–7690.

[30] Y. C. Wong, J. De Andrew Ng, Z. K. Tan, *Adv. Mater.* **2018**, *30*, DOI 10.1002/adma.201800774.

[31] Y. Zhu, Y. Liu, K. A. Miller, H. Zhu, E. Egap, *ACS Macro Lett.* **2020**, *9*, 725–730.

[32] X. Jin, K. Ma, J. Chakkamalayath, J. Morsby, H. Gao, *ACS Energy Lett.* **2022**, *7*, 610–616.

[33] X. Jin, K. Ma, H. Gao, *J. Am. Chem. Soc.* **2022**, *144*, 20411–20420.

[34] S. Mecca, F. Pallini, V. Pinchetti, A. Erroi, A. Fappani, F. Rossi, S. Mattiello, G. M. Vanacore, S. Brovelli, L. Beverina, *ACS Appl. Nano Mater.* **2023**, *6*, 9436–9443.

[35] G. Di Liberto, O. Fatale, G. Pacchioni, *Phys. Chem. Chem. Phys.* **2021**, *23*, 3031–3040.

[36] M. Hartlieb, *Macromol. Rapid Commun.* **2022**, *43*, DOI

10.1002/marc.202100514.

[37] V. Bellotti, C. Daldossi, D. Perilli, M. D. Arienzo, M. Stredansky, C. Di Valentin, R. Simonutti, *J. Catal.* **2023**, DOI 10.1016/j.jcat.2023.07.015.

[38] M. P. U. Haris, E. Ruiz, S. Kazim, S. Ahmad, *Cell Reports Phys. Sci.* **2023**, *4*, 101516.

[39] J. B. McLeary, J. M. McKenzie, M. P. Tonge, R. D. Sanderson, B. Klumperman, *Chem. Commun.* **2004**, *6*, 1950–1951.

[40] L. Lu, H. Zhang, N. Yang, Y. Cai, *Macromolecules* **2006**, *39*, 3770–3776.

[41] S. Nozari, K. Tauer, A. M. I. Ali, *Macromolecules* **2005**, *38*, 10449–10454.

Chapter 6

Chemical Recycling via PET-RAFT Controlled Radical Depolymerization

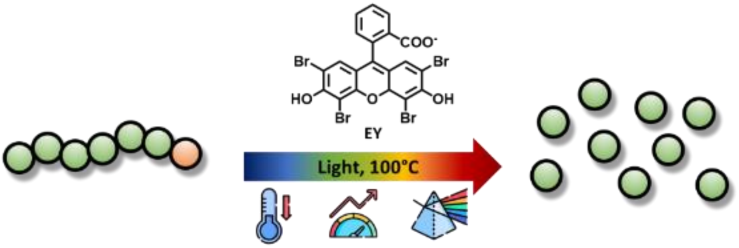

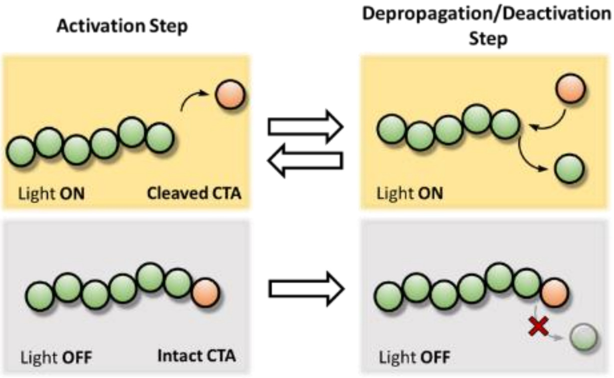

Part of this Chapter has been published as:

"V. Bellotti, K. Parkatzidis, H. S. Wang, N.D.A. Watuthanthrige, M. Orfano, A. Monguzzi, N. P. Truong, R. Simonutti, A. Anastasaki, *Light-accelerated depolymerization catalyzed by Eosin Y*, Polym. Chem., **2023**, 14, 253-258."

And "V. Bellotti, H. S. Wang, N. P. Truong, R. Simonutti, A. Anastasaki, *Temporal regulation of PET-RAFT controlled radical depolymerization*, Angew. Chem. Int. Ed. **2023**, e202313232.

6.1 Introduction

As we now know by now, RDRPs techniques allows for the production of well-defined polymers with tailored molecular weight, dispersity, block sequence, and architectures for the construction of advanced functional materials.[1–6] Anyhow, these materials are not fully integrated in the current market mainly due to the use of expensive chain transfer agents. One way to promote the use of RDRP-made polymers for industrial production is the ability to recycle the polymer, retrieving the initial monomers and CTA and producing new materials.

Increasingly efforts have been focused lately on the depolymerization of RDRP-made polymers due to the easier generation of active radicals that allows fast and efficient depolymerization in the right conditions. [7–14] In fact, very low depolymerization can be observed when the end groups are removed.[7,8] Initially, researchers centered their attention on backbone degradation yielding low molecular weight oligomers[15–19] but recently depolymerization with the aim of fully regenerating the monomers attracted considerable attention to such an extent that it has been classified as one of the top 10 emerging technologies in chemistry by IUPAC.[20] For example, Ouchi's group used a Cl-capped poly(methyl methacrylate) (PMMA), previously synthesized by ATRP, which was depolymerized in the presence of a ruthenium catalyst achieving moderate conversion (e.g., 24%) at 120 °C.[12] Subsequently, Matyjaszewski and co-workers improved the depolymerization yield of ATRP-made polymers (e.g., Cl-capped poly(poly(dimethylsiloxane) methacrylate and poly(butyl methacrylate)) by the aid of a copper catalyst ($CuCl_2$/tris(2-pyridyl methyl)-amine) at 170 °C, achieving up to 67% depolymerization.[7,9] For RAFT synthetized polymers the groups of Gramlich[13] demonstrated the depolymerization of bottlebrush poly-(oligo(dimethylsiloxane) methacrylate) (PODMSMA) and poly-(oligo(ethylene glycol) methacrylate) (POEGMA). More recently near-quantitative depolymerization of non-bulky, cross-linked and functional polymethacrylates with different terminal CTAs and in various solvents was achieved by thermally driven depolymerization.[8,10]

However, some of the challenges in the chemical depolymerization of RDRP polymers are not addressed yet. For instance, the use of less expensive solvents, the increase of the reaction kinetics, and lower temperature. On this topic, the transition from a thermal to a photo-thermal system can bring several advantages in the field of depolymerization. Light is one of the most attractive stimuli that have been introduced in the field of polymer synthesis due to its abundant availability, low energy consumption,[21] possibility to have mild reaction conditions,[22–26] and flexibility of diverse reactions set up such as flow reactors.[27] In addition, with the aid of light, the polymerization outcome can be tuned by changing the emission profile, wavelength, intensity,[28], and ON/OFF states.[29] In particular, this last feature brings to the development of spatial-temporal control, which is particularly appealing for surface applications[30,31] and 3D/4D printing.[32–34] The possibility to easily modulate the consecutive initiation and termination for different cycles is possible for RDRP polymerization because the activation/deactivation equilibrium is finely controlled. However, it is difficult to translate this concept in depolymerization where the depropagation would continue in the dark (upon switching OFF the light) due to the influence of the thermal depolymerization, thus precluding the possibility for temporal control. In addition, the large majority of the above mentioned chemical recycling approaches report an uncontrolled depolymerization process, whence upon chain-end cleavage, rapid and complete unzipping of the polymer chain occur, generating back the monomer units. This effect can be observed by GPC traces, in fact, both for ATRP and RAFT polymers, a very low shift of the molecular weight (M_n) in comparison with the conversion has been observed in the seminal works. Additional control in the depolymerization of RAFT-made polymers could be in possible achieved by enhancing the deactivation of the chains during depolymerization.

In this chapter, we report for the first time that the use of light and specific photocatalysts could improve both the depolymerization rate and the overall depolymerization conversion. The activation of the CTA under light irradiation, as occurs in PET-RAFT polymerization,[35–40] has been exploited to homolytic cleavage of the C-S bond results in radical generation without the addition of exogenous radical sources,[41,42] which could be advantageous for depolymerization reaction. The use of photocatalysis allows to decrease the depolymerization temperature (up to 100 °C in this first section) with respect to thermal depolymerization. It is noted that the regeneration of the building blocks, in particular non-bulky monomers, is commonly triggered at high temperatures (≥120 °C). In fact, PMMA has been efficiently depolymerized within 8 h at 120 °C, yielding 86% of monomer. However, when the reaction was ran at 100 °C, a much slower depolymerization rate was obtained and the final yield dropped to 64%.[8] Moreover, we also aimed to exploit all the possible advantages of photocatalysis, resulting in a control radical depolymerization where the initiation is possible only when the light is ON while the thermal initiation is completely suppressed in the dark. The key strategy for achieving this temporal regulation is to manipulate the activation/deactivation equilibrium for photocatalyzed depolymerization in order to encourage deactivation over depropagation. However, enhanced deactivation of the depropagating chains is a necessary but not sufficient parameter to achieve perfect temporal control. In fact, the experimental conditions in which the generation of the active radicals by thermolysis was negligible has been investigated to obtain CTA cleavage (activation) only when the light was switched ON (**Scheme 6.1**). This is the first report of light-mediated depolymerization following a reverse PET-RAFT polymerization pathway.

Eosin Y (EY) is a well-studied, non-toxic organic metal-free catalyst, already employed for a variety of organic reactions.[43] For this reason, EY was the photocatalyst of choice for our study.

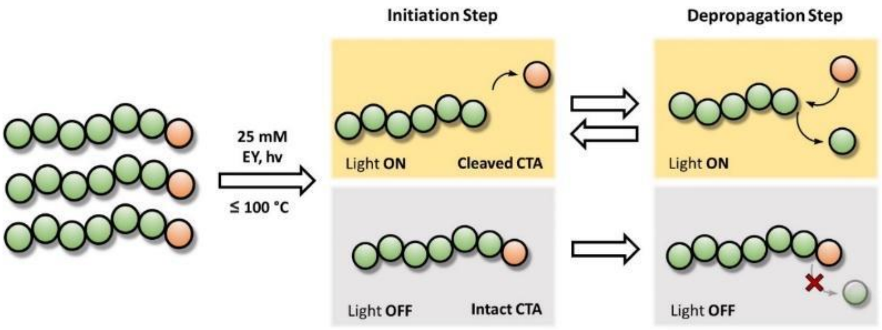

Scheme 6.1: Graphic illustration of temporal control PET-RAFT depolymerization. At increased concentration (25 mM), low temperatures, and EY as photocatalyst under green light activation of the CTA is possible when the light is switched on, generating the active macroradical. Depropagation starts, regenerating the monomer until the chain is deactivated by the RAFT agent which can again be activated by light. This process is suppressed when the light is off due to the lack of activation.

6.2 Materials and Methods

6.2.1 Materials

All materials were purchased from either Sigma Aldrich or Fischer Scientific. Monomers were filtered through basic alumina before use.

6.2.2 Experimental procedures

Polymerization of MMA using 2-cyano-2-propyl dithiobenzoate as a RAFT agent (PMMA-DTB).

Into a 25 mL Schlenk tube, 92.13 mg of 2-cyanoprop-2-yl dithiobenzoate (416.3 μmol, 1 equiv) and 6.85 mg AIBN (41.7 μmol, 0.1 equiv) were dissolved in 3.75 mL toluene. Subsequently, 5.32 mL of MMA (5.0 g, 49.9 mmol, 120 equiv) and a stirrer bar were added, and the tube was sealed with a septum, prior to deoxygenation by nitrogen bubbling for 15 min. Polymerization was conducted in a pretreated oil bath at 70 °C for 5 h with a 400-rpm stirring rate. Polymerization was stopped at 40% conversion by removing the reaction from the oil bath and exposing it to air. PMMA macroCTA was precipitated at least three times in cold methanol and vacuum-filtered using a Buchner funnel. The precipitates were dried in a vacuum oven for at least 12 h before use.

Polymerization of MMA using 2-Cyano 2-propyl dodecyltrithiocarbonate as a RAFT agent.

In a 15 mL vial, 57.5 mg of 2-Cyano 2-propyl dodecyltrithiocarbonate (166.5. μmol, 1 equiv) and 2.7 mg AIBN (16.6 μmol, 0.1 equiv) were dissolved in 1.3 mL toluene. Subsequently, 2.66 mL of MMA (2.5 g, 25 mmol, 150 equiv) and a stirrer bar were added, and the flask was sealed with a septum, prior to deoxygenation by nitrogen bubbling for 15 min. Polymerization was conducted in a pretreated oil bath at 70 °C for 4.5 h with a 400-rpm stirring rate. Samples were taken periodically under a nitrogen blanket for ^{1}H-NMR analysis and passed through a syringe filter (0.45 µm PTFE membrane) prior to SEC analysis. Polymerization was stopped at 38% conversion by removing the reaction from the oil bath and exposing to air. PMMA macroCTA was precipitated at least three times in cold methanol and vacuum-filtered using a Buchner funnel. The precipitates were dried in a vacuum oven for at least 12 h before use.

Polymerization of MMA using 2-Cyanobutan-2-yl 4-chloro-3,5-dimethyl-1H-pyrazole-1- carbodithioate as a RAFT agent.

In a 15 mL vial, 143.7 mg of 2-Cyanobutan-2-yl 4-chloro-3,5-dimethyl-1H-pyrazole-1-carbodithioate (499.4 µmol, 1 equiv) and 8.2 mg AIBN (16.6 µmol, 0.1 equiv) were dissolved in 1.3 mL toluene. Subsequently, 2.66 mL of MMA (2.5 g, 25 mmol, 50 equiv) and a stirrer bar were added, and the flask was sealed with a septum, prior to deoxygenation by nitrogen bubbling for 15 min. Polymerization was conducted in a pretreated oil bath at 70 °C for 6 h with a 400-rpm stirring rate. Samples were taken periodically under a nitrogen blanket for 1H-NMR analysis and passed through a syringe filter (0.45 µm PTFE membrane) prior to SEC analysis. Polymerization was stopped at 65% conversion by removing the reaction from the oil bath and exposing to air. PMMA macroCTA was precipitated at least three times in cold methanol and vacuum-filtered using a Buchner funnel. The precipitates were dried in a vacuum oven for at least 12 h before use.

Polymerization of BzMA using 2-cyano-2-propyl dithiobenzoate as a RAFT agent (PBzMA-DTB).

Into a 10 mL round bottom flask, 125.6 mg of 2-cyanoprop-2-yl dithiobenzoate (380 µmol, 1 equiv) were dissolved in 3 mL toluene. A stock solution of AIBN (10 mg) was prepared in 1 mL toluene, and 617 µL of this solution (6.17 mg, 37.6 µmol, 0.1 equiv) was transferred to the flask. Subsequently, 5.08 mL of BzMA (5.3 g, 30 mmol, 80 equiv) and a stirrer bar were added, and the flask was sealed with a septum, prior to deoxygenation by nitrogen bubbling for 15 min. Polymerization was conducted in an oil bath at 70 °C for 4 h with a 400-rpm stirring rate. Polymerization was stopped at 59% conversion by removing the reaction from the oil bath and removing the septum. PBzMA macroCTA was precipitated at least three times in cold methanol and vacuum-filtered using a Buchner funnel. The precipitates were dried in a vacuum oven for at least 12 h before use.

Polymerization of OEGMA using 2-cyano-2-propyl dithiobenzoate as a RAFT agent (POEGMA-DTB).

Into a 50 mL round bottom flask, 44.3 mg of 2-cyanoprop-2-yl dithiobenzoate (200 µmol, 1 equiv) were dissolved in 10 mL toluene. A stock solution of AIBN (10 mg) was prepared in 1 mL toluene, and 328 µL of this solution (3.28 mg, 20 µmol, 0.1 equiv) was transferred to the flask. Subsequently, 10 g of OEGMA (20 mmol, 100 equiv) and a stirrer bar were added, and the flask was sealed with a septum, prior to deoxygenation by nitrogen bubbling 2 for 15 min. Polymerization was conducted in an oil bath at 70 °C for 4 h with a 400-rpm stirring rate. Polymerization was stopped at 45% conversion by removing the reaction from the oil bath and removing the septum. POEGMA macroCTA was precipitated at least three times in diethyl ether/hexane solution (50% v/v) and vacuum-filtered using a Buchner funnel. The precipitates were dried in a vacuum oven for at least 12 h before use.

Polymerization of DMAEMA using 2-cyano-2-propyl dithiobenzoate as a RAFT agent (PDMAEMA-DTB).

Into a 10 mL round bottom flask, 70.4 mg of 2-cyanoprop-2-yl dithiobenzoate (318 µmol, 1 equiv) were dissolved in 6 mL toluene. A stock solution of AIBN (10 mg) was prepared in 1 mL toluene, and 522 µL of this solution (5.22 mg, 31.8 µmol, 0.1 equiv) was transferred to the flask. Subsequently, 4.29 mL of DMAEMA (4 g, 25.4 mmol, 80 equiv) and a stirrer bar were added, and the flask was sealed with a septum, prior to deoxygenation by nitrogen bubbling for 15 min. Polymerization was conducted in an oil bath at 70 °C for 4 h with a 400-rpm stirring rate. Polymerization was stopped at 40% conversion by removing the reaction from the oil bath and removing the septum. PDMAEMA macroCTA was precipitated at least three times in pentane and vacuum-filtered using a Buchner funnel. The precipitates were dried in a vacuum oven for at least 12 h before use.

Polymerization of BuMA using 2-cyano-2-propyl dithiobenzoate as a RAFT agent (PBuMA-DTB).

Into a 10 mL round bottom flask, 64.9 mg of 2-cyanoprop-2-yl dithiobenzoate (293 µmol, 1 equiv) were dissolved in 2.5 mL toluene. A stock solution of AIBN (10 mg) was prepared in 1 mL toluene, and 481 µL of this solution (4.81 mg, 29.3 µmol, 0.1 equiv) was transferred to the flask. Subsequently, 5.6 mL of BuMA (5.0 g, 35.2 mmol, 120 equiv) and a stirrer bar were added, and the flask was sealed with a septum, prior to deoxygenation by nitrogen bubbling for 15 min. Polymerization was conducted in an oil bath at 70 °C for 4 h with a 400-rpm stirring rate. Polymerization was stopped at 49% conversion by removing the reaction from the oil bath and removing the septum. PBuMA macroCTA was precipitated at least three times in cold methanol and vacuum-filtered using a Buchner funnel. The precipitates were dried in a vacuum oven for at least 12 h before use.

General thermal depolymerization procedure for PMMA

PMMA-DTB will be used as the model example to describe a typical depolymerization procedure. In a 125 ml schlenk tube, 21.5 mg of PMMA was dissolved in 40 ml 1,4-dioxane (5.17 mM of MMA repeat unit). 15 mg of 350 g/mol poly(ethylene glycol) monomethyl ether was added as an internal standard for 1H NMR analysis. The schlenk tube was sealed with a rubber septum and deoxygenated by nitrogen bubbling for 20 min. The schlenk tube was then put into a 100 ℃ oil bath to start the reaction. The schlenk tube was submerged into the oil bath until the surface of the solution inside was submerged ~2 cm below the surface of the oil bath. To take samples, the reaction was periodically removed from the oil bath and quickly added to an ice bath until the solution cooled to room temperature. The solution was then sampled under a nitrogen blanket. For SEC samples, ~3 ml of the sample solution was blow-dried, dissolved in DMAc, and passed through a syringe filter (0.45 μm PTFE membrane).

General photothermal depolymerization catalyzed by Eosin Y procedure for PMMA

A typical depolymerization procedure for PMMA-DTB depolymerization is here described for a general concentration of 5 mM. 71.5 µL of a stock solution (0.2 mg/mL) of Eosin Y was added (100 ppm with respect to the MMA repeating units) in a 125 ml schlenk tube. 21.5 mg of PMMA was dissolved in 40 ml 1,4-dioxane (5.17 mM of MMA repeat unit). 15 mg of 350 g/mol poly(ethylene glycol) monomethyl ether was added as an internal standard for 1H NMR analysis. The schlenk tube was sealed with a rubber septum and deoxygenated by nitrogen bubbling for 20 min. The schlenk tube was then put into a 100 ℃ oil bath and the LED light strip was turned on at the selected wavelength to start the reaction. The LED lights were organized in a circular way around the oil bath whit a distance of 3 cm, the reactor was then covered by aluminum foil. The schlenk tube was submerged into the oil bath until the surface of the solution inside was submerged ~2 cm below the surface of the oil bath. To take samples, the reaction was periodically removed from the oil bath and quickly added to an ice bath until the solution cooled to room temperature. The solution was then sampled under a nitrogen blanket. For SEC samples, ~3 ml of the sample solution was blow-dried, dissolved in DMAc, and passed through a syringe filter (0.45 µm PTFE membrane). For temporal control experiments, the LED light was switched ON and OFF by a remote controller.

Analysis of RI/UV SEC signal during depolymerization

Relative SEC signals were analyzed by preparing the samples at the same concentration of the reaction mixture. Specifically, 3 ml of the reaction was sampled at various time points (including t0, before the reaction was put into the oil bath) and dried by air blowing. The dried polymer residue was then redissolved into 1 ml of N,N-dimethylacetamide and analyzed with SEC. The signal intensities for subsequent time points were not normalized and compared with each other. The conversion was determined by comparison of RI signal at a certain time to the one at t_0.

Analysis of ^{1}H NMR during depolymerization

Depolymerization conversions were also determined by ^{1}H NMR, comparing the monomer vinyl signals to the polymer backbone -CH_3 signals (simply taking a sample in dioxane and re-dissolving it in deuterated chloroform). In addition, an internal standard is added in each reaction to ensure accurate conversion calculation through an alternative way. Specifically, a second NMR sample was prepared by re-dissolving the dried reaction mixture (blowing the solvent with air). Conversions were then calculated by comparing the intensity of the backbone –CH_3 signals before and after depolymerization against a nonvolatile internal standard (methoxy-terminated polyethylene glycol). Depolymerization conversions from the two methods deviated by <5%.

6.3 Results and Discussion

6.3.1 Light-Accelerated Depolymerization

To initiate the study, the starting polymer was synthesized by RAFT polymerization using 2-cyano2-propyl dithiobenzoate as the chain transfer agent at 70 °C resulting in a well-defined polymer with low dispersity ($Đ$ = 1.14, M_n = 6300 g/mol) and high end-group fidelity (**Figure 6.1a**). Before use, the polymer was rigorously purified until no vinyl protons could be observed via ^{1}H-NMR, thus confirming the absence of any remaining monomer (**Figure 6.1b**).

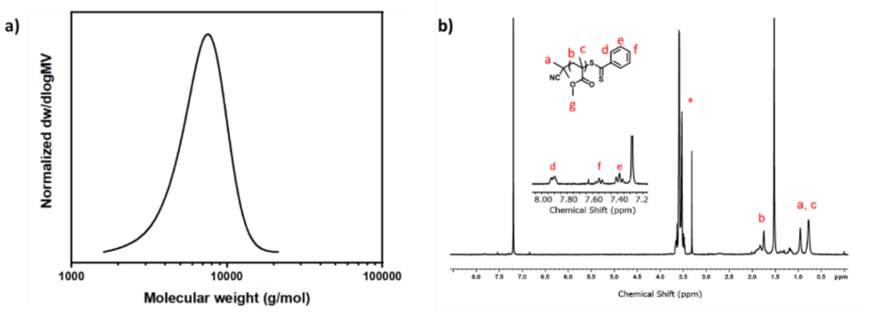

Figure 6.1: a) SEC trace of PMMA-DTB synthesized via RAFT polymerization with 2-cyano-2- propyl dithiobenzoate as a chain transfer agent ([CTA]:[AIBN]:[MMA] = 1:0.1:120) (*M*n = 6,300; *Đ* = 1.14). b) ^{1}H-NMR spectrum of purified PMMA-DTB prior to depolymerization. (*) Internal standard

Thermal depolymerization of PMMA was repeated with the same conditions previously reported (100 °C, 5 mM).[8] In line with the reported results, low depolymerization profile respect to 120°C depolymerization was obtained. The final depolymerization yield after 8 h under thermal conditions 66% of monomer regeneration with only 16% in the first 1 h (**Figure 6.2**). It should be considered that the final depolymerization yield is a combination of various factors including the monomer concentration at equilibrium, the number of living chains compared to the total amount of chains, and the chains side reactions that may occur at high temperatures (e.g. Chugaev elimination) resulting in further loss of the end-group fidelity. Since the monomer concentration at equilibrium is also dependent on the depolymerization temperature we expect lower yield when the temperature is decreased.

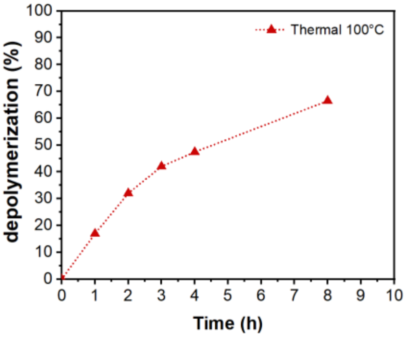

Figure 6.2: Depolymerization conversion versus time of PMMA-DTB thermal depolymerization. Reactions was run at 100 °C, 5 mM in 1,4-dioxane.

In order to test the performance of the photocatalyzed system, the depolymerization of PMMA was repeated in the presence of green light (λ_{max}=510 nm) and Eosin Y (**Figure 6.3a**). A homemade photo-thermal set up was built in order to simultaneously irradiate the system an heat up. RGB LED strip was placed in circular shape and positioned around the oil bath, as illustrated in **Figure 6.3b**.

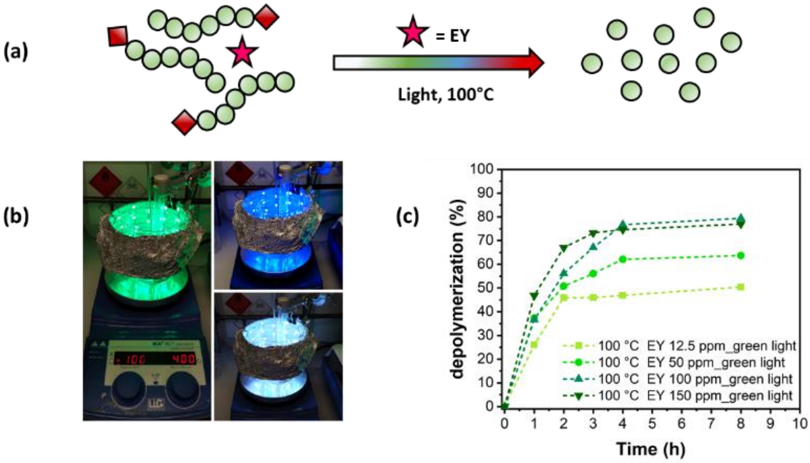

Figure 6.3: (a) Schematic illustration of reversing RAFT polymerization in the presence of Eosin Y and light irradiation (b) Photothermal reactor set-up for different wavelengths (c) Kinetics of light-accelerated depolymerization catalyzed by different concentrations of Eosin Y under green light.

Significant acceleration of the depolymerization rate was observed, even when a very low amount of EY (12.5 ppm with respect to the MMA repeat unit) was added to the photo-thermal reactor. The presence of light and EY considerably enhanced the depolymerization rate, in fact, after the first hour, 26% of the monomer was regenerated, against the 16% reached with the thermal system. Even though the rate of the depolymerization was increased the reaction plateaued after 3 h with a maximum conversion of 45%. In order to enhance the performance, the concentration of Eosin Y was gradually increased to 50 ppm, 100 ppm, and 150 ppm (**Figure 6.3c**). In the first two cases, the depolymerization rate after 1 h reached 37% of conversion for both concentrations, whereas the final yield was increased to 61% for 50 ppm and 80% for 100 ppm. Finally, with a concentration of 150 ppm of Eosin Y, no further enhancement in the depolymerization rate was observed, although the rate of the reaction continued to increase. As the final depolymerization yield was not improved for higher EY loading we decided to conduct the subsequent experiments with 100 ppm of PC. Nevertheless, these experiments unambiguously demonstrate that the rate of depolymerization under irradiation is affected by the concentration of EY, which therefore play a very important role in the regulation of depolymerization. Furthermore, the final depolymerization conversion can be preserved (80%) even when the temperature is lowered from 120 °c to 100 °C, with a significant acceleration compared to the thermal system (from 16% to 37% depolymerization within 1 h).

For each analysis, the regeneration of the monomer, rather than the decomposition of the polymer in oligomers was confirmed by ^{1}H NMR (**Figure 6.4a**). The vinyl signals of MMA appear after the first hour and increased over time while the signals of the polymer decrease. Considering the SEC traces reported in **Figure 6.4b** we can also conclude that the depolymerization proceeds through an uncontrolled pathway, in which the polymer chains are unzipped back to the monomer very fast once the end-radical is formed. This result is in line with the previous reports in similar conditions. [4,7,8,10]

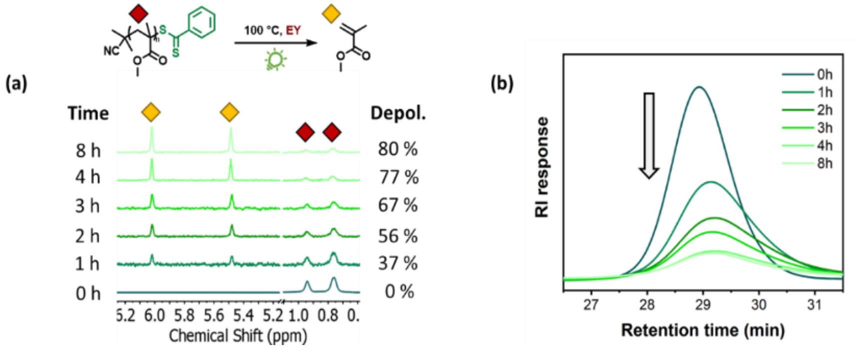

Figure 6.4: (a) ^{1}H NMR spectra of the PMMA depolymerization, vinyl peaks appearances over time confirming the monomer regeneration. Reactions were run in 1,4-dioxane at 5 mM and 100 °C in the presence of Eosin Y and green light. (b) Relatives SEC traces of PMMA during depolymerization with 100 ppm of Eosin Y.

Higher molecular weight PMMA, with a degree of polymerization (DP) of 260 was also synthesized and subjected to the optimized depolymerization condition, yielding 62% of monomer regeneration within 8h (**Figure 6.5a**). A dependency of the depolymerization plateau with the DP has been already reported for the thermal system.[8] Anyhow the photo-thermal experiment shows an improvement in the final depolymerization conversion when compared to the previously reported thermal approach. Moreover, under the same conditions, different polymers could be efficiently depolymerized, including poly benzyl methacrylate (PBzMA), poly dimethylaminoethyl methacrylate (PDMAEMA), and poly oligo (ethylene glycol) methyl ether methacrylate (POEGMA) yielding high conversions in all cases (68-80%) (**Figures 6.5b** and **c**).

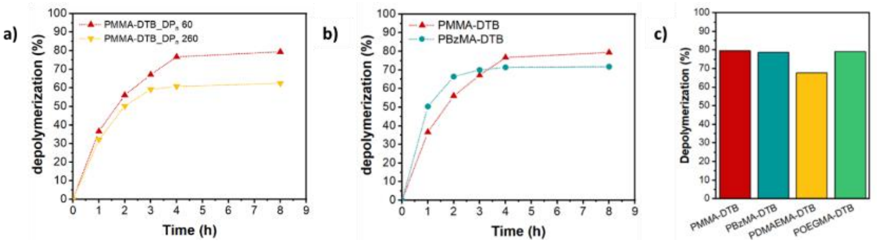

Figure 6.5: a) Depolymerization conversion versus time of PMMA-DTB with DP of 60 (red triangles), and 260 (yellow triangles). b**)** Depolymerization conversion versus time of PMMA-DTB (red triangles), and PBzMA (green dots). c) Depolymerization of PMMA, PBzMA, PDMAEMA, and POEGMA after 8 hours of green irradiation. Reactions were run at 100 °C, 5 mM, 100 ppm of Eosin Y, and green light in 1,4-dioxane.

Besides the polymer nature, the effect of different RAFT chain-end groups on both the depolymerization rates and final conversions was evaluated. PMMA was synthesized using 2-cyano 2-propyl dodecyltrithiocarbonate (TTC), and 2-cyanobutan-2-yl 4-chloro-3,5-dimethyl1H-pyrazole-1-carbodithioate (pyrazole-CD) as the RAFT agents. Depolymerization of PMMA-TTC and PMMA-pyrazoleCD was performed both by thermal and photo-thermal (100 °C, green light, 100 ppm of Eosin Y, 5 mM repeat unit concentration) methods. Remarkable results were obtained for the depolymerization PMM-TTC, for which 50% of monomer generation was detected in 1 h, instead of the 13% obtained for the experiment performed under heat. In addition, the thermal depolymerization led to a final conversion of 42% while the presence of light and EY significantly increased the depolymerization conversion to 68% (**Figure 6.6a**). Analog behavior was observed for the depolymerization of the PMMA-pyrazoleCD (**Figure 6.6b**). The rate of the depolymerization doubled in the first hour in the presence of light and Eosin Y and the final yield was improved. The reported data highlight the generality of the light/catalytic-depolymerization methodology, for different methacrylates, expanding the potential of this new approach.

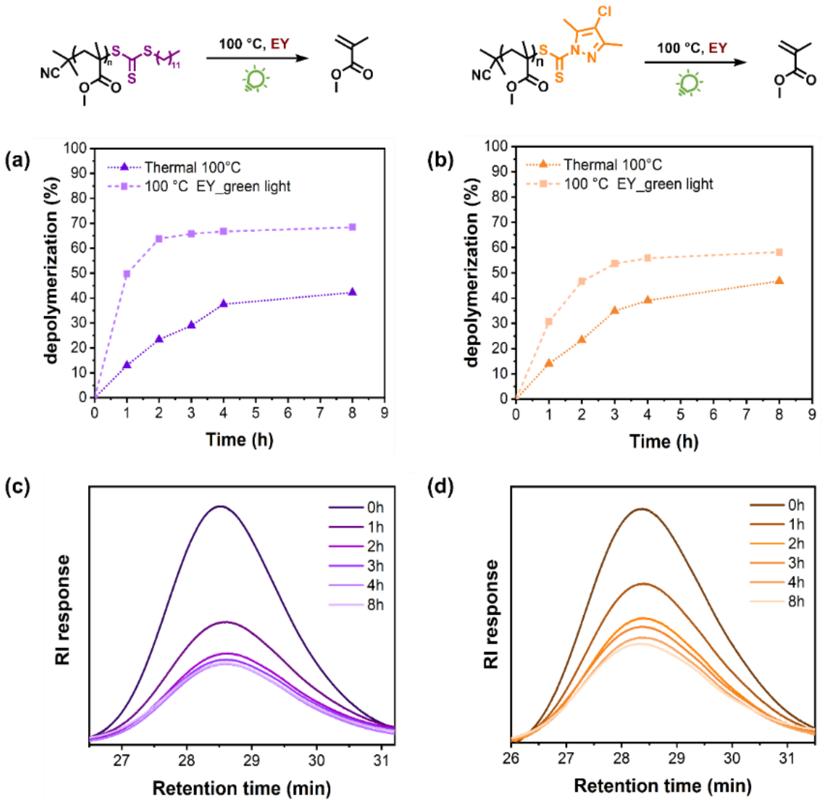

Figure 6.6: Kinetic study comparing green light-accelerated depolymerization of PMMA catalyzed by Eosin Y at 100°C versus thermal depolymerization using (a) TTC and (b) pyrazoleCD chain transfer agents. Respectively, SEC traces at different depolymerization times (c) and (d).

Different solvents were screened for the depolymerization of PMMA-DTB under green light irradiation in the presence of 100 ppm Eosin Y. In particular, reactions were conducted in dimethyl sulfoxide (DMSO), dimethyl formamide (DMF), toluene, and xylene (**Figure 6.7**). In line with the previous work on thermal depolymerization,[10] DMF shows a lower conversion (i.e. 35%) possibly due to partial ammonolysis of the CTA, whereas xylene and toluene allow a monomer regeneration of 52% and 50% respectively. Surprisingly, in DMSO very high final conversion (i.e. of

82%) was obtained. This is a remarkable result when compared with the 35% conversion obtained by thermal depolymerization at 120 °C, and conversion close to zero when the temperature was decreased to 100 °C, within the same time frame. The excellent results obtained in DMSO can be rationalized by an efficient radical formation at the chain end, in fact this solvent has been intensively used in PET-RAFT polymerization. [29,45,46] In addition, EY can be found in different forms with various catalytic activities. DMSO allows proton extraction from the neutral form of EY into the mono or di-anionic forms, which are more photoredox catalytically active.[47]

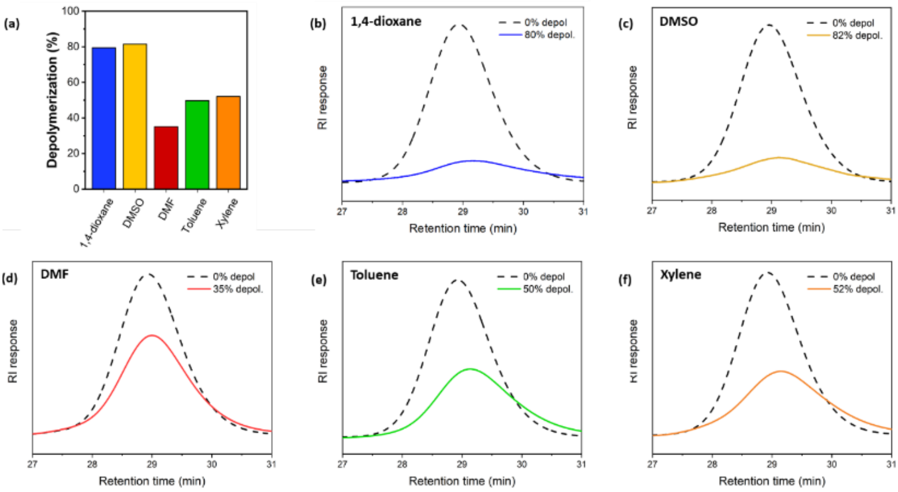

Figure 6.7: (a) Depolymerization conversion after 8 hours of PMMA-DTB with 100 ppm of Eosin Y, 5mM and 100°C using different solvents under green irradiations and the relative SEC traces before and after depolymerization.

Finally, the effect of light intensity and wavelength was investigated. When the light intensity was decreased from 2.31 mW/cm^2 (**Table 6.1**, experimental section) to 0.18 mW/cm^2, a slower depolymerization was observed. This experiment further highlights the importance of light to accelerate depolymerization, analogously to PET-RAFT polymerization. Noteworthy, even when the intensity was decreased to the minimum power accessible with commercially available LED, a significant acceleration of the rate was observed when compared to the control experiment in the dark under identical conditions (**Figure 6.8**).

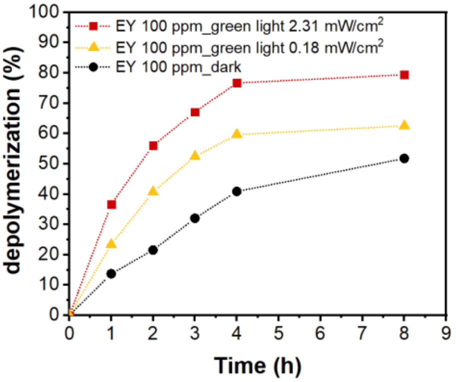

Figure 6.8: Depolymerization conversion versus time of PMMA-DTB in the presence of Eosin Y under green irradiation and high intensity of the photoreactor (red squares), low intensity (yellow triangles), and in the dark (black dots). Reactions were run at 100 °C, 5 mM, and 100 ppm of Eosin Y, in 1,4-dioxane.

In all previous experiments, the green light was selected because of the maximum absorption of EY (λ_{max} = 524 nm). In fact, green is the most commonly utilized light source for Eosin Y in organic chemistry.[43] Even though, it is known that PET-RAFT polymerization can be conducted under a range of wavelengths, depending on the catalyst.[28] As such, we performed the depolymerization of PMMA by irradiating at different wavelengths, in particular comparing green with blue and white lights (**Figures 6.9**). All the investigated wavelengths lead to high monomer regeneration after 8 hours (i.e. 78% for blue light and 75% for white) with comparable kinetic respect to the green LED. By overlapping the absorption spectrum of Eosin Y with the emission profile of the RGB LED (**Figure**

8.1, Appendix I) it is clear that green LED allows optimal excitation, near the maximum absorption of the PC. However, the smaller absorption at 460 nm, corresponding to the blue LED appears to be enough to excite EY to the singlet state and activate the C-S bond of the macro-CTA with the same efficiency of green irradiation. In fact, it has been demonstrated that some catalyst display effective performance far from the maximum absorption wavelength depending on the pathways available for the intersystem crossing of their excited state (S1).[50]

It can be concluded that despite the excitation wavelength, both blue, green, and white irradiations improve the depolymerization kinetic and yield with respect to the thermal system, making this process more versatile. Depolymerization under UV irradiation has been avoided since it was already reported that, in polymer synthesis, the RAFT chain-end undergoes degradation under high energetic light. [51–53]

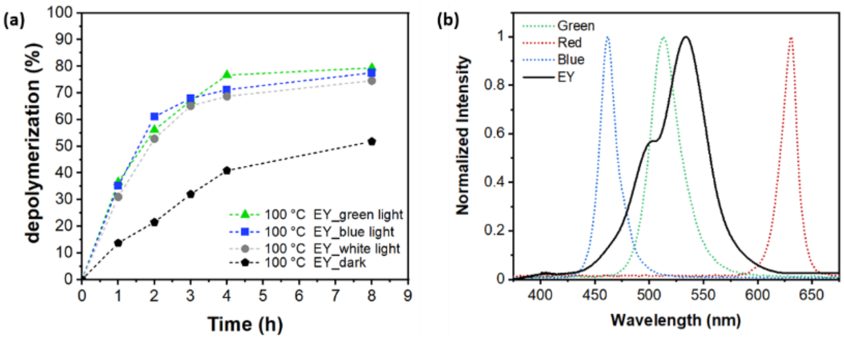

Figure 6.9: a) depolymerization conversion versus time of PMMA-DTB in the presence of Eosin Y under green, blue and white irradiation. Reactions were run at 100 °C, 5 mM, and 100 ppm of Eosin Y, in 1,4-dioxane. b) absorption spectrum of EY in 1,4-dioxane and emission spectra of the three light components of the RGB LED.

To summarize, in this section, we demonstrate that thermal depolymerization of RAFT-made polymers can be improved by the aid of light ad photo-redox catalysis achieving higher conversion and enhanced rate even at lower temperatures. This result is a step forward in the chemical depolymerization of RDRP materials. Anyway, under this condition we were not able to reverse RAFT polymerization in a controlled manner. Once the CTA is cleaved by the chain end, the polymer chain is rapidly unzipped. However, obtaining a control depolymerization pathway could allow us to exploit all the advantages of control polymerization with respect to free radical processes. For this reason, in *section 6.3.2,* the aim is to translate the newly photo-accelerated depolymerization into a reverse PET-RAFT mechanism.

6.3.2 Temporal regulation via PET-RAFT controlled radical depolymerization

Kinetic study at 1 mM concentration has been conducted as a control experiment. After 1 hour (46% depolymerization conversion), a very low shift of the molecular weight was observed (**Figures 6.10b** and **c**). After this time and up to 86% of monomer regeneration, the change in the M_n with respect to the conversion was negligible, and the overall shift was less than 12%, confirming that the monomer regeneration follows a fast and uncontrolled pathway, comparable to free radical polymerization. On the other hand, when the concentration has been increased to 25 mM the shift in the M_n during the depolymerization process is clearly evident (**Figure 6.10f**), concomitantly with an increase in the dispersity values (**Figure 6.10e**). The depolymerization trend seems to follow a control pathway, meaning that deactivation of the macro de-propagating radical can occur in a similar fashion as in RAFT polymerization. Subsequently, the end-group is cleaved again *via* PeT process producing the active macro-radical, which undergoes depropagation regenerating the monomer. Results are summarized in **Table 6.2**.

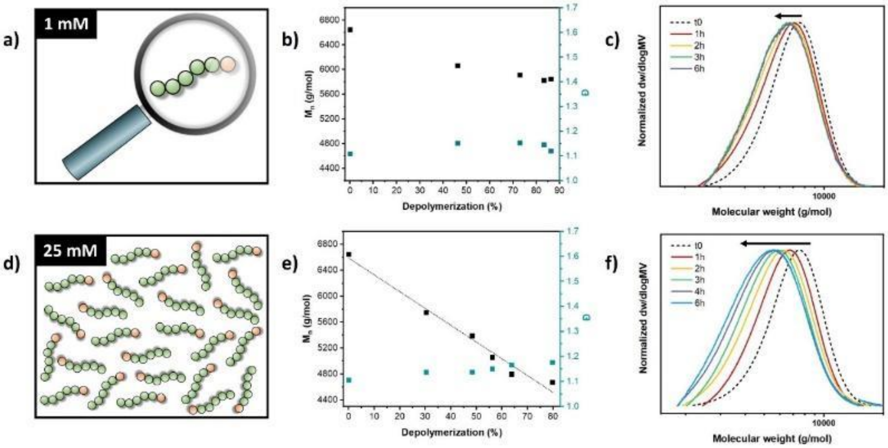

Figure 6.10: PMMA-DTB depolymerization at 100 °C **a)** 1 mM and **d)** 25 mM concentration with respect to the repeating units. Very low shifting toward low molecular weights could be observed for the 1 mM experiments **b)** and **c)**. On the other hand, when the concentration is increased to 25 mM the GPC traces showed linear respect to the depolymerization conversion shift toward low molecular weight **e)** and **f)**.

Table 6.1: Kinetics of PMMA-DTB depolymerization. Reaction run at 100 °C, in 1,4-dioxane, and in the presence of 100 ppm of Eosin Y under green irradiation. ^{a} Monomer conversion calculated with NMR analysis. ^{b} Dispersity and molecular weight obtained by GPC measures.

Entry	**[RU] (mM)**	**Time (h)**	**α (%)^{a}**	**Đ^{b}**	**M_n (Da)^{b}**
1	1	1	46.2	1.15	6 066
2		2	72.9	1.15	5 915
3		3	83.2	1.15	5 826
4		6	86.2	1.12	5 848
5	25	1	30.3	1.14	5 752
6		2	48.3	1.14	5 390
7		3	56.2	1.15	5 059
8		4	63.7	1.17	4 796
9		6	79.7	1.18	4 674

Temporal control experiments were then performed for both 1 and 25 mM by switching the light ON-OFF for four different cycles. When 1 mM concentration was used no evident changes between ON and OFF cycles could be observed, confirming again the lack of control (**Figure 6.11a**). On the other hand, promising results have been obtained in the case of 25 mM, where two different behavior have been observed when the light was ON and OFF (**Figure 6.11b**).

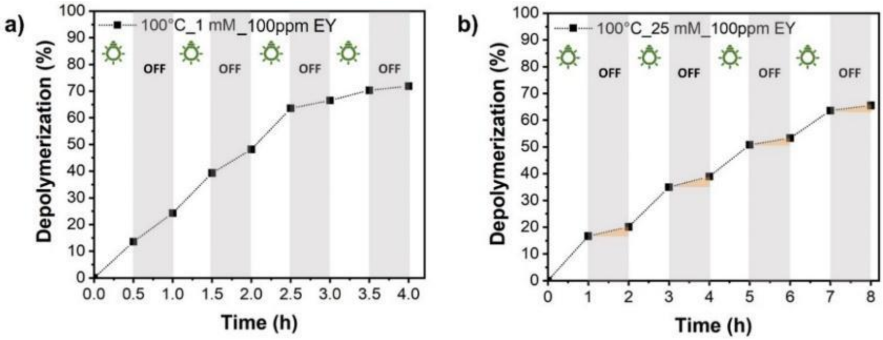

Figure 6.11: Temporal control experiments of photo-catalyzed depolymerization at 100 °C with the addition of 100 ppm of EY, at **a)** 1 mM and **b)** 25 mM. The light was switched ON-OFF every hour for 4 cycles.

In particular, a low depolymerization rate was obtained in the dark, whereas the rate accelerate when the light was switched ON. When the depolymerization percentage of ON and OFF cycles is considered as independent experiments (by summing the depolymerization yield for ON and OFF separately) it is possible to obtain the apparent rate constant of depolymerization ($k_{dp,app}$) (**Figure 6.12**). When the depolymerization proceeded under light irradiation a $k_{dp,app}$ of (2.3 ± 0.04) x 10^{-1} s^{-1} was obtained, whereas this values drop to (3.3 ± 0.04) x 10^{-2} s^{-1} in the case of OFF cycle. These data suggest that temporal control for depolymerization is possible but, under these experimental conditions, the competition between photolysis and thermolysis of the macro-CTA did not provide a full arrest of the depolymerization when the light was switched OFF (12% of the final depolymerization is due to heat contribution alone). Encouraged by these results we decided to conduct a more accurate study of the factors that can influence the depolymerization control, both in terms of molecular weight and temporal control, still maintaining a good balance between kinetic and final depolymerization yield.

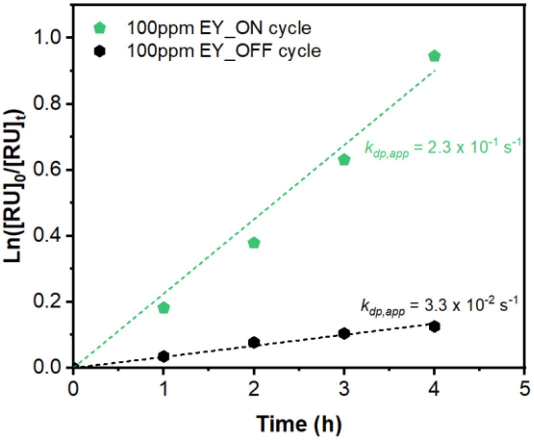

Figure 6.12: Depolymerization kinetic of PMMA-DTB during temporal control experiment considering the ON cycle (green pentagons) and OFF cycle (black hexagons) independently. Reactions were run at 100 °C, 25 mM, and 100 ppm of EY under green light. in 1,4-dioxane.

Study and Optimization of the Controlled Depolymerization Conditions

A systematic analysis of the main parameters involved in the activation/deactivation equilibrium during depolymerization has been performed by varying the repeating unit concentration, the amount of CTA, and the temperature.

The effect of the concentration

In previous works on depolymerization of RAFT-based polymers low concentration (5 mM) has been used due to the high performance in terms of depolymerization yield. [8,10,54,55] When concentration is increased the performance concerning both kinetic and final conversion gets worst, and the trend is much more evident at low temperatures. It’s worth noticing that the use of Eosin Y as a photocatalyst provides good depolymerization yield, achieving 80% after 6 hours at 100 °C (**Figure 6.10**, **Table 6.2** entry **9**) when the concentration is increased to 25mM. The same final conversion, with slightly faster kinetic, was obtained for depolymerization at 5 mM (**Figure 6.13a**). On the other hand, the thermal system is much more affected by the increase of the concentration to 25 mM, resulting in 48% depolymerization after 8 hours. The depolymerization conversion follows a liner trend with different slopes for both thermal and EY catalyzed systems but the thermal system start plateauing at 50 mM (**Figure 6.13b**).

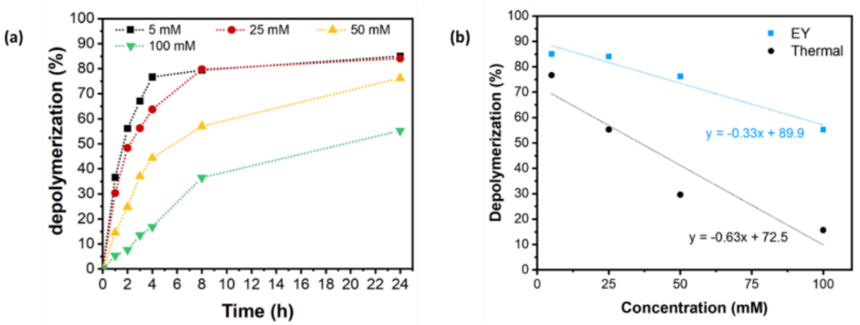

Figure 6.13: a) Depolymerization kinetics of PMMA-DTB at 5 mM (black squares), 25 mM (red dots), 50 mM (yellow triangle), and 100 mM (green triangle). b) Depolymerization conversion of PMMA-DTB after 24 hours at 5, 25, 50, and 100 mM concentrations with respect to the repeating units for the thermal system (black dots) and in the presence of 100 ppm EY under green irradiation (blue squares). Reactions were run at 100 °C, in 1,4-dioxane, and in the presence of 100 ppm of Eosin Y under green irradiation.

Due to the high efficiency of the photocatalyzed depolymerization at 100 °C, the effect of even higher concentrations in the control has been studied. In particular, the molecular weight shift (M_n shift) with respect to the original polymer has been analyzed as the depolymerization proceed for various concentrations, and compared to the theoretical value in ideal conditions ($M_{n(theo)}$ shift = depolymerization conversion).

In **Figure 6.14** is evident that the higher the concentration closer the M_n shift to the theoretical value. As expected, the final depolymerization conversion decreases by increasing the concentration, nevertheless, 37% depolymerization have been achieved at 100 mM and 100°C thanks to the presence of the photocatalyst whereas thermal depolymerization achieved only 15% conversion after 24 hours (**Figure 6.13b**). Impressively, 100 mM concentration resulted in an almost perfect overlap with the ideal case.

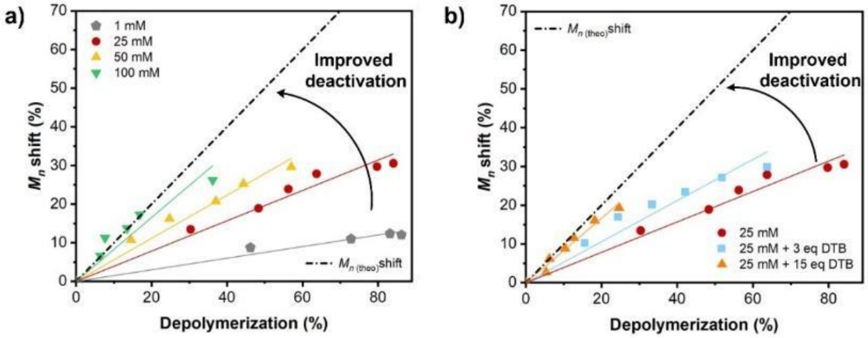

Figure 6.14: M_n shift respect to depolymerization conversion for **a)** different concentrations of the monomer repeating units ($[RU]_0$ = 1 mM, 25 mM, 50 mM, and 100 mM) and for **b)** $[RU]_0$ =25 mM with the addition of different amounts of DTB (equivalent respect to the moles of the polymer). The molecular weight shift has been calculated according to the following formula: M_n shift = ($M_{n(initial)}$ - $M_{n(time,x)}$)/$M_{n(initial)}$ where $M_{n(initial)}$ is the molecular weight of the starting polymer and $M_{n(time,x)}$ is the molecular weight after x hours under depolymerization conditions. All depolymerizations have been conducted at 100 °C with 100 ppm of EY under green light.

Noteworthy, in the range from 25 to 100 mM all the depolymerization experiments results in continuous decreases of the molecular weight over time (linear increases in the M_n shift), but deviation from the ideal behavior (M_n theoretical) is more evident for low concentrations. We hypothesize that in more dilute conditions the rate of deactivation is still slow, meaning that some of the macro active radicals formed on the polymeric chain-end do not have the time to encounter a RAFT or macro-RAFT agent and be deactivated, so they completely unzip to regenerate the monomer. In order to prove this hypothesis, the addition of different amounts of CTA in the 25 mM solution was studied. In particular, 3 and 15 equivalent of DTB with respect to the polymer were added and kinetic studies were performed. An increased amount of CTA in the solution resulted in additional control over the molecular weight until good overlapping with the theoretical M_n shift was reached for 15 DTB equivalents (**Figure 6.14b**), showing that comparable results as the 50 and 100 mM can be obtained at 25 mM by CTA addition. The kinetic of the process decreases by increasing the amount of CTA (**Figure 6.15**) which is a confirmation of the fact that the rate of deactivation is increased.

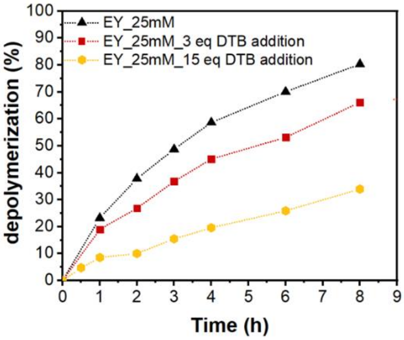

Figure 6.15: a) Kinetic of PMMA-DTB depolymerization at 25 mM (black triangles), 25 mM with the addition of 3 equivalents (red squares) and 15 equivalents (yellow dots) of DTB.

When temporal control studies were performed at 50 mM and 25 mM with the addition of 3 equivalents of DTB a similar behavior as the previously reported experiment (25 mM, **Figure 6.11b**) was obtained, with slightly lower $k_{dp,app}$ during the OFF cycles (**Figure 6.16**). This strongly pointed out that good control over molecular weight in depolymerization is necessary for obtaining temporal control but it’s not enough. The thermal contribution in the CTA cleavage should be completely suppressed in order to be able to stop the depropagation by stopping the CTA activation. For this reason, the effect of lowering the temperature has been analyzed.

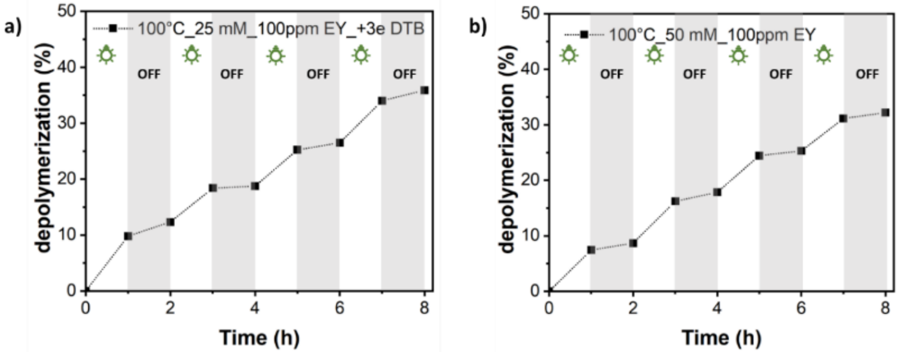

Figure 6.16: Temporal control experiments of photo-catalyzed depolymerization at 100 °C, with the addition of 100 ppm of EY in dioxane at a) $[RU]_0 = 25$ mM with the addition of 3 equivalents of DTB and b) $[RU]_0 = 50$ mM. The light was switched ON-OFF every hour for 4 cycles.

Decreasing the temperature

The depolymerization temperature is a key feature since the thermodynamics of the system strongly relies on it ($\Delta G = \Delta H - T\Delta S$). Reducing the depolymerization temperature is ideal for many factors. Low temperatures can suppress side reactions to the chain termini, allowing better activation/deactivation, which brings increased control, and make the process less energetic dispendious, and scalable. We already showed that the presence of Eosin Y as photocatalyst allows to lower the temperature thus maintaining good performances. In addition, it was recently reported that fine-tuning of the electronic properties of the RAFT agent can also allow thermal depolymerization at low temperatures by making the cleavage of the C-S bond more favored.

Herein, we take advantage of photocatalysis to further decreased the kinetic barrier. In PET-RAFT polymerization the CTA is very rapidly activated by electron or energy transfer from the photocatalyst, even at room temperature. In the same fashion, in depolymerization, the use of a photo-catalyzed system should favor a very fast generation of terminal active radicals. Then, if the temperature is high enough to favor depropagation over propagation depolymerization can occur. Depolymerization of PMMA-DTB under our previous conditions ([RU] = 25 mM, [EY]:[RU] = 100 ppm, green light, 1,4-dioxane) was repeated by decreasing the temperature down to 70 °C and the results were compared with the thermal system at the same dilution. Depolymerization is still possible for the photo-thermal system even at 70°C (**Figure 6.17a**), whereas, in the non-catalyzed system the activation of the RAFT chain-end cannot be provided at low temperatures. 1.6% of the monomer was regenerated after 24 hours at 90 °C (data obtained over 10 experiments repetition), and depolymerization is not possible at lower temperatures (**Figure 6.17b**). The final depolymerization yield after 24 hours at various temperatures follows a linear trend and the intercept of the linear plot with the x axe (minimum temperature for depolymerization to occur) provides a temperature of 61.7 °C for the photo-catalyzed system, much lower than the one obtained for the thermal system, which was 89.8 °C. This is the first evidence of light-induced depolymerization.

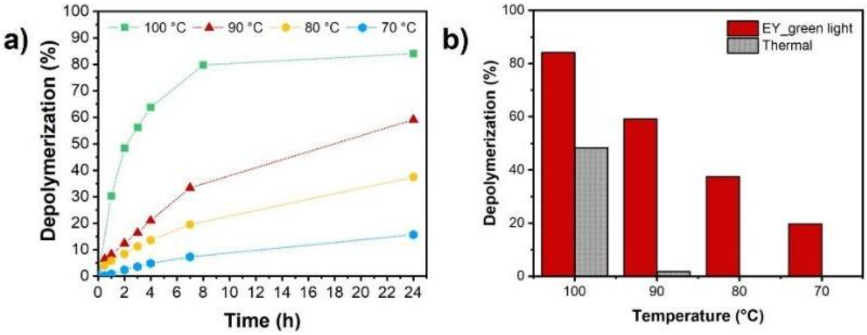

Figure 6.17: a) Kinetic studies of PMMA depolymerization at different temperatures (100 °C, 90 °C, 80 °C, and 70 °C) and **b)** comparison of depolymerization yield after 24 hours between thermal and photo-thermal systems.

At 90 °C linear decreases in molecular weight and an increase in the dispersity was achieved (**Figure 6.18**), likewise the 100 °C experiment, but with higher control. The M_n shift with respect to the depolymerization is in better agreement with the theoretical values when the temperature is decreased (**Figure 6.17c**), guaranteeing additional control. Further decreases in the depolymerization temperature did not provide additional control highlighting the limits for these experimental conditions.

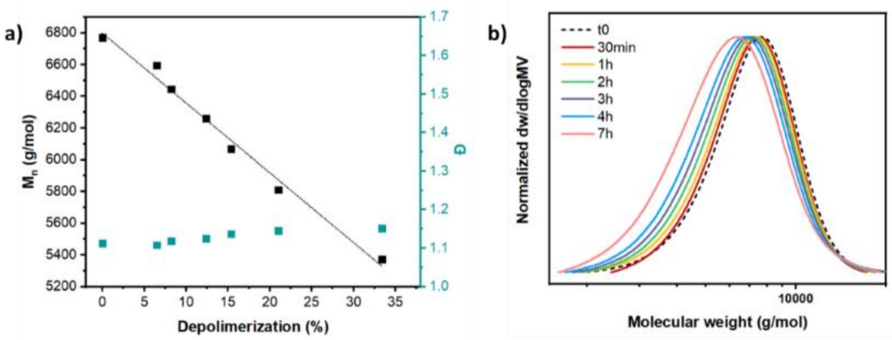

Figure 6.18: a) M_n decrease in PMMA-DTB depolymerization at 90 °C respect to the conversion and relative SEC traces b). The reaction was run at 100 °C, in 1,4-dioxane, and in the presence of 100 ppm EY under green irradiation.

Notably, PMMA depolymerization could occur at 90 °C and in the presence of EY even when no LED was used, likewise PET-RAFT polymerization. The fume hood light is enough to initiate the polymerization but only 23% of depolymerization conversion was reached after 24 h.

Temporal control

Thanks to the additional knowledge provided by this optimization study we decided to repeat the temporal control experiments at 90 °C. At this temperature and with a concentration of repeating units equal to 25 mM the contribution of thermolysis for the RAFT chain-end activation is negligible after 24 hours and completely suppressed in the linear region of the depolymerization (0% depolymerization after 4 hours), whereas PeT activation is still possible. Furthermore, the temperature is high enough to guarantee the unzipping of the chain in a controlled manner and with a good yield. These are, to the best of our knowledge, the optimal conditions for testing the temporal control. Five ON-OFF cycles, 1 hour each, have been performed achieving depolymerization when the light was ON and no depolymerization in the dark (**Figure 6.19a**). GPC traces confirmed a shift of the molecular weight only when the solution was irradiated by light, whereas the M_n was maintained equal at the end of the OFF cycle (**Figure 6.19b**). This is the first example of light-triggered RAFT depolymerization and follows a reverse path as PET-RAFT polymerization.

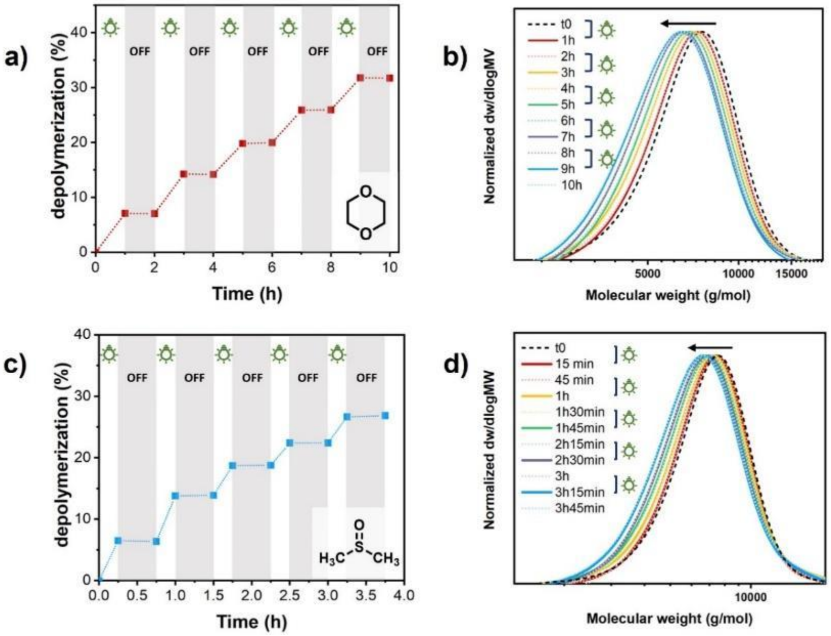

Figure 6.19: Temporal control experiments of photo-catalyzed depolymerization at 90 °C, $[RU]_0$=25 mM with the addition of 100 ppm of EY in dioxane **a)** depolymerization conversion versus time and **b)** GPC traces) and in DMSO (**c)** depolymerization conversion versus time and **d)** GPC traces). The light was switched ON-OFF every hour in dioxane and every 15 minutes-30 minutes (ON-OFF) in DMSO for 5 cycles.

The control of the system was confirmed even when longer OFF periods of 2 and 4 hours were tested, confirming in each case re-activation of the depolymerization (**Figure 6.20**).

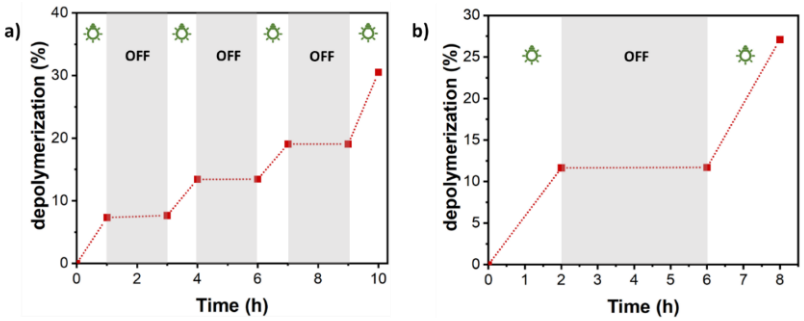

Figure 6.20: Temporal control experiments of photo-catalyzed depolymerization at 90 °C, $[RU]_0$=25 mM with the addition of 100 ppm of EY in dioxane with different ON-OFF cycles.

In the first experiment a) light was switched ON for 1 hour and OFF for 2 hours. In the second experiment b) light was switched ON for 2 hours and OFF for 4 hours.

In order to expand the solvent applicability of temporal control DMSO was used under the same condition (**Figures 6.19c** and **d**). Faster depolymerization was achieved using DMSO, reaching more than 50% depolymerization yield in 2 hours. Due to the faster kinetic the temporal control experiment was performed keeping ON the light for 15 minutes and OFF for 30 minutes. Even in this case, successful temporal control of the depolymerization was achieved together with linear M_n decreased during the ON cycles. Finally, molecular weight and temporal control has been demonstrated also for different polymethacrylates (i.e. poly(benzyl methacrylate) (PBzMA) and poly(butyl methacrylate) (PBuMA)), and PMMA with a trithiocarbonate end-group (**Figure 6.21** and **Figure 6.22**), thus further expanding the scope of our approach.

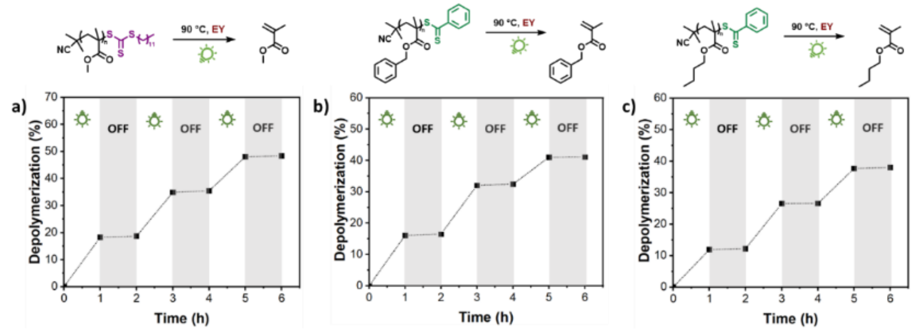

Figure 6.21: Temporal control experiments of photo-catalyzed depolymerization at 90 °C, $[RU]_0$=25 mM with the addition of 100 ppm of EY in dioxane with different “on”-“off” cycles for a) PMMA-TTC, b) PbzMA-DTB and c) PBuMA-DTB.

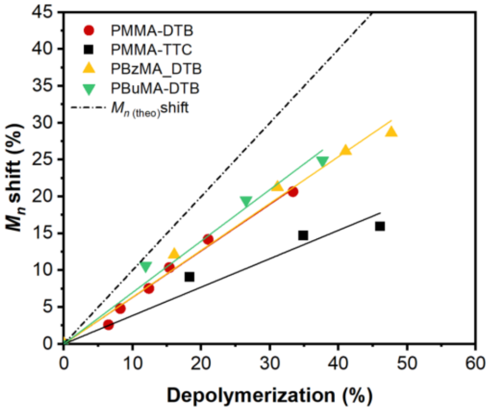

Figure 6.22:M_n shift respect to depolymerization conversion for PMMA-DTB, PMMA-TTC, PBzMA-DTB, PBuMA-DTB. The molecular weight shift has been calculated according to the following formula: M_n shift = ($M_{n(initial)}$ - $M_{n(time,x)}$)/$M_{n(initial)}$ where $M_{n(initial)}$ is the molecular weight of the starting polymer and $M_{n(time,x)}$ is the molecular weight after x hours under depolymerization conditions. All depolymerization has been conducted at 90, $[RU]_0$ = 25 mM °C with 100 ppm of EY under green light.

6.4 Conclusions

To summarize, in this chapter, we report a complete study of the photocatalyzed depolymerization of methacrylate RAFT-made polymers with the aid of Eosin Y and visible light. For the first time it was demonstrated that under light irradiation and a very low amount of Eosin Y (in the ppm range), faster depolymerization rates and higher overall depolymerization conversions can be achieved when compared to exclusively thermal depolymerization at low temperature. Notably this approach maintains high performance also in DMSO (conversion up to 82%), much higher than the current reports on thermal depolymerization at 120°C. In addition, the experimental setup could work under various solvents and could be applied to different CTA and various methacrylates. The importance of light for an efficient depolymerization strategy was demonstrated by experiments at different light intensities and wavelengths.

Furthermore, the understanding of this new technique was sought by reversing the PET-RAFT mechanism achieving control during the depolymerization process. We first demonstrate that linear decreases in molecular weight during depolymerization were possible by increasing the concentration of the repeating units. Then the effect of concentration and CTA addition was further investigated in order to enhance deactivation, thus increasing the depolymerization control. The increased deactivation of the deporopagating chains allowed to module the kinetic behavior by switching ON and OFF the light but the thermal contribution in the chain activation did not allow an optimal temporal control. Finally, we were able to suppress thermolysis of the CTA by decreasing the depolymerization temperature, so that chain-end activation was possible only when light was used as an external stimulus to initiate depolymerization. This fine tune of the activation/deactivation equilibrium finally results in perfect temporal control and molecular weight shift for subsequent ON-OFF cycles. The same behavior was shown for different chain-termini and poly methacrylates, expanding the scope of the technique.

6.5 References

[1] N. Corrigan, K. Jung, G. Moad, C. J. Hawker, K. Matyjaszewski, C. Boyer, *Prog. Polym. Sci.* **2020**, *111*, DOI 10.1016/j.progpolymsci.2020.101311.

[2] A. Parkatzidis, K.; Wang, H. S.; Truong, N. P.; Anastasaki, *Chem.* **2020**, *6*, 1575−1588.

[3] G. Moad, E. Rizzardo, S. H. Thang, in *Aust. J. Chem.*, **2005**, pp. 379–410.

[4] F. Lorandi, M. Fantin, K. Matyjaszewski, *J. Am. Chem. Soc.* **2022**, *144*, 15413–15430.

[5] N. P. Truong, G. R. Jones, K. G. E. Bradford, D. Konkolewicz, A. Anastasaki, *Nat. Rev. Chem.* **2021**, *5*, 859–869.

[6] S. Perrier, *Macromolecules* **2017**, *50*, 7433–7447.

[7] M. R. Martinez, F. De Luca Bossa, M. Olszewski, K. Matyjaszewski, *Macromolecules* **2022**, *55*, 78–87.

[8] H. S. Wang, N. P. Truong, Z. Pei, M. L. Coote, A. Anastasaki, *J. Am. Chem. Soc.* **2022**, *144*, 4678–4684.

[9] M. R. Martinez, S. Dadashi-Silab, F. Lorandi, Y. Zhao, K. Matyjaszewski, *Macromolecules* **2021**, *54*, 5526–5538.

[10] H. S. Wang, N. P. Truong, G. R. Jones, A. Anastasaki, *ACS Macro Lett.* **2022**, 1212–1216.

[11] D. J. Lloyd, V. Nikolaou, J. Collins, C. Waldron, A. Anastasaki, S. P. Bassett, S. M. Howdle, A. Blanazs, P. Wilson, K. Kempe, D. M. Haddleton, *Chem. Commun.* **2016**, *52*, 6533–6536.

[12] Y. Sano, T. Konishi, M. Sawamoto, M. Ouchi, *Eur. Polym. J.* **2019**, *120*, 109181.

[13] M. J. Flanders, W. M. Gramlich, *Polym. Chem.* **2018**, *9*, 2328–2335.

[14] S. Huang, X. Su, Y. Wu, X.-G. Xiong, Y. Liu, *Chem. Sci.* **2022**, 11352–11359.

[15] M. R. Martinez, K. Matyjaszewski, *CCS Chem.* **2022**, *4*, 2176–2211.

[16] G. G. Hedir, C. A. Bell, N. S. Ieong, E. Chapman, I. R. Collins, R. K. O'Reilly, A. P. Dove, *Macromolecules* **2014**, *47*, 2847–2852.

[17] N. De Alwis Watuthanthrige, J. A. Reeves, M. T. Dolan, S. Valloppilly, M. B. Zanjani, Z. Ye, D. Konkolewicz, *Macromolecules* **2020**, *53*, 5199–5207.

[18] J. A. Reeves, M. L. Allegrezza, D. Konkolewicz, *Macromol. Rapid Commun.* **2017**, *38*, 1–5.

[19] T. Nwoko, N. De Alwis Watuthanthrige, B. Parnitzke, K. Yehl, D. Konkolewicz, *Polym. Chem.* **2021**, *12*, 6761–6770.

[20] "IUPAC Top Ten Emerging Technologies in Chemistry.," can be found under https://iupac.org/what-we-do/top-ten/., **n.d.**

[21] M. Sender, D. Ziegenbalg, *Chemie-Ingenieur-Technik* **2017**, *89*, 1159–1173.

[22] J. Yeow, R. Chapman, A. J. Gormley, C. Boyer, *Chem. Soc. Rev.* **2018**, *47*, 4357–4387.

[23] G. Ng, J. Yeow, J. Xu, C. Boyer, *Polym. Chem.* **2017**, *8*, 2841–2851.

[24] Y. Chu, N. Corrigan, C. Wu, C. Boyer, J. Xu, *ACS Sustain. Chem. Eng.* **2018**, *6*, 15245–15253.

[25] Y. Chu, Z. Huang, K. Liang, J. Guo, C. Boyer, J. Xu, *Polym. Chem.* **2018**, *9*, 1666–1673.

[26] J. Wang, M. Rivero, A. Muñoz Bonilla, J. Sanchez-Marcos, W. Xue, G. Chen, W. Zhang, X. Zhu, *ACS Macro Lett.* **2016**, *5*, 1278–1282.

[27] P. R. Judzewitsch, N. Corrigan, F. Trujillo, J. Xu, G. Moad, C. J. Hawker, E. H. H. Wong, C. Boyer, *Macromolecules* **2020**, *53*, 631–639.

[28] N. Corrigan, J. Yeow, P. Judzewitsch, J. Xu, C. Boyer, *Angew. Chemie - Int. Ed.* **2019**, *58*, 5170–5189.

[29] S. Shanmugam, J. Xu, C. Boyer, *Macromolecules* **2014**, *47*, 4930–4942.

[30] M. Li, M. Fromel, D. Ranaweera, S. Rocha, C. Boyer, C. W. Pester, *ACS Macro Lett.* **2019**, *8*, 374–380.

[31] S. E. Seo, E. H. Discekici, Y. Zhang, C. M. Bates, C. J. Hawker, *J. Polym. Sci.* **2020**, *58*, 70–76.

[32] A. Bagheri, C. W. A. Bainbridge, K. E. Engel, G. G. Qiao, J. Xu, C. Boyer, J. Jin, *ACS Appl. Polym. Mater.* **2020**, *2*, 782–790.

[33] Z. Zhang, N. Corrigan, A. Bagheri, J. Jin, C. Boyer, *Angew. Chemie - Int. Ed.* **2019**, *58*, 17954–17963.

[34] C. W. A. Bainbridge, K. E. Engel, J. Jin, *Polym. Chem.* **2020**, *11*, 4084–4093.

[35] J. Xu, K. Jung, A. Atme, S. Shanmugam, C. Boyer, *J. Am. Chem. Soc.* **2014**, *136*, 5508–5519.

[36] S. Shanmugam, J. Xu, C. Boyer, *J. Am. Chem. Soc.* **2015**, *137*, 9174–9185.

[37] J. Xu, K. Jung, N. A. Corrigan, C. Boyer, *Chem. Sci.* **2014**, *5*, 3568–3575.

[38] J. Xu, S. Shanmugam, H. T. Duong, C. Boyer, *Polym. Chem.* **2015**, *6*, 5615–5624.

[39] K. Parkatzidis, N. P. Truong, M. N. Antonopoulou, R. Whitfield, D. Konkolewicz, A. Anastasaki, *Polym. Chem.* **2020**, *11*, 4968–4972.

[40] P. N. Kurek, A. J. Kloster, K. A. Weaver, R. Manahan, M. L. Allegrezza, N. De Alwis Watuthanthrige, C. Boyer, J. A. Reeves, D. Konkolewicz, *Ind. Eng. Chem. Res.* **2018**, *57*, 4203–4213.

[41] M. L. Allegrezza, D. Konkolewicz, *ACS Macro Lett.* **2021**, *10*, 433–446.

[42] M. L. Allegrezza, N. De Alwis Watuthanthrige, Y. Wang, G. A. Garcia, H. Ren, D. Konkolewicz, *Polym. Chem.* **2020**, *11*, 6129–6133.

[43] V. Srivastava, P. P. Singh, *RSC Adv.* **2017**, *7*, 31377–31392.

[44] R. Whitfield, K. Parkatzidis, N. P. Truong, T. Junkers, A. Anastasaki, *Chem* **2020**, *6*, 1340–1352.

[45] N. Corrigan, D. Rosli, J. W. J. Jones, J. Xu, C. Boyer, *Macromolecules* **2016**, *49*, 6779–6789.

[46] J. Yeow, R. Chapman, J. Xu, C. Boyer, *Polym. Chem.* **2017**, *8*, 5012–5022.

[47] M. Majek, F. Filace, A. J. Von Wangelin, *Beilstein J. Org. Chem.* **2014**, *10*, 981–989.

[48] H. Cao, G. Wang, Y. Xue, G. Yang, J. Tian, F. Liu, W. Zhang, *ACS Macro Lett.* **2019**, 616–622.

[49] S. Allison-Logan, Q. Fu, Y. Sun, M. Liu, J. Xie, J. Tang, G. G. Qiao, *Angew. Chemie - Int. Ed.* **2020**, *59*, 21392–21396.

[50] J. A. Reeves, N. De Alwis Watuthanthrige, C. Boyer, D. Konkolewicz, *ChemPhotoChem* **2019**, *3*, 1171–1179.

[51] M. D. Thum, S. Wolf, D. E. Falvey, *J. Phys. Chem. A* **2020**, *124*, 4211–4222.

[52] J. F. Quinn, E. Rizzardo, L. Barner, C. Barner-Kowollik, T. P. Davis, *Am. Chem. Soc. Polym. Prepr. Div. Polym. Chem.* **2002**, *43*, 319–320.

[53] R. N. Carmean, C. A. Figg, G. M. Scheutz, T. Kubo, B. S. Sumerlin, *ACS Macr o Lett.* **2017**, *6*, 185–189.

[54] J. B. Young, J. I. Bowman, C. B. Eades, A. J. Wong, B. S. Sumerlin, *ACS Macro Lett.* **2022**, *11*, 1390–1395.

[55] V. Bellotti, K. Parkatzidis, H. S. Wang, N. De Alwis Watuthanthrige, M. Orfano, A. Monguzzi, N. P. Truong, R. Simonutti, A. Anastasaki, *Polym. Chem.* **2022**, *14*, 253–258.

Chapter 7

General Conclusions

This PhD thesis highlights the importance of understanding and further developing the PET-RAFT technique in the field of polymer chemistry for the production of new classes of functional materials, particularly with nanotechnology purposes, and its applicability in chemical recycling.

The first approach was based on the understanding of heterogeneous TiO_2 catalyzed PET-RAFT from a mechanistic perspective. To achieve this, a precise investigation was carried out by combining polymerization kinetic investigations with Density Functional Theory (DFT) calculations. This strategic approach not only recognized energy transfer as the primary pathway for CTA activation but also highlighted the pivotal role played by the catalyst surface area and the chemical nature of the selected CTA. Furthermore, the catalyst limitation was successfully overcame by shifting its absorption from UV to visible lights, improving the polymerization performance in terms of control and livingness of the polymer chains.

In the area of advanced materials, special attention was paid to the development of facile synthetic procedures for the fabrication of nanomaterials, including both nanoparticles and nanocomposites. In the case of nanoparticles, a one-pot synthesis of soft-core hard-shell nanoparticles was carried out through a dispersion polymerization-induced self-assembly protocol, concurrently encapsulating the porphyrin-based photocatalysts within the particle cores. This method, distinguished by its simplicity, eliminated the need for toxic solvents and allowed the production of upconverting nanoparticles. Similarly, it gave a new aim to the photocatalyst, which was finally used as sensitizer. In a similar way, perovskite/polymer nanocomposites were efficiently produced in a single-step oxygen-tolerance process. Herein, the full potential of PET-RAFT was exploited, *i.e.* room temperature polymerization, without relying on external radical sources, which are known to be detrimental for the polymerization and the optical properties of the final material. Notably, the specific interactions between the CTA and the perovskite crystal (as previously elucidated for TiO_2) played a pivotal role in producing high-loaded nanocomposites while preserving high yields.

Nevertheless, while PET-RAFT addresses many common limitations of traditional RAFT polymerization, it remains challenged by the inherent cost associated with the use of CTAs, thereby precluding its full-scale industrial transition. However, a recent breakthrough has opened up new possibilities: the regeneration of initial monomers and CTAs for subsequent use in the creation of new materials. Interestingly, even in this context, the reversal of the PET-RAFT protocol offers several noteworthy advantages. In fact, the thesis concludes with a study on the photocatalyzed temporal-regulated depolymerization of polymethacrylates. This investigation yielded remarkable results, demonstrating exceptional monomer regeneration capabilities even at lower temperatures. This breakthrough, coupled with other pioneering studies on light-induced depolymerization, represents a promising step towards chemical recycling by overcoming some of the current depolymerization challenges.

In essence, this thesis underscores PET-RAFT's multifaceted utility, from shedding light on complex mechanistic aspects to facilitating the synthesis of advanced nanomaterials and their depolymerization. The advantages offered by PET-RAFT, combined with its applicability, makes it a significant area of research with substantial industrial implications. As we continue to explore and refine this technique, we move closer to a more sustainable and efficient future in the field of polymer materials. However, there is still work to be done in terms of optimizing and scaling up the technique, expanding its applicability, and addressing its limitations.

Appendix I: Methods

8.1 Characterization Techniques

Nuclear magnetic resonance (NMR)

Chemical structures were investigated through ^{1}H NMR spectra, recorded using a Bruker Ascendent 400 spectrometer operating at 400 MHz, equipped with a 9.4T magnet. The NMR tube was prepared with 25-30 mg of sample dissolved in 0.7 mL of deuterated chloroform or d-DMSO.

Gel permeation chromatography (GPC)

For all the polymerization reactions Gel Permeation Chromatography (GPC) was used to determined molecular weight distributions and polydispersity indexes using a WATER 1515 isocratic HPLC Pump, a WATER 2414 refractive index detector, four Styragel columns (HR2, HR3, HR4, HR5). 10 mg of the sample was dissolved in 2 mL of THF adding 7 µL of toluene and the chromatograms was recorded with a flow of 1.0 ml/min at 35 °C. A calibration with polystyrene standards was used.

In the case of depolymerization analysis GPC was measured on Shimadzu equipment comprising a CBM-20A system controller, LC-20AD pump, SIL-20A automatic injector, 10.0 µm bead-size guard column (50 x 7.5 mm) followed by three KF-805L columns (300 x 8 mm, bead size: 10 µm, pore size maximum: 5000 Å), SPD-20A ultraviolet detector, and a RID-20A differential refractive index detector. The column temperature was maintained at 40 °C using a CTO-20A oven. The flow rate was set to 1 ml/min and with N, N-dimethylacetamide (DMAc, Acros, HPLC grade, with 0.03 w/v LiBr) as the eluent. The UV wavelength was set to 310 nm. Molecular weights were determined relative to poly(methyl methacrylate) standards with molecular weights ranging from 5,000 to 1.5 x 106 g/mol (Agilent Technologies). All SEC samples were dissolved in DMAc and passed through 0.45 μm PTFE filters prior to analysis.

Differential scanning calorimetry (DSC)

Thermal properties were determined by Differential Scanning Calorimetry (DSC) using a Mettler Toledo DSC instrument with a heating and cooling rate of 20 or 10 °C/min under nitrogen gas flow (80 mL/min). Calibration was performed each time the instrument was turned on with In standard. Glass transition temperature resulted from the analysis was calculated considering the inflection point of the second order transition.

Thermal gravimetric analysis (TGA)

TGA analysis was carried out with a Mettler Toledo TGA/DSC STARe System, at a constant gas flow (50 cm^3/min). The thermal profile was the following: first cycle from 20 °C to 130 °C with heating rate of 20 °C/min followed by cooling at 50 °C under nitrogen in order to eliminate all residual solvent, final heating till 1000 °C was performed in air flow with a rate 10 C min^{-1}.

Dynamic Light Scattering (DLS)

Hydrodynamic volume and size distribution of nanoparticles was determined by dynamic light scattering. This technique measures the diffusion of particles moving under Brownian motion, and converts this to size and a size distribution using the Stokes-Einstein relationship. The measures were recorded at 25 °C on a Malvern Zetasizer Nano S equipped with a continuous wave 1mW He-Ne monochromatic laser operating at 632.8 nm and an avalanche photodiode detector, Q.E. > 50% at 633 nm, placed at 173° with respect to the incident beam. Reported data are the average of at least three different measurements of the size distribution as the function of the intensity.

Fourier Transform Infrared spectroscopy (FT-IR)

Fourier transform infrared characterization was performed using a PerkinElmer Spectrum 100 instrument scanning from 650 to 4000 cm^{-1} with a resolution of 4 cm^{-1} for 32 scans. The sample, in the form of powder, is added on the sample holder and directly analyzed over the Si crystal with the Universal ATR (UATR).

Raman spectroscopy

Raman spectra were collected with a Horiba Jobin-Yvon Labtam HR coupled with a microscope equipped with a Marzhauser Wetzlar SCANplus motorized XYZ stage (75x50mm). Samples have be observed with Olympus achromatic 50x MPLN objective and excited in backscattering geometry with a 632 nm frequency. The spectra were collected with an acquisition time of 60 seconds between 100 and 900 cm^{-1}.

Electron Paramagnetic Resonance (EPR)

The Electron Paramagnetic Resonance (EPR) investigation on N-doped TiO_2 was performed by a Bruker EMX spectrometer working at the X-band frequency and equipped with an Oxford cryostat working in the range of temperature 4–298 K. The powder sample was contained within quartz glass tubes connected to a high vacuum pumping system. Spectra were recorded in vacuo conditions ($p < 10-5$ mbar) at 130 K. Modulation frequency was 100 kHz, modulation amplitude 2–5 gauss, and microwave power 0.2-63.5 mW. Care was taken in order to always keep the most sensitive part of the EPR cavity (1.5 cm length) filled.

Powder X-Ray Diffraction (PXRD)

Powder X-ray diffraction (PXRD) analyses were performed using a benchtop Rigaku MiniFlex 600 operating at 45 kV and 40 mA equipped with a copper radiation source (Kα Cu 1.54 Å). PXRD of $CsPbBr_3$ samples were prepared by drop-casting a concentrated NC toluene dispersion (50 mg/mL) onto glass slides. Diffractograms were collected in a laboratory atmosphere and room temperature from 10° to 45° with steps of 0.02 and 0.2 deg/min speed. For TiO_2 samples the PXRD patterns were collected in the 2θ range 20–80° (2θ step 0.020°, 1° min^{-1} scan rate).

Transmission Electron Microscopy (TEM)

TEM images on materials were collected by using a JEOL JEM-2100Plus TEM (JE OL, Akishima, Tokio, Japan) operating at an acceleration voltage of 200 kV, equipped with an 8-megapixel Gatan (Gatan, Pleasanton, CA, USA) Rio complementary metal-oxide-semiconductor camera. The CsPbBr3 samples were prepared by drop casting a toluene NCs dispersion (0.1 mg/mL) onto an ultrathin lacey carbon TEM grid. High resolution imaging was performed in parallel illumination mode using a CMOS Gatan RIO camera. The TiO_2 samples were deposited onto carbon-coated Cu TEM mesh grids by drop-casting dilute NPs dispersions in ethanol.

X-Ray Photoelectron Spectroscopy (XPS)

The surface chemical composition of the N-TiO_2 powders was investigated by XPS. The measurements were performed on the as-prepared powder samples, fixing them on the sample holder using carbon tape. The XPS spectra were acquired in ultrahigh vacuo (base pressure: $\sim 5 \times 10^{-10}$ mbar) at RT in normal emission geometry using a conventional Mg X-ray source (hν = 1253.6 eV) and a hemispherical electron energy analyzer (120 mm by PSP: total energy resolution ∼ 0.8 eV, standard deviation ± 0.2 eV). Due to charging effects, all binding energies (BE) were calibrated by fixing the C 1s BE of atmospheric contamination at 284.8 eV. Survey scans were obtained in the 0–1100 eV range, while detailed scans were recorded in the BE regions corresponding to N 1s, and O 1s levels. The N 1*s* XPS spectra was reproduced by fitting the experimental data using a Shirley background and several Doniach-Sunjich components, corresponding to different oxidation states and chemical environments.

Optical and Photoluminescence Studies for UC evaluation

UV–vis absorption spectra were recorded on a Cary Varian 50 spectrometer. Steady-state PL spectra were acquired with a with a nitrogen cooled charge coupled device (Spex ≈2000) coupled to a polychromator Triax 190 from J-Horiba. Steady state fluorescence spectra have been recorded using a 355 nm UV laser. Fluorescence emission intensity decay have been recorded using a pulsed LED at 340 nm (3.65 eV, EP-LED 340 Edinburgh Instruments, pulse width of 700 ps). Green-to-blue upconversion spectra were recorded using a focused doubled Nd:YAG diode pumped Coherent Verdi TEM 00 CW laser at 532 nm for excitation. The 1/e2 beam diameter of 0.80 mm (Nd:YAG) has been measured by the knife blade method. The laser intensity was varied using reflective power density neutral filters and measured with an optical power meter (Thorlabs PM100USB, power sensor S120VC). The laser stray light was attenuated with a notch filter in the detection line. All spectra were corrected for the instrumental optical response. For time-resolved upconversion measurements, the samples were excited at 532 nm by modulating a Nd:YAG laser with a TTi TG5011 wavefunction generator with a duty cycle of 50%, in order to reach the steady state condition before monitoring the upconverted emission in intensity decay. The spectra were recorded by nitrogen cooled photomultiplier (Hamamatsu R5509-73) coupled with a high-speed amplifier (Hamamatsu C5594), a 74 100 Cornerstone 2601/4 (ORIEL) monochromator, and a PCI plug-in multichannel scaler ORTEC 9353 100 ps time digitizer/MCS in a photon counting acquisition mode.

Optical characterization of $CsPbBr_3$ nanocomposites

Optical absorption measurements were measured in toluene with a Cary 50 UV–Vis spectrophotometer. The PL spectra were excited using a laser source at 3.06 eV (405 nm); the emitted light was collected using a custom apparatus featuring a liquid nitrogen-cooled, back-illuminated, and UV-enhanced charge-coupled device detector (Jobin-Yvon Symphony II) coupled to a monochromator (Jobin-Yvon Triax 180) with 100 lines/mm gratings and corrected for the spectral response of the system. Time-resolved PL were carried out using 3.06 eV (405 nm) ps-pulsed diode lasers (Edinburgh EPL405, ∼70 ps pulses); the emitted light was collected with a phototube coupled to a Cornerston 260 1/4 m VIS-NIR Monochromator (ORIEL) and a time-correlated single-photon counting unit (time resolution ∼400 ps).

8.2 Photoreactor characterization

The homemade photoreactor was built into a tube-like shape (diameter of 12 cm and height of 7 cm). On the inner walls of the photoreactor, an LED strip (Mxellex®) was placed inside in a spiral pattern. The final number of LEDs inside the photoreactor was 35. A silicone oil bath (diameter of 8 cm) where the reaction was heated was placed in the center of the photoreactor. Aluminum foil was used to cover the top of the reactor from external light. Photoreactor emission spectra were collected on a Varian Cary Eclipse spectrometer (**Figure 8.1a**). The maximum emission wavelength for blue, green, and red are respectively 460 nm (±17), 510 nm (±31), and 630 nm (±16) respectively. Photoreactor intensity was determined using a Thorlabs PM100D light power meter, equipped with a S170C Microscope Slide Power Sensor (**Figure 8.1b**).

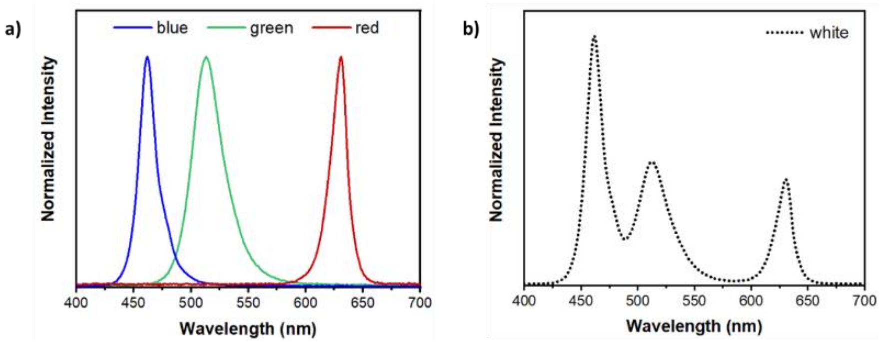

Figure 8.1: Normalized emission intensity of the a) blue, green, red, and b) white RGB LED strip used for the photoreactor.

Table 8.1: Characterization data of the photoreactor: Density of light has been control using a remote controller. High indicate the maxim intensity and low the minimum intensity that the LEDs strips can reach.

Reactor	**Wavelength (nm)**	**FWHM (nm)**	**Density of light**	**Intensity (mW/cm^2)**
Blue	460	17	High	3.63±0.55
			Low	0.26±0.03
Green	510	31	High	2.31±0.14
			Low	0.18±0.01
Red	630	16	High	1.14±0.11
			Low	0.12±0.01
White	460	17	High	8.75 ±0.34
	520	31	High	6.04±0.75
	630	16	High	5.33±0.82

List of Publications

V. Bellotti, R. Simonutti, “*New Light in Polymer Science: Photoinduced Reversible Addition-Fragmentation Chain Transfer Polymerization (PET-RAFT) as Innovative Strategy for the Synthesis of Advanced Materials*”, Polymers, **2021**, 13(7), 1119;

V. Bellotti, C. Daldossi, D. Perilli, M. D'Arienzo, M. Stredansky, C. Di Valentin, R. Simonutti, “*UV to visible light PET-RAFT polymerization catalyzed by titanium dioxide-based nanoparticles”*, Journal of Catalysis, 428, (**2023**), 115074.

V. Bellotti, G. Beretta, R. Simonutti, “*Synthesis of soft-core hard-shell nanoparticles by visible PET-RAFT polymerization in dispersion conditions*”, Polymer 271 (**2023**) 125804.

V. Bellotti, K. Parkatzidis, H. S. Wang, N.D.A. Watuthanthrige, M. Orfano, A. Monguzzi, N. P. Truong, R. Simonutti, A. Anastasaki, “*Light-accelerated depolymerization catalyzed by Eosin Y*”, Polym. Chem., **2023**, 14, 253-258.

V. Bellotti, H. S. Wang, N. P. Truong, R. Simonutti, A. Anastasaki, “*Temporal regulation of PET-RAFT controlled radical depolymerization*”, Angew. Chem. Int. Ed. 2023, e202313232.